DOCTORAL THESIS

# Principles of the axial pile setup

*Author:*
Alexander V. Busch

*Supervisor:*
Prof. Dr. Tobias Mörz

*Examiner:*
Prof. Dr. Tobias Mörz (1) and Prof. Dr.-Ing. Roberto Cudmani (2)

*A thesis submitted in fulfillment of the requirements*
*for the degree of **doctor rerum naturalium***

*in the working group of*

Marine Engineering Geology
MARUM - Center for Marine Environmental Sciences, University of Bremen

April 24, 2022
(revised version)

University
of Bremen

marum
Center for Marine
Environmental Sciences
University of Bremen

# Declaration of Authorship

I, Alexander V. Busch, residing at Heerwisch 20 - 22419 Hamburg, declare that this thesis titled: "Principles of the axial pile setup" and the work presented in it are my own. I affirm that:

- I wrote the present thesis independently and without illicit assistance from third parties,

- I used no sources other than those indicated nor aids other than those permissible,

- I appropriately referenced any text or content from other sources

Signed:

_____

Date:

_____

# The five rules of science

*"Only a few centuries ago, a mere second in cosmic time, we knew nothing of where or when we were. Oblivious to the rest of the cosmos, we inhabited a kind of prison, a tiny universe bounded by a nutshell. How did we escape from the prison? It was the work of generations of searchers who took five simple rules to heart.*

1. *Question authority. No idea is true just because someone says so, including me.*

2. *Think for yourself. Question yourself. Don't believe anything just because you want to. Believing something doesn't make it so.*

3. *Test ideas by the evidence gained from observation and experiment. If a favorite idea fails a well-designed test, it's wrong. Get over it.*

4. *Follow the evidence wherever it leads. If you have no evidence, reserve judgment. And perhaps the most important rule of all...*

5. *Remember: you could be wrong. Even the best scientists have been wrong about some things. Newton, Einstein, and every other great scientist in history – they all made mistakes. Of course they did. They were human.*

*Science is a way to keep from fooling ourselves, and each other".*
*Neil deGrasse Tyson*

UNIVERSITY OF BREMEN

# *Abstract*

Faculty Name

MARUM - Center for Marine Environmental Sciences, University of Bremen

**doctor rerum naturalium**

**Principles of the axial pile setup**

by Alexander V. Busch

Piles, as widely used foundations onshore and offshore for advanced structures or wind turbines are known for their frequently observed, long-lasting, capacity increases – known as the pile setup. Not seldom, this results in a doubling of the pile capacity within the first 100 days after their installation. Many sub-mechanisms are suspected to contribute to this increase, such as changes in the pile surrounding stress field, an aging of the soil, or modifications at pile shaft surface due to physiochemical processes. However, many of the existing studies focus too much on a single mechanism as a possible cause of the setup. As a result, attempts to transfer these findings to alternative sites and/or piles frequently did not produce satisfying results. The possibility, that this process might be multi-factorial is still often rejected or just ignored. As a result, there is still no conclusive theory to explain the setup in all its facets, even though it was first mentioned now 120 years ago. An improved understanding of the mechanisms and a consequent integration of the setup into daily engineering practice has the potential of considerable cost savings. In particular if smaller, thinner or shorter piles could be used to carry the same loads as before. When piles are used as foundations for wind turbines, eliminating such inefficiencies will be of utmost importance in a world of dwindling resources and for a humanity fighting the climate crisis. The present study aims at improving our understanding of this process in three, well defined sub-studies, which concern one constant test environment. An extensive, small-diameter field study (Chapter 4) reveals that the capacity of a pile and its setup is dependent on the respective installation method as well as on the corrosion vulnerability of the pile material. Piles installed by a rather soil disturbing installation method – i.e. by pile vibration instead of impact driving or pile jacking – potentially tend to a reduced initial capacity, but simultaneously, to a more pronounced setup. It is shown, that vibrated piles can reach capacities of identical impact driven piles after not more than 100 days of aging. Indications are provided, that for longer time ranges the vibrated piles might even outperform these impact driven piles. The second study (Chapter 5) evaluates three-years of capacity monitoring of six, offshore-size piles installed by pile vibration and by impact driving. It demonstrates that vibrated, large-diameter piles provide just a third of the capacity of impact driven equivalents even after an aging period of three years. The small-pile experiment hypothesis is consequently rejected, and a size dependence of the pile setup is assumed. A final laboratory and modeling study (Chapter 6) evaluates the impacts of physiochemical effects on the overall setup. Direct shear testing of naturally-aged surfaces and subsequent capacity modeling indicate that physiochemical effects and the formation of a pile adhering sand-crust have a high potential to increase pile capacity. With these three sub-studies, this doctoral thesis provides a significant contribution to the understanding of the setup as a multi-factorial and multidimensional process.

# *Acknowledgements*

# Contents

xii

# List of Figures

# List of Tables

# List of Abbreviations

| | |
|---|---|
| **CPT** | Cone Penetration Testing |
| **CS** | Corrosion Scenario |
| **Css** | Cyclic strain scenario |
| **CE** | Closed Ended |
| **DLT** | Dynamic Load Testing |
| **EoD** | End of Driving |
| **GL** | Ground Level |
| **GWL** | Ground Water Level |
| **GRAD** | Graduation |
| **ID** | Impact Driving |
| **J** | Jacking |
| **LAR** | Least Absolute Residual |
| **LOESS** | LOcally Weighted Scatter-plot Smoother |
| **MGL** | Mean Groundwater Level |
| **ms** | mild steel |
| **mbgl** | meter below ground level |
| **OE** | Open Ended |
| **PG** | Poorly Graded |
| **PRV** | Pressure Reliefe Valve |
| **REF** | Reference |
| **Sf** | Surface |
| **SLT** | Static Load Testing |
| **ss** | stainless steel |
| **TS** | This Study |
| **WG** | Well Graded |

# List of Symbols

| | | |
|---|---|---|
| $A$ | setup factor | - |
| $A_s$ | surface area | - |
| $A_{rs,eff}$ | effective pile area ratio | - |
| $API_{Nq}$ | API-00 bearing capacity factor | - |
| $API_{max}$ | API-00 shaft friction limit | Pa (kg m$^{-1}$ s$^{-2}$) |
| $API_{qmax}$ | API-00 unit end bearing limit | Pa (kg m$^{-1}$ s$^{-2}$) |
| $ax.Red$ | unadjusted reduction factor | - |
| $ax.Red_t$ | adjusted toe reduction | - |
| $ax.Red_u$ | adjusted reduction factor | - |
| $c_v$ | coefficient of consolidation | m$^2$ s$^{-1}$ |
| $D$ | pile outer diameter | m |
| $D_R$ | relative soil density | - |
| $D_{50}$ | mean grain size | m |
| $e_{field}$ | in-situ (field) void ratio | - |
| $e_{max}$ | maximum void ratio | - |
| $e_{min}$ | minimum void ratio | - |
| $e_0$ | initial void ratio | - |
| $F$ | force | N (kg m s$^{-2}$) |
| $F_{max}$ | maximum applied force | N (kg m s$^{-2}$) |
| $f_s$ | sleeve friction | Pa (kg m$^{-1}$ s$^{-2}$) |
| $h$ | distance to pile tip | m |
| $h_s$ | sensor hight over ground level | m |
| $IFR$ | incremental filling ratio | m |
| $k_f$ | soil permeability | m s$^{-1}$ |
| $L$ | pile embendment length | m |
| $L_{eff}$ | effective pile embendment length | m |
| $N_{bA}$ | number of blows per unit external pile shaft area | m$^{-2}$ |
| $n$ | distribution size | - |
| $P$ | mean peak height line roughness | m |
| $Q$ | soil quake | m |
| $Q_s$ | pile shaft capacity | N (kg m s$^{-2}$) |
| $Qs_{corr}$ | offset-corrected shaft capacities | N(kg m s$^{-2}$) |
| $Q_{ti}$ | axial pile capacity at time $ti$ | N (kg m s$^{-2}$) |
| $Q_{t0}$ | axial pile capacity at reference time $t0$ | N (kg m s$^{-2}$) |
| $q_c$ | tip resistance | Pa (kg m$^{-1}$ s$^{-2}$) |
| $q_{c1N}$ | air pressure normalized CPT tip resistance | Pa (kg m$^{-1}$ s$^{-2}$) |
| $R$ | pile outer radius | m |
| $R_i$ | pile internal radius | m |
| $R^2$ | coefficient of determination | - |
| $R$ | equivalent pile radius | m |
| $R_s$ | dynamic pile shaft resistance | N (kg m s$^{-2}$) |
| $R_{set}$ | setup ratio | - |

| | | |
|---|---|---|
| $R_t$ | dynamic pile toe resistance | N $\text{kg}\,\text{m}\,\text{s}^{-2}$) |
| $R_u$ | total resistance | N ($\text{kg}\,\text{m}\,\text{s}^{-2}$) |
| $R_{CLA}$ | mean centerline (line) roughness | m |
| $R_{Dynamic}$ | dynamic resitance | N ($\text{kg}\,\text{m}\,\text{s}^{-2}$) |
| $R_{Static}$ | static resitance | N ($\text{kg}\,\text{m}\,\text{s}^{-2}$) |
| $Si$ | soil sensitivity | - |
| $s$ | shear displacement | m |
| $\dot{s}$ | shear displacement rate | $\text{m}\,\text{s}^{-1}$ |
| $\overline{Sa}$ | mean centerline surface roughness | m |
| $t0$ | setup reference time | d |
| $ti$ | time after reference time $t0$ | d |
| $V$ | pile excavation depth | m |
| $v$ | velocity | $\text{m}\,\text{s}^{-2}$ |
| $w, w_1, w_2$ | pile wall thicknesses | m |
| $\bar{x}$ | arithmetic mean | - |
| $z_{tip}$ | depth of pile tip below ground level | m |
| $\sigma_{rd}$ | effective, radial-acting, dilative stress component | Pa ($\text{kg}\,\text{m}^{-1}\,\text{s}^{-2}$) |
| $\delta_{cv}$ | constant volume, interface friction angle | degree |
| $\delta_{max}$ | maximum, interface friction angle | degree |
| $t$ | elapsed time | s |
| $\rho_s$ | particle density | $\text{kg}\,\text{m}^{-3}$ |
| $\rho_d$ | bulk density | $\text{kg}\,\text{m}^{-3}$ |
| $\sigma_f$ | effective, radial-acting stress at pile failure | Pa ($\text{kg}\,\text{m}^{-1}\,\text{s}^{-2}$) |
| $\sigma_{v0}$ | effective, vertical-acting stress | Pa ($\text{kg}\,\text{m}^{-1}\,\text{s}^{-2}$) |
| $\sigma_{rs}$ | effective, radial-acting, static stress component | Pa ($\text{kg}\,\text{m}^{-1}\,\text{s}^{-2}$) |
| | effective, circumferential-acting stress | Pa ($\text{kg}\,\text{m}^{-1}\,\text{s}^{-2}$) |
| $\tau_{avg}$ | averaged pile shaft shear stress | Pa ($\text{kg}\,\text{m}^{-1}\,\text{s}^{-2}$) |
| $\tau_{f\,UWA}$ | pile shaft shear stress after UWA-05 | Pa ($\text{kg}\,\text{m}^{-1}\,\text{s}^{-2}$) |
| $\tau_{f\,ICP}$ | pile shaft shear stress after ICP-05 | Pa ($\text{kg}\,\text{m}^{-1}\,\text{s}^{-2}$) |
| $\tau_f$ | pile shaft shear stress | Pa ($\text{kg}\,\text{m}^{-1}\,\text{s}^{-2}$) |
| $\varphi_{cv}$ | constant volume, sand-to-sand shear angle | degree |
| $\varphi_{max}$ | maximum, sand-to-sand shear angle | degree |

*In memory of Matthias Daum, the best brother-in-law that anyone could ever have had...*

# Chapter 1

# Preface

## 1.1 Organization of the thesis

This thesis was developed as part of the Restrike-XL project (0324231A), funded by the Federal Ministry for Economic Affairs and Energy of Germany, and is a part of the Carbon Trust initiative. In a collaboration of industry and academia, this project focuses on the investigation of cause and effect relations concerning to the frequently observed capacity increase of driven piles.

**Chapter 2** provides an introduction into the general theory of piles. It will be presented and explained how piles are used as deep foundations in engineering practice, how they are classified and how their capacity is generated (2.1-2.5). The process which will be the main subject of the thesis – the setup effect – will be explained in detail (2.8.1 - 2.8.6). Furthermore, the state of the art and the scientific hypotheses will be tackled.

**Chapter 3** provides on overview over the basic scientific methods used. Since each publication itself contains its own methods section, methods introduced in this chapter are only presented superficially and on an abstract level.

**Chapter 4** presents a field study dealing with the research hypothesis 1, and quantifies the impact of varying installation methods on the initial pile capacity as well as on its subsequent setup. This research paper – Busch et al. (2022) – was submitted to Geomechanics for Energy and the Environment on September 23th (2021) and was accepted for publication on April 19th (2022).

**Chapter 5** presents the capacity evolution of six, large-diameter, open-ended monopiles derived by the VIBRO project. Because three of them have been installed by impact driving and three by pile vibration, a unique opportunity is given to compare capacities of real-size offshore piles installed by different methods. This chapter deals with the research hypothesis 2 and will be submitted to Ocean Engineering.

**Chapter 6** provides inside into how natural corroded surfaces affect the friction behavior of a pile. Furthermore, its potential impact on the pile capacity is estimated. The data is compared to and validated through by both previous field studies (Chapters 4-5). The research hypothesis 3 is tackled. The study was submitted to Géotechnique on February 22th (2022) and is currently in revision.

**Chapter 7** recapitulates the main conclusions of Chapters 4-6 with respect to the research hypotheses. Supplemental figures are presented in **Chapter A** along with all of the experimental data in **Chapter B**.

## 1.2    Author contributions

The following authors have contributed to the dissertation at hand. Their exact share is broken down.

1. Alexander V. Busch[1] - AVB

2. Max O. Kluger[1,2] - MOK

3. Tobias Mörz[1,3] - TM

4. Majid Goodarzi[1] - MG

5. Daniel A. Hepp[1] - DAH

6. Stefan Kreiter[1] - SK

7. Benjamin Ossig[3] - BO

8. Akash Verma[3] - AV

9. Pooyan Ghasemi[4] . PG

[1]MARUM – Center for Marine Environmental Sciences, University of Bremen, Bremen, Germany
[2]School of Science/Te Aka Mātuatua, University of Waikato, Hamilton, New Zealand
[3]Geo-Engineering GmbH, Bremen, Germany
[4]COWI A/S, Hamburg Branch Office, Hamburg, Germany

### Chapter 4

Methodology and concept of the study were developed by AVB and reviewed for reliability by MOK, DAH, MG, SK and TM. The field work was conducted by AVB, including planing, material procurement, investigation, logistics and execution of all static pile tests. The code for evaluation was written solely by AVB. The original draft of the paper was written by AVB. MOK, DAH, MG, SK and TM were involved in the rewriting, editing and overall review process. The visualization was prepared by AVB and revised by MOK and DAH to guarantee high scientific quality. Project administration and funding acquisition was done by MOK and TM. TM had the supervision and responsibility for the project and the study.

### Chapter 5

Methodology and concept of the study were developed by AVB and MG as well as reviewed by BO, AV, PG and TM. The dynamic pile load testing was done by MG, BO, AV and PG, including planing, material procurement, investigation and logistics. The evaluation and analysis of the dynamic pile load data was done by MG, BO, AV and PG. The code for capacity modeling and the original manuscript draft was written by AVB and revised by MG, BO, AV, PG and TM. The visualization was done by AVB and revised by MG. Project administration and funding acquisition was done by TM. TM had the supervision and responsibility for the project and the study.

**Chapter 6**

Methodology and concept of the study were developed by AVB and MOK. Sampling and field work were conducted by AVB, MOK and TM. All direct shear experiments were executed (or supervised) solely by AVB. AVB wrote the code for data evaluation and the original manuscript draft, which was reviewed by MOK and TM. The visualization was done by AVB and quality checked by MOK to guarantee high scientific quality. Project administration and funding acquisition was done by TM. TM had the supervision and responsibility for the project and the study.

**Rest of the thesis**

Passages including the published work and quotations of others are marked accordingly. References of the respective passages are provided. Except quotations, attributions and the previously mentioned Chapters 4-6, this thesis is entirely and exclusively my own work.

# Chapter 2

# Introduction

## 2.1 Foundations in engineering practice

Every time when structural loads (i.e. constant acting self-weight or live loads) have to be transfered into the ground, foundations are in use. Commonly, these loads act vertically even if for some cases significant lateral loads or movements may occur. Optimally, the soil can bear these loads without additional improvements. In civil engineering this beneficial situation is always given when the deformations of a material or soil to an applied load are negligible, homogeneous for the whole structure, or at least not critical regarding its functionality or serviceability.

However, all known materials tend to respond to external acting forces with the formation of internal forces - called stresses $\sigma$ - and ultimately with a deformation like e.g. a displacement. The gradient of such a displacement responsible for a change in shape or volume of the material due to acting stresses is called strain $\varepsilon$. Assuming an simplified elastic material behavior and one-dimensional conditions, Hook's law is capable to describe the relations between stress and strain as follows:

$$\varepsilon = \frac{\sigma}{E} = \frac{F}{E \cdot A_s} \qquad\qquad F \dots force; A_s \dots surface\, area \qquad (2.1)$$

Both values are connected by the reciprocal of a material parameter, the Elastic or Young's - Modulus ($E$). Eq. 2.1 reveals, that the higher the Elastic Modulus, the lower the resulting strains. Naturally, these perfect beneficial conditions can only be accomplished for rock basements or for negligible loads induced by small and light structures, like i.e. shelters. If larger deformations instead are expected, the distribution of the acting loads by a additional rigid structure to a wider area (increasing $A_s$), lowers the potential stress ($\sigma$) subjected to the identical acting force $F$. This load-distributing type of foundations are referred to as "shallow foundations" or "footings" and are basically strips or pads of reinforced concrete with varying thicknesses and lateral dimension. The most common type might be the mat- or raft-foundation, containing a continuous slab of usually reinforced concrete. Typically, these reinforced concrete slabs then covers the entire base of a building or structure.

If the calculated dimensions necessary for a non-hazardous construction nonetheless exceed a realistic scope or are economically unfavorable, alternative methods that attempt to dampen the resulting deformations have to be considered. As a rule, soil improvements such as compaction or even the partial replacement of very weak soil layers are then considered. Soft clays, silts or peats are just some examples of such weak soil layers typically found near the river mouths, along the perimeters

of bays or beneath swamps or lagoons. Every time these sediments occur, they require specially adapted geotechnical consideration. A combination of ground improvements combined with a shallow foundation are also frequently used solutions. Since this topic of ground improvements opens up a very broad field, reference is made to Holtz, Kovacs, and Sheahan (1981), which deals with this topic extensively and in great detail. From an economic perspective, soil improvements mostly pay off for small areas and/or thin soil layers. Heavy machinery has to be deployed, such as scrapers or rollers, and effort required to ensure a sufficient improvement increases exponentially with the thickness of the layer (Holtz, Kovacs, and Sheahan, 1981). Then again, if the soil layer exceeds a distinct dimension, it can become more favorable to resort to deep foundations i.e. piles.

## 2.2   Pile foundations

Piles are normally slender load bearing structures where their embedded length $L$ exceeds their diameter $D$ by far. As the typical type of deep foundations, piles differ from shallow foundations in a way, that they divert forces or structural loads to a more distant or *deep* area. The deep foundation itself is again not defined by one pile alone (with the exception of the monopiles) but rather by an arrangement of several, that are often joined together by a pile-cap to form a group. Piles are today in use if a shallow foundation does not fulfill safety or economical requirements. Fellenius (1991) defined the following situations where piles become favorable in modern days.

- A competent soil layer can only be found at a high depths.

- The soil layers immediately below the structure, while competent, are subject to scour.

- The structure transmits large concentrated loads to the soil that cannot be spread horizontally by means of a wide, shallow foundation.

- The structure is very sensitive to differential settlement.

- The site has a very high water table or artesian water conditions and the soil is sensitive to the construction of even shallow excavations required for mat or footing foundations.

In history of human civilization, piles have been in use in central Europe at least since neolithic times (3300 up to 1800 BC). Wooden piles were driven into soft bedrock to extend buildings above flood effected zones, above lakes or coastal regions, or just above dangerous animals and hostile neighbors (Billamboz, 2014). Regarding to the habitus of piles, they can be divided into an upper part, the head or pile top, and into a lower basal area, called toe or base. Everything in between the head and the toe can be described as the pile shaft or pile mantle (Fig. 2.1A). Which of these terms - head or top, base or toe, mantle or shaft - is used depends mostly on the country, the pile aspect which is addressed (stress, friction, geometry) or simply by the preference of the author.
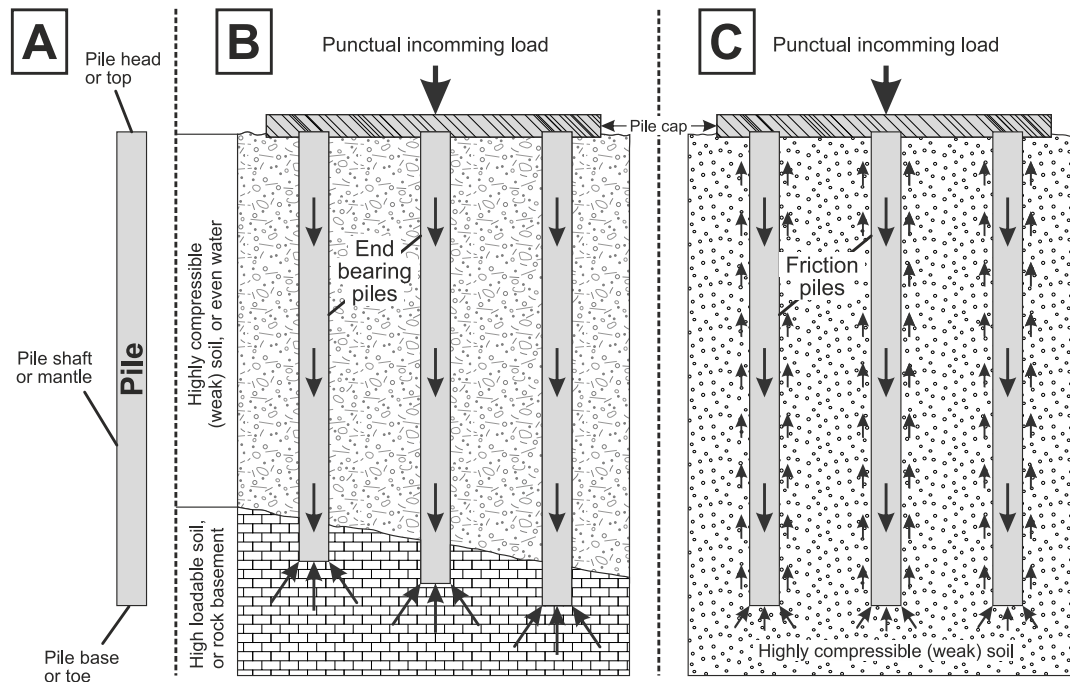
FIGURE 2.1: General pile description and classification according to
load distribution

## 2.3 Pile classification

Piles in their almost innumerable manifestations can be roughly divided according
to various criteria. Examples of the most common are listed below.

- Kind of load distribution: into end bearing piles (Fig. 2.1B) or friction piles
  (Fig. 2.1C)

- Interaction with the soil during installation: into driven-displacement, driven-
  non-displacement or drilled-replacement piles

- Construction material of the pile: into e.g. steel, wooden, or concrete piles

- Geometry of the cross sectional area: into e.g. H-, square-, pipe-like or sheet-
  piles (Fig. 2.2)

- Kind of basal-opening: into open-ended piles or closed-ended piles

- Installation method: into e.g. impact driven (hammered), jacked-, vibratory
  driven or drilled piles

- Structural combination: into e.g. monopiles where just one pile bears the loads
  or pile groups where the load is distributed to many

- Direction of loading: into in tension or compression piles as well as into hori-
  zontal and vertical loaded piles

While some of these criteria can be combined to describe a pile with increasing pre-
cision, some criteria are mutually exclusive.
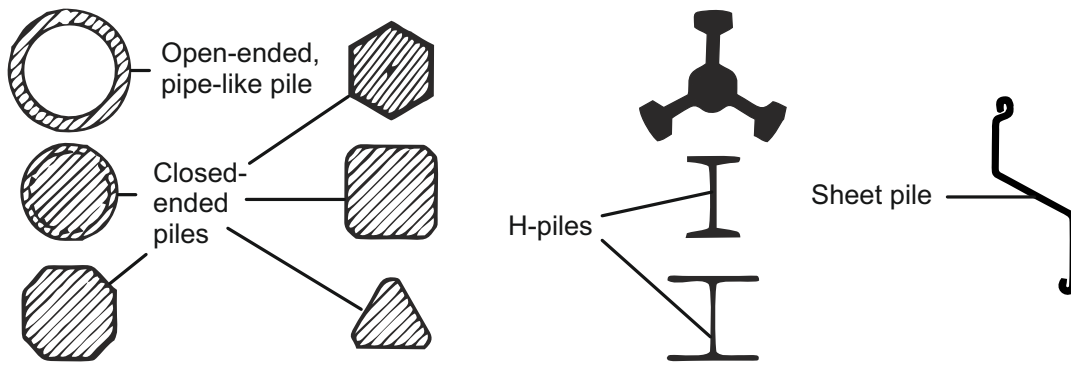
FIGURE 2.2: Pile classification according to pile cross sections. Modified after Fellenius (1991)

## 2.4  Pile installation techniques

The choice of pile installation is primarily defined by the intended type of load application (end-bearing or friction piles), the cost, the time, the available space, the soil, or by the sensitivity of the surrounding area to vibrations and noise. At onshore areas, the installation of non-displacement piles by auger drilling is state of the art (White and Deeks, 2007). While the borehole is kept open, concrete can be poured into the hole, forming so-called "cast-in-place piles". An alternative solution are "pre-cast piles", which are embedded into the hole. When disposal of excavated material, generated during conventional pile boring is limited, displacement methods like impact driving are used. With a hydraulic hammer or a drop weight, an impulse is applied to the pile head and transmitted through the shaft to its tip, forcing the pile into the ground. This procedure is usually associated with high noise emissions and vibrations, which eventually damage surrounding structures. Hence, this method is seldom used in urban areas. An alternative solution is provided by monotonically pushing the pile into the ground without any vibration or noise emissions. This method is called "pile jacking". Since this jacking method is not using the energetic advantage of a gravitational potential by a falling weight, the entire resistance of the pile-soil system has to be exceeded statically. Practically, the jacking devise has to provide at least the same weight force as the maximum resistance of the pile to be installed. Regularly, this is provided by dead-weights. If possible, the jacking device can overcome this principle by gripping the heads of already installed adjacent piles as an abutment. This installation method is often used for the installation of sheet-pile walls in soft soils (White and Deeks, 2007).

In the offshore sector, where bigger pile dimensions have to be handled, impact pile driving is the preferred technique. Recently, alternative installation techniques have been developed to reduce noise emissions. In this context, the "vibratory pile driving" installation method is most promising. In contrast to impact driving, the pile is subjected to a dynamic force, stimulated by a rotating and eccentric mass, attached to the pile head. These imposed cyclic loads reduces the friction at the pile shaft and the resistance underneath the pile toe due to the induced multi-directional strains (Cudmani, 2001). Problems with this method arise when it is difficult to assess the reaction of certain soil layers to such vibrations (Al-Sammarraie et al., 2018). In addition, pile capacity prediction methods have not yet been calibrated for this type of installation method. Due to a lack of data and varying constrains, pile vibration is still rarely used for offshore size piles but increasingly in the focus of research and

industry.

## 2.5  Pile capacities, stresses and friction fatigue

The capacity of a pile is defined as the maximum load which can be carried by a pile in axial or lateral direction without inducing an uncontrolled settlement or displacement of the pile. According to the direction of the applied load in relation to the pile axis, the pile capacity is divided into the "lateral" and the "axial" pile capacity (Fig. 2.3). The lateral capacity will not considered further in this paper. The axial capacity
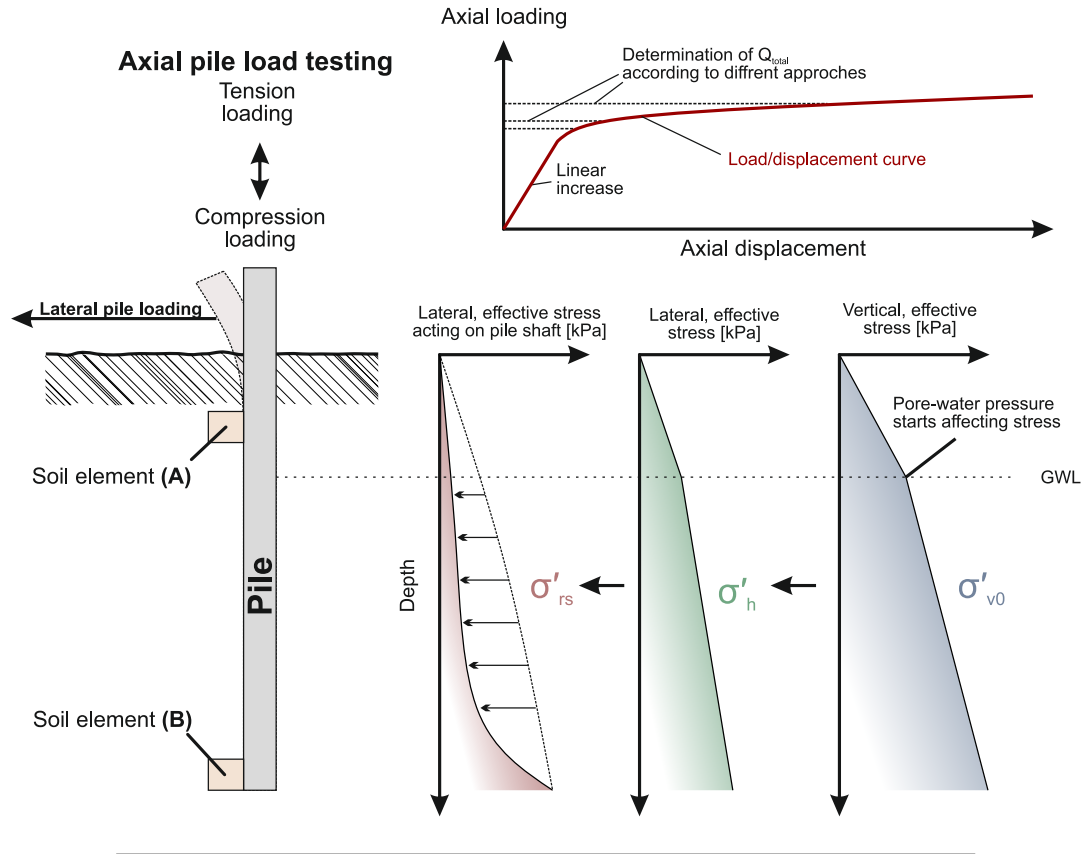


FIGURE 2.3: Simplification of stress distribution at the pile shaft and the determination of total pile capacity

of the pile is usually described as the total capacity $Q_{total}$, which is generally lower than the theoretical maximum capacity. A determination of $Q_{total}$ is accomplished in a best case scenario by interpreting the pile load-displacement curve, obtained by a static pile load test (see upper part of Fig. 2.3). Like shown in Eq. 2.2, the total capacity reflects the sum of the individual two capacities $Q_s$ (i.e. shaft capacity) and $Q_b$ (i.e. base capacity).

$$Q_{total} \quad Q_s \quad Q_b \tag{2.2}$$

The shaft capacity results out of the overall friction between the hole pile shaft and the surrounding soil Monzón (2006). Thus, the shaft capacity is given by the integrated skin friction $_f$ over the total embedded area of the pile. The second proportion contributing to total pile capacity, the base capacity, is developed by the interaction of the annular area of the pile with the soil underneath, following a bearing

failure in a first approximation (Monzón, 2006). In contrast to the shaft capacity – which is always activated independent to the load direction – the base capacity is set zero if the pile is tension loaded.

Chow et al. (1998) and Lehane et al. (1993) proposed the following expression to describe the unit skin friction $_f$ contributing to the shaft capacity (Eq. 2.3).

$$ _f \qquad _{rs} \qquad _{rd} \ \tan \ _{cv} \qquad\qquad (2.3)$$

Thus the shaft shear stress of an arbitrary point at the pile depends on the the constant volume interface friction angle $_{cv}$ and two horizontal acting stress components $_{rs}$ and $_{rd}$. The dilative stress component $_{rd}$ is generated by a dilative response of the soil surrounding the pile whenever the pile starts to move relatively to the soil. $_{rs}$ instead, should theoretically reflect the natural – free field – lateral acting effective stress in the ground $_h$, in turn coupled to the vertical, effective stress $_{v0}$. These relations are simplified at Fig. 2.3. However, since the coupling of the pile to the soil and its stress field is affected by pile installation, a bias between the far field stress in the ground and the stress effectively reaching the pile shaft arises (Fig. 2.3).

This is the reason why, for example, non-displacement piles like drilled piles mobilize a significantly reduced shaft capacity and have to dissipate most of their loads via the pile base. However, even for displacement piles where this coupling to the free stress field is significantly improved by laterally displaced soil, this bias still occurs. Known mechanisms such as the "friction fatigue effect" according to Jardine and Chow (1996) or alternatively called the "h/R - effect" according to Heerema (1978) are responsible for this. This effect describes, that a soil element loses continuously its ability to transmit incoming lateral stresses to the shaft if its distance to the pile toe $h$ is further increased. This inevitably happens when the installation process pile continues. The soil elements **A** and **B** at Fig. 2.3 simplifies this situation. Even if grain crushing effects and/or post-dilative contraction (Lim and Lehane, 2015) might be imaginable as potential mechanisms causing this friction fatigue effect, a clarification is still pending. Its negative impact on the lateral stress reaching the pile shaft instead could be already verified by numerous model-pile tests (White and Lehane, 2004; Gavin and O'Kelly, 2007; Yang et al., 2014).

## 2.6   Pile load testing

To determine the pile capacity $Q_{total}$ in practice, pile loading tests can be carried out. Furthermore, pile load tests are also necessary to determine the load-settlement relations of the pile foundation (Olgun, Yenginar, and Hanati, 2017). In a static pile loading testing procedure (SPL) – the standard for determining the pile capacity – the load at the pile head is increased incrementally by hydraulic stamps or applied weights. Simultaneously, the settlement (displacement) of the pile head is measured and plotted against the applied loads. Such a pile load-displacement curve is given in Fig. 2.3. It can be seen, that these load-displacement curves usually consist of a linear region merging into a non linear region for higher loads. To properly determine the total capacity ($Q_{total}$), large displacements are required. In practice, these large displacement cannot always be realized technically (Fellenius, 1991). For this reason,

numerous extrapolative methods like e.g. Brinch Hansen (1963) and Chin (1970) exist, to determine $Q_{total}$ even when the induced displacements are not sufficient for usual evaluations. If the load required to overcome linearity exceeds economical dimension (especially for large piles), a dynamic load test (DLT) can be performed. Thus, no static load is incrementally increased. In contrast, one strong impulse is introduced into the pile, e.g. by a hydraulic hammer blow. Analysis software is then able to model the dynamic pile capacity from the incoming impulse, its refraction and reflection, without the need for a more elaborated SLT.

Since the soil resistances are activated differently for both methods (dynamically and statically), SLT and DLT may develop slightly different $Q_{total}$'s even for an identical pile. These uncertainties are often unavoidable, but should be taken into account when comparing SLT and DLT results. Nevertheless, research by e.g. Likins and Rausche (2004) have shown that both methods tend to show at least values of a similar magnitude.

## 2.7 Piles and their offshore usage

The most demanding application of piles can be found in the offshore area as it handles enormous axial and lateral loads. Here, piles are used in various combinations to support wind turbines and thus to produce renewable electricity on the sea. Offshore wind energy is considered the most promising solution to satisfy climate-friendly human energy consumption in the future. This technology is relatively mature and very cost-efficient (GWEC, 2014). It is not unusual that a wind-driven turbine placed offshore, costs twice as much as the identical turbine placed onshore (Musial and Ram, 2010). This is explained by increased planning efforts, expensive foundations related installations/logistics and complicated grid connections (e.g. submarine cabling and offshore substations) . An economic incentive is, nevertheless, given as offshore plants benefit from stronger and more reliable blowing winds, less turbulence, and less citizen complaints (Oh et al., 2018). The foundation and its installation of such a wind turbine is one of the most difficult factors to estimate. It depends on water depth and on seabed characteristics. In shallow water, the foundation accounts for about 20% of the total cost of a wind farm (planning, logistics, installation). For increased water depth and more challenging soils, the cost-proportion can easily reach 36% (Swart et al., 2009). Especially the lateral acting forces due to wave impacts, water and air loads (Fig. 2.4) are a challenge for the foundation and the pile designing engineers. Whereas all other parts of the wind turbine (blades, rotor, tower, nacelle) can be manufactured consistently, the foundation has to be adapted always to the given environment. However, due to the high cost of the foundation and the technical maturity of all other components, the foundation offers perhaps the last link for a truly profound efficiency improvement in the offshore market.

The most popular of these foundations is the "monopile". It will account for about 81% of all offshore foundations in Europe by 2019, as it is easy to install and easily scalable (Ramírez Lizet, Fraile, and Brindley, 2020). Although monopiles were originally designed for shallower water depths (similar to gravity foundations or suction buckets), the industry is now able to bridge even water depths of up to $50\,m$, previously only handled by more complex structures such as jackets, tripods or floating foundations (Fig. 2.4). The TSPIC monopiles for the Guangdong Province (China) are currently (2021) considered the largest monopiles ever manufactured for a wind

turbine. With a mass of 1600 metric tons, a length of 100 meters and a diameter of 8.4 meter, they provide a good example of the size monopiles have already reached.
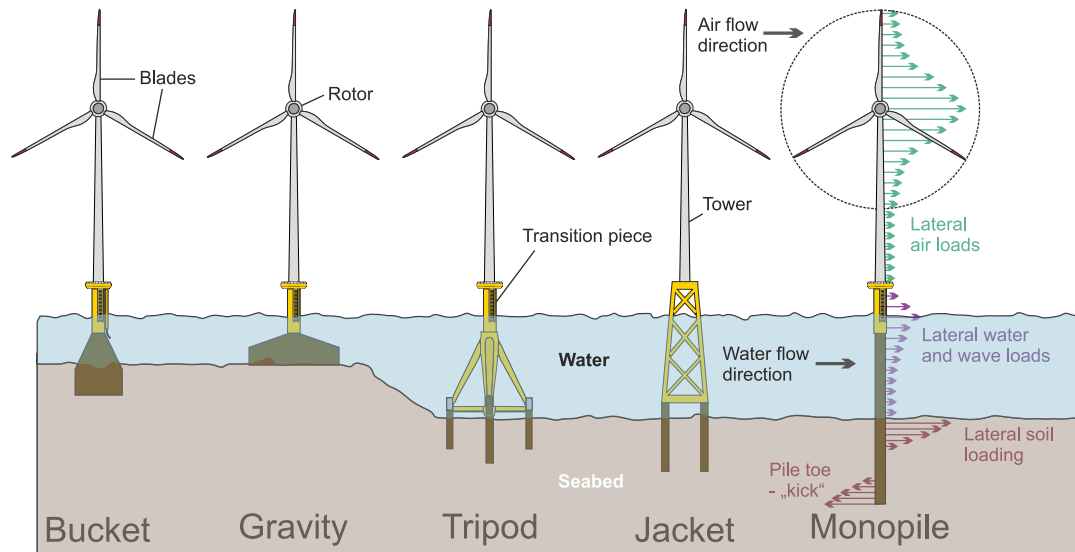


FIGURE 2.4: Wind turbine foundations in their offshore usage

## 2.8 The axial pile setup

### 2.8.1 Definition

Wendel (1900) was the first who reported that the capacity of piles might increase over time. The axial capacity of his timber piles, driven into a clay near Gothenburg (Sweden), showed a continuous increase of their axial capacity over a time of 3 weeks. In the following years, this type of capacity increase was demonstrated and reported for almost all types of driven piles around the world, whether they were installed in clay or sand, in the field, or under controlled laboratory conditions (e.g. Tavenas and Audy, 1971; Fellenius et al., 1989; York et al., 1994; Chow, 1996; Axelsson, 2000; Kolk, Baaijens, and Senders, 2005; Bullock et al., 2005b; Jardine, Standing, and Chow, 2006; Karlsrud et al., 2014; Lim and Lehane, 2014; Zhang and Wang, 2015; Carroll et al., 2017; Carroll et al., 2019; Anusic et al., 2019a). However, it was simultaneously recognized, that this increase in capacity does not occur for all piles. In some cases, the pile capacities remain either unchanged or even strongly reduced (Chen Yang, 1956; Miller, 1938). The process in which the axial capacity of the pile increases during their contact with the soil - was referred to as **pile setup**, where its opposing effect was named pile relaxation (Komurka, Wagner, and Edil, 2003). As the title of this work already reveals, the pile setup and its principles will be the main subject of the thesis on hand. The term "pile setup" is frequently used in combination with the term "pile aging". The use of "Pile aging" is a somewhat more ambiguous in the literature and describes a temporal process or procedure. It does not refer directly to a change of pile capacity, although this is often implied. "Aging" rather describes the process of a change in several aspects over a temporal component.

Pile relaxation, appears to be the exception rather than the rule and will not be considered further in this study.

### 2.8.2 Conceptual evolution of bearing capacity with time

One major phenomenon controlling pile setup is related to the nature of displacement piles and can be rationalized with respect to how a pile generates its capacity. During pile installation, the pile displaces the soil and pore-water as it reaches the saturated or partial-saturated zone. The displacement of both media is equivalent to the cross sectional area of the pile. While the soil grains are partially and the pore-water almost incompressible, the soil itself can become more densely packed (up to a certain point), if the pore-water can escape fast enough through the pores. If this escape is prevented or delayed, the pore-water pressure rises in an area close to the pile. The pore-water gradient decreases inversely proportional to the square of the distance from the pile (Pestana, Hunt, and Bray, 2002). This pore-water-pressure $u$ acts on the soil grain skeleton and reduces the effective stress (Terzaghi, 1925). As presented in chapter 2.5, this reduced effective stress, lowers the potential skin friction and thus the pile shaft capacity. The dissipation of this pore-water overpressure now temporarily controls the recovery of capacity, controlled in turn by soil parameters like soil permeability $k_f$, soil sensitivity $Si$ or the coefficient of consolidation $c_v$ (Soderberg, 1962). A larger cross-sectional area thus results in steeper pore-water gradients (Soderberg, 1962; Holloway and Beddard, 1995). Soils with lower $k_f$ values in turn, i.e. less permeable soils, slow down the equilibration of this gradient. Controlled by the $k_f$ parameter, this kind of setup can last days or weeks for clays, silts or mixed low permeable soils but just seconds for highly permeable materials like sands (Komurka, Wagner, and Edil, 2003). Especially since the capacity of a pile is often determined for the first time several hours or days after the end of driving (EoD), such pore-water effects are often already excluded. The initial capacity would then include a completed pore-water induced setup.

The fact, that nevertheless similar high capacity increases were observed in such high permeable soils even after years (e.g. Chow et al., 1998; Axelsson, 2000; Lim, 2013; Gavin et al., 2015; Gavin and Igoe, 2019; Anusic et al., 2019a; Carroll et al., 2019) reveal that one or more additional mechanisms have to influence the pile setup. Consequently, we have to distinguish between the pore-water induced – to some extend good understood and predictable – setup, and the subsequent, long-ranging – not fully understood, and pore-water independent – setup. The three setup phases after Komurka, Wagner, and Edil (2003) are suited for this kind of descriptive subdivision by setting a potential final pile capacity $Q_{Final}$ in relation to the capacity of the same pile immediately after end of driving $Q_{EoD}$ over time. This relationship is simplified in Fig. 2.5. Whereas the Phases 1 and 2 are related to pore-water dissipation effects, the principal and mechanisms leading to Phase 3 are still under debate. The time where the first two phases end and the third begins, is again controlled mainly by soil ($k_f$, $Si$, $c_v$), pile or installation properties (driving speed, cross-sectional area, plugging conditions). $t0$ at Fig. 2.5 marks the point in time where all pore-water effects are subsided. Thus, this point becomes important for further determination of setup proportions with respect to Phase 3 by providing a reference capacity to which any further capacity change can be referred to. Whether Phase 3 ever ends and a final capacity $Q_{Final}$ will be ever reached is also unknown. However, due to the logarithmic scaling of the x-axes in this simplification, capacity increases would get insignificant after only a few log cycles considering the life span of man-made structures. Due to the inhomogeneous nature of a natural soil, it is also very likely that some phase do overlap. As the soil properties vary vertically as well (Komurka, Wagner, and Edil, 2003), different parts of a pile would pass over from one phase to another phase at also different times. In the following, the present study will deal
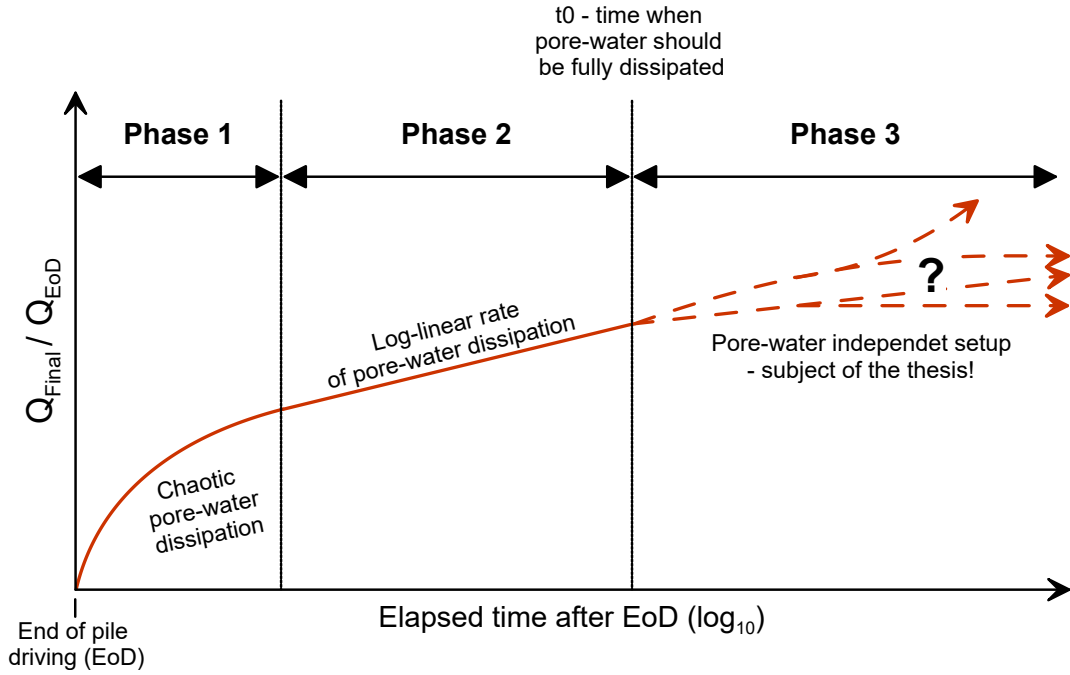
FIGURE 2.5: Simplified setup phases after Komurka, Wagner, and Edil (2003)

exclusively with effects related to Phase 3 of the setup, after pore-water effects have subsided. Since phases 1 and 2 account for the major part of the capacity increase in cohesive soils such as clays (Komurka, Wagner, and Edil, 2003), cohesive materials will also not be considered further.

### 2.8.3 Experimental evidence of pile setup

Early studies by, e.g. Tavenas and Audy (1971) observed axial capacity increases of up to +70% within 20 days after EoD for a medium dense sand. Numerous researchers and practitioners reported similar observations for a wide range of pile materials and soil types where notable examples observed increases in axial capacity of more or nearly +100% within 100 days after EoD (e.g. Jardine, Standing, and Chow, 2006; Karlsrud et al., 2014; Lim and Lehane, 2014; Carroll et al., 2017). In special cases, an increase of up to 12 times the initial capacity could be recognized (Titi and Wije Wathugala, 1999). An exemplary collection of setup cases in sand for a mixture of various driven pile types is presented in Fig. 2.6. The data is plotted together with three exemplary setup trends after the most common pile setup prediction approach after Skov and Denver (1988)(Eq 2.4).

$$\frac{Q_{ti}}{Q_{t0}} = 1 + A \log\left(\frac{ti}{t0}\right) \qquad (2.4)$$

This prediction approach assumes, that the setup ratio of a pile increases linearly over the decadic-logarithm of elapsed time after the reference time $t0$ in days. A dimensionless setup factor $A$, controls the slope of the straight. The setup ratio reflects the pile capacity $Q$ at a distinct time $ti$, divided by the initial capacity $Q_{t0}$ at the reference time $t0$. It can be seen, that the setup pile data does not follow any of the three exemplary given setup trends. In contrast, the setup data rather forms a strong
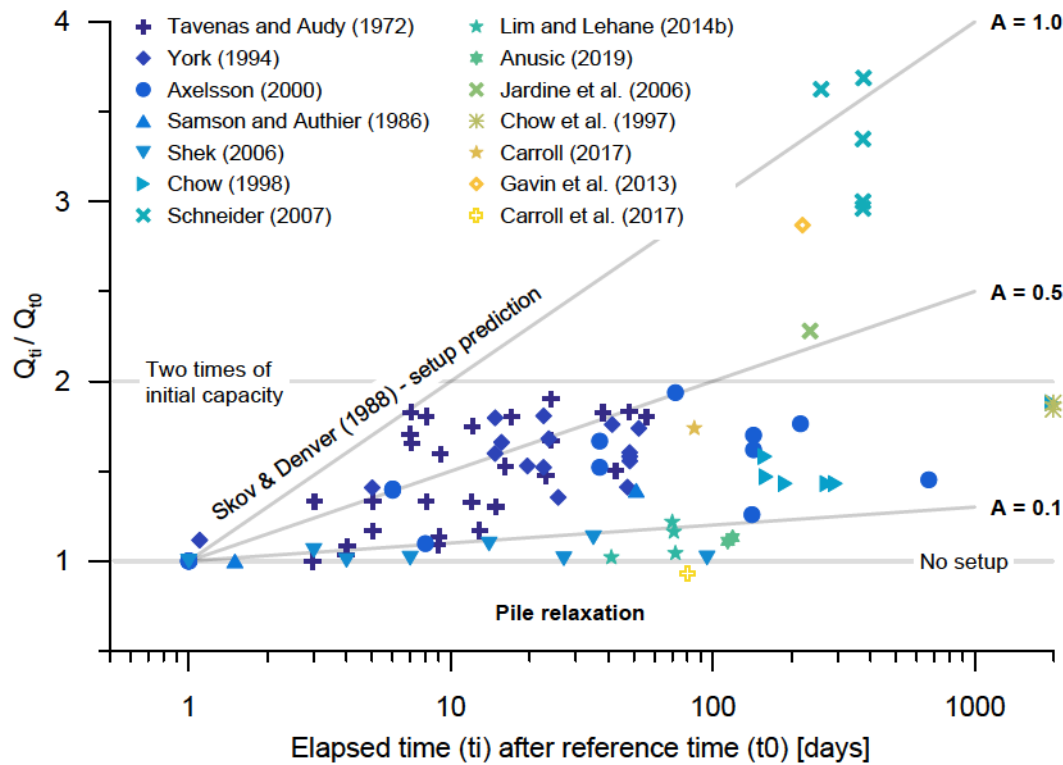
FIGURE 2.6: Case studies of pile setup in sandy soil. Extended compilation after Axelsson (2000) and Zhang and Wang (2015)

scatter pattern. This large scatter weakens the validity of existing setup characterization approaches (e.g. Skov and Denver, 1988) and justifies that standard pile design methods does not consider the setup effect explicitly. The setup factor may be in the range of $0.15 \leq A \leq 0.65$ for most cases (Fig.2.6) (Axelsson, 2000). Other authors suggested setup factors of $A = 0.5$ as the best fit of the data (Chow et al., 1998). The scatter of the observed pile setup was widely discussed. Thereby Lim (2013) and Bowman and Soga (2005) suggested that all case studies suffer at least one and often more of the following (slightly modified) limitations, which significantly add to the scatter:

- Mixing static and dynamic pile capacities

- Mixing tension and compression static load tests

- Inclusion of undesired pore-water effects by taking the measurements at the EoD as the reference capacity $t0$ (growth shares of Phases 1 and 2 at Fig. 2.5 are erroneously counted as part of Phase 3)

- Non-standardized determination of $t0$

- Under-mobilization of ultimate pile capacity in dynamic and static load tests

- Deficiencies during dynamic load testing for large diameter piles

- Uncertainties by separating shaft and base capacity

- Disruption of setup potential due to repeated testing procedures

While the accumulation of these purely methodological errors and uncertainties may account for some of the scatter shown in Fig. 2.6, these errors alone cannot explain the entire range of variability. That an unambiguous setup trend can be identified without these potential errors is also unlikely. Other effects more related to the soil, the pile itself, or the type of installation must also contribute to the unpredictability of this process.

### 2.8.4   What we know

Some important aspects about the setup in granular soils could be elucidated by scientific studies over the last decades, including most notably:

1. Setup seems to be mostly driven by shaft capacity increases, the base capacity is not effected at all or even slightly reduced (Airhart, Hirsch, and Coyle, 1967; Skov and Denver, 1988; Preim, March, and Hussein, 1989; Shioi et al., 1992; Axelsson, 2000).

2. Setup seems to be limited to displacement piles. Replacement piles like drilled piles do not show any setup (Chow et al., 1998).

3. The laterally acting, static stress around a displacement pile was found to increase for some cases (Ng, Briaud, and Tucker, 1988; Chow, 1996; Axelsson, 2000).

4. Setup was observed for all pile materials like for wooden, concrete or steel piles (Tavenas and Audy, 1971; Preim, March, and Hussein, 1989; Chow et al., 1997; Rimoy et al., 2015).

5. Setup was found to take place for saturated or just partially saturated soils as well for piles installed underneath or above the saturated zone (Jardine et al., 2015; Carroll et al., 2017).

6. In a direct comparison, setup seems to be reduced if the pile is protected against an acting corrosion, i.e. if the pile is made of stainless steel – for example – rather than of mild steel (Carroll et al., 2019).

7. Setup seems to be related to the size of the pile or driving equipment. Setup is hard to detect for small size piles under laboratory conditions and very pronounced for medium size piles under field conditions (Zhang and Wang, 2015; Shek, Zhang, and Pang, 2006).

8. Setup will be reduced if the pile resting phase is disturbed by repeated testing. The highest setup trends have been measured if a number of identical piles next to each other are tested just once for different times (virgin or fresh-pile testing procedure) (Jardine, Standing, and Chow, 2006).

9. Large-strain cyclic loading lowers the pile setup potential, small-strain cyclic loading instead, amplifies the setup (Jardine, Standing, and Chow, 2006; White and Zhao, 2006; Tsuha et al., 2012).

10. Setup seems to be related to the installation process of the pile. When a pile is driven with more blows i.e. more disturbances, its initial capacity is reduced but its setup instead, seems to become more pronounced (Lim and Lehane, 2014; Anusic et al., 2019a).

### 2.8.5 Setup as a capacity gain - theory A

Most of the traditional understanding and imagination of the setup mechanism are based on Chow's very detailed dissertation (Chow, 1996), which summarizes nearly a decade of scientific research on the subject (1988 - 1996). By postulating three sub-mechanisms that potentially affect the setup in various combinations, she was able to explain most of the known phenomena from the 2.8.4 section. These sub-mechanisms still form the basis of most recent scientific publications on this subject but are increasingly less able to withstand more recent scientific findings.

**Redistribution of radial effective stresses as a consequence of degrading hoop-stresses and creeping**

Chow (1996) postulated, that during the pile installation and the related lateral soil displacement, the sand grains in direct vicinity would create a "sleeve" of loose sand, followed by a densified "arch" (Fig. 2.7). This arch deflects the radial acting stress $\sigma_{rc}$ around the pile creating a circumferential acting "hoop" stress. Over time, these arches might be waked by micro-mechanical soil movements (i.e. creep), leading to a continuously rising $\sigma_{rc}$ and an increasing shaft resistance. In such manner, the increasing lateral stress observed over time by Ng, Briaud, and Tucker (1988), Chow (1996), and Axelsson (2000) as well as the setup observation 2 at section 2.8.4 could be explained. It would also explain why the setup does not take place for drilled or replacement piles (observation 3) as lateral soil displacement would not occur for these installation methods. This theory further provides at least a partial explanation for observation 1, 4 and 5. Contradicting evidence exists from recent instrumented pile tests conducted by Gavin, Igoe, and Kirwan (2013), Lim and Lehane (2015), and Gavin and Igoe (2019) who measured only a small increase or even a slight reduction of $\sigma_{rc}$ over time. It is possible, however, that in all these cases precise measurement of stress gradients were prevented by methodological limitations (e.g. stress transducers were shielded by corrosion products). Furthermore, uncertainties regarding lateral stress measurements would not be surprising, because they are considered to be among the most difficult measurements in geotechnical engineering (Prof. Dr.-Ing. Roberto Cudmani; personal communication). On the other hand, if the ratio of the pile diameter $D$ to the mean grain size $D_{50}$ of the surrounding soil rises, it becomes unlikely that these arches would remain stable.
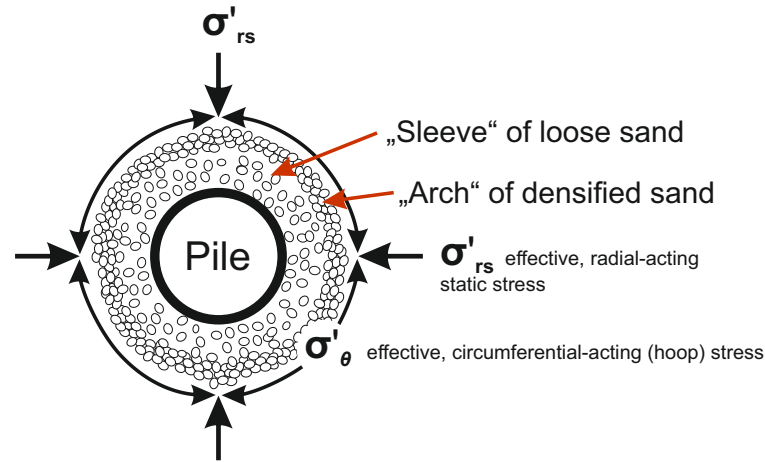
FIGURE 2.7: The arching setup theory, simplified after Chow (1996)
and Chow et al. (1998)

**Enhanced dilative response at the pile-sand interface - soil aging**

Chow (1996) alternatively proposed, that next to the radial, static-acting stress $\sigma_{rs}$ the dilative stress component $\sigma_{rd}$ at Eq. 2.3 – mobilized if the piles is loaded due to interface shearing failure – holds an additional potential to increase pile capacity. Microstructural re-arrangements and a better grain interlocking would result in a stiffer, more dilative fabric of the pile surrounding soil over time while maintaining the actual void ratio mostly unchanged (Zhang and Wang, 2016). Lehane et al. (1993) and others suggested a mathematically description of $\sigma_{rd}$ using the cavity expansion theory after Eq. 2.5.

$$\sigma_{rd} \approx 2G \frac{\Delta r}{R} \tag{2.5}$$

In accordance to this definition, the stiffness $G$ has to be increased due the normally constant pile radius $R$ and the interface dilation $\Delta r$. Alternatively, an increase of the surface roughness to pile radius ratio $\Delta r \cdot R^{-1}$ would translate to an equivalent increase of $\sigma_{rd}$. Interface shear experiments by Chow (1996) demonstrated such an increases of $\Delta r$ and $G$ over aging periods from less than 1 h up to 63 days. These findings are supported by shear wave velocity gains and stress-redistributions observed by Zhang and Wang (2015). They further indicate, that the soil stiffness might increase over time. Axelsson (2000) or Gavin and Igoe (2019) demonstrated in a number of instrumented pile tests, that the overall lateral stress at failure $\sigma_f \approx \sigma_{rs} + \sigma_{rd}$ increases after a certain aging time. Such a temporal change in soil properties or responses are often referred to as "soil aging". A stronger dilative response of the pile during loading would provide an explanation for observation 4 and 5. In contrast, it does not provide a clear solution for observation 2. In addition, the inverse proportional relationship to the pile radius at Eq. 2.5 would suggest, that smaller piles would tend to a more pronounced setup. However, when the size of a pile already exceeds a laboratory pile dimension 7, this size dependence no longer appears to exist Chow et al. (1998).

**Physicochemical processes affecting the pile shaft - corrosion and/or cementation**

Chow's third assumption about what effects might control the general pile setup takes a different approach than the previous two. Instead of focusing on possible options to control the stress acting in the soil or during pile loading, this theory focuses on the frictional properties acting between the pile and the surrounding soil. Physicochemical processes, such as the corrosion of a steel pile or the frequently observed incrustations (e.g. Gavin and Igoe, 2019), are supposed to change or increase the roughness of the pile surface. A rougher pile shaft should theoretically lead to a higher shear strength in the same stress field, i.e. under a higher interface friction angle $_{cv}$ (see Equation 2.3). Physicochemical processes around the shaft were questioned in the past. Gavin et al. (2015) argued that physicochemical processes around the shaft are a mechanism that is unlikely to control the setup as capacity increases are also documented for wooden and concrete piles (observation 4), for which no corrosion would be expected under normal conditions. In contrast, other studies (e.g. White and Zhao, 2006; Lehane et al., 2012; Carroll et al., 2017) considered corrosion as the dominant mechanism controlling their setups. Physicochemical processes affecting the pile shaft would provide an explanation for observation 6.

### 2.8.6 Setup as a result of stress equilibration - theory B

A new perspective of the pile setup was provided by Lim and Lehane (2014) and has been subsequently adopted by Zhang and Wang (2015). They moved away from defining the setup as a process of capacity gain (as defined by Chow, 1996) to one that is rather defined by soil recovery. The amount of soil recovery has been associated by the authors with the soil disturbance induced during pile installation. According to Lim and Lehane (2014), the ground disturbance is controlled by the installation method and this in turn by friction fatigue (Section 2.5) but first of all by pile characteristics, i.e. whether the pile is open- or closed-ended. Subsequently, a pile installation with higher potential for soil disturbance – such as the installation of a closed-ended impact driven pile – would lead to a more disturbed stress field – compared to a jacked open- or closed- ended pile. Consequently, the initial pile capacity would be reduced but followed by a more pronounced subsequent setup. The authors argued that these micro-mechanical inhomogeneities (i.e. disturbances) reequilibrate with time. As a result, the radial effective stress acting on the pile shaft ($_{rs}$) as well as the stiffness ($G$) response of the pile during loading are increased. This theory rationalizes the stress field more as a thermodynamic system evolving towards equilibrium, but nonetheless in explaining the observations 1-5 without the need for additional, not verified phenomenas like arching or creeping. The peculiarity of this theory is not that it tries to completely reinvent the wheel, but merely looks at the same observation (i.e. increased radial acting stresses or dilative responses) from a different point of view. It also postulates, that the capacity of a pile will not grow endlessly, but instead, it will reach a natural upper limit controlled by the dimension of the pile and the soil properties. At this point, the disturbances induced by pile installation are dissipated and an equilibrium is reached. This theory has been partially confirmed and extended by field experiments conducted by Anusic et al. (2019a). These authors encoded the amount of disturbance by the number of blows during installation, divided by the effective shaft area of the pile $N_{bA}$. Anusic et al. (2019a) demonstrated, that a higher $N_{bA}$ induced by the use of closed-ended piles or the utilization of an air hammer (instead of a heavy drop weight) lead to

a reduced initial pile capacity, close to EoD. Subsequently, the pile setup was more pronounced for these high $N_{bA}$ piles, confirming the assumption of Lim and Lehane (2014). However, Anusic et al. (2019a) were not able to prove that this relationship still holds for vibratory driven piles. Due to their cyclic nature, the highest $N_{bA}$ - values for all known installation methods would be obtained with pile vibration.

## 2.9  Motivation and hypothesis

Following the outlined state of knowledge the following three major considerations constituted the motivation for the work conducted in the framework of this thesis: (1) Additional and suitable datasets are required to enable a proper assessment of the extent, to which variations in the pile installation method and pile material affect initial capacity and setup. (2) Insufficient data is available to evaluate whether the setup of large-diameter piles is similarly affected by a variation of the installation methods as small-diameter piles. (3) It is not well understood up to which extend corrosion or incrustations of the pile shaft contribute to the setup effect.

All three aspects effectively limit our understanding of the setup and consequently the potential efficiency of pile foundations. In a world of dwindling resources heading towards a climate catastrophe it is crucial to eliminate such inefficiencies. Piles, which are frequently used as foundations for offshore wind turbines will play an important role in escaping this crisis and hence their construction and design will have to be as efficient as possible.

To improve our understanding of the setup effect and its principles the following research hypothesis were defined:

1. The usage of pile vibration as an installation method generally leads to higher disturbances of the subsoil than induced by impact driving. Therefore, the initial bearing capacity of vibrated piles should be significantly reduced compared to impact driven equivalents. However, these vibrated piles should show a increased setup potential. A different behavior instead would not be in accordance with the stress equilibrium theory after Lim and Lehane (2014).

2. Larger piles require also a more powerful i.e. more soil disturbing driving equipment. If the understanding of disturbance after Lim and Lehane (2014) would be solely responsible for the setup – without the extensions made by Anusic et al. (2019a) – differences in setup between piles driven by divergent installation methods should be amplified if the pile size increases.

3. The physico-chemical processes like corrosion and the associated formation of pile adhering sand crusts (incrustations) influence many factors that contribute to pile capacity (e.g. $_{rd}$, $_{cv}$, surface roughness or $D$). Such an influence on primary capacity controlling parameters must have a more significant impact on pile capacity that previously assumed.

In the following chapters of the thesis, these hypothesis will be investigated but limited to the dense sand states encountered at pile-test site in Cuxhaven, northern Germany.

# Chapter 3

# Methods

## 3.1 Cone penetration testing

Cone penetration testing (CPT) is a powerful in-situ method for sub-soil characterization. By pushing an extended cone penetrometer into the soil at a constant rate, sensors record the tip resistance $q_c$, the friction at the sleeve $f_s$, and the pore-water pressure $u$ continuously (Fig. 3.1). A cone penetration test rig works comparable
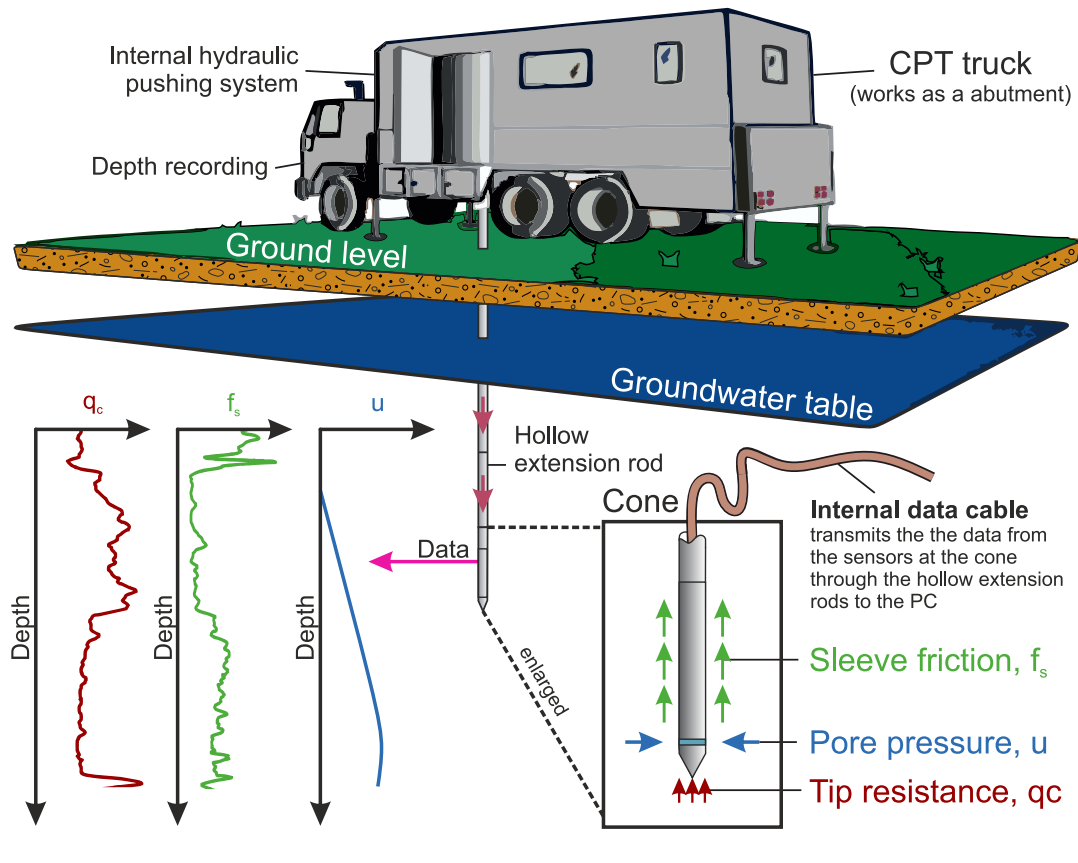


FIGURE 3.1: Working procedure of cone penetration testing

to a counterweight or abutment. Due to the interaction of tip and sleeve resistance and the resulting friction ratio, the soil can be classified in-situ without the need for expensive drilling (e.g. Robertson et al., 1986). Furthermore, the use of repeatable information about soil strength and compressibility generated by cone penetration testing, leads to an increased pile design reliability (Briaud and Tucker, 1988). Therefore, especially the tip resistance is used by many approaches (e.g. ICP-05 or UWA-05) in combination with material laws for pile capacity prediction (see e.g Schneider,

Xu, and Lehane, 2008). CPT was included in all three sub-studies for pile capacity prediction and for soil classification. During field work, ICONE system with a cross-sectional area of 15 cm$^2$ from A.P. van den Berg was used. $q_c$, $f_s$ and $u$ - were saved in 2 cm depth intervals.

## 3.2  Pile capacity prediction

The ICP-05 and UWA-05 approaches were firstly presented in the 22nd edition of the API recommendations (API, 2006). They were developed by Jardine et al. (2005) at the Imperial College and by Lehane, Schneider, and Xu (2005) at the University of Western Australia. Both approaches are the most frequently applied ones and known for their good match between predicted and measured pile capacities (Moshfeghi and Eslami, 2018a; Schneider, Xu, and Lehane, 2008). Beside alternative approaches like e.g. NGI-05 or API-00, the ICP-05 and UWA-05 methods also account for material laws like Mohr Coloumb (Eq. 2.3) or the cavity expansion theory (Eq. 2.5) in their equations. With these empirical relations and additional soil parameters like the interface friction shear angle $_{cv}$, the transformation of in situ cone resistance data into the skin friction can be established. Nevertheless, numerous effects like friction fatigue or plugging are still under debate and cannot easily put into a mathematical relationship. As a result, these approaches were also developed on an iterative way. After providing the mathematical framework following the understanding of the authors, they were equipped with calibration factors and fitted against a broad database. Hence, the quality of the predictive models directly depends on the quality of the database against which they were calibrated. These models are used in all three studies, e.g. for normalization. By normalizing a measured pile capacity to its predicted UWA-05 or ICP-05 capacity, the impact of already known capacity-influencing factors – already accounted for in the existing equations – can be reduced. Leftover impacts can be simultaneously amplified and might lead to the identification of unknown influencing factors. The equations for both approaches can be found in Section 6.4.6.

# Chapter 4

# Installation and small pile aging effects

This study – Busch et al. (2022) – was submitted to Geomechanics for Energy and the Environment on September 23th (2021) and was accepted for publication on April 19th (2022).

## 4.1 Authors

1. **Alexander V. Busch**[1]

2. **Max O. Kluger**[1,2]

3. **Daniel A. Hepp**[1]

4. **Majid Goodarzi**[1]

5. **Stefan Kreiter**[1]

6. **Tobias Mörz**[1,3]

[1]MARUM – Center for Marine Environmental Sciences, University of Bremen, Bremen, Germany
[2]School of Science/Te Aka Mātuatua, University of Waikato, Hamilton, New Zealand
[3]Geo-Engineering GmbH, Bremen, Germany
Corresponding author: abusch@marum.de

## 4.2   Abstract

Pile setup is not fully understood, despite its high potential for cost saving and risk mitigation in onshore and offshore constructions. Studies indicate that the pile installation process has important influence on initial pile capacity and the subsequent setup. However, only few studies considered a wide range of installation methods (e.g., impact driving, jacking or vibratory pile driving) when quantifying both initial capacity and setup characteristics. This study presents data of 88 static tension load tests conducted on 44 small piles at 1, 2, 10, and 100 days after their installation by four different methods. Piles made from mild and stainless steel exhibit strongly divergent setup characteristics, being a result of their different resistance to corrosion. Additional factors governing setup are the number of shear cycles induced during pile installation and the elapsed time after end of driving. We suggest a new approach considering the setup as a multidimensional effect, enabling the prediction of the initial capacity of a pile and its temporal development for the tested boundary conditions. This study provides a significant contribution to the understanding of the mechanisms governing setup by combining existing conceptual models, as friction fatigue and stress re-equilibration, together with corrosion under a time perspective.

## 4.3   Introduction

Uncertainties in capacity prediction and setup (i.e. capacity increase over time) of displacement piles increase the risk and costs in civil engineering projects. A forecast of initial axial capacity of piles installed by impact driving can be achieved by prediction methods based on cone penetration tests (CPTs) (Schneider, Xu, and Lehane, 2008; Moshfeghi and Eslami, 2018b). Recent prediction methods are specified in the American Petroleum Institute's design code (API, 2006) and are now partly implemented in the standard procedure in geotechnical engineering. In contrast, a prediction of pile setup is still hampered by numerous uncertainties about its causing mechanisms and by the large scatter of pile setup observations in existing databases (Lim, 2013). As a result, pile setup predictions have yet not been fully considered in daily engineering practice. Additionally, Lim and Lehane (2014) and Anusic et al. (2019a) demonstrated in their studies that the use of different installation methods (e.g., impact driving, jacked piling) directly affects both initial pile capacity and pile setup. The different initial pile capacities and observed setup were considered to reflect the number of shear cycles during pile driving, which vary between the installation methods (Anusic et al., 2019a). This underlines that neither initial pile capacity nor pile setup characteristics can be sufficiently predicted when the piles are not installed by the traditional way of impact driving. An alternative installation method is vibratory pile driving. This method features faster drivability, better pile handling, less noise emission, and reduced material fatigue compared to the conventional method of impact pile driving (Elmer et al., 2007; Chung, Wallerand, and Hélias-Brault, 2013). These advantages provide a high potential in cost reduction, especially for the offshore renewable energy industry, which depends on the installation of large-sized piles. A better understanding of the interrelation between different installation methods, initial pile capacity, and pile setup would allow for a more efficient pile design and thus to significant economic benefits for project developers and investors. This study aims for better understanding the effect of installation methods on initial pile capacity and pile setup. For this purpose, the change in

pile tension capacity over time was measured in a long-term field experiment using a high number of small piles driven by one of four different installation methods. 44 close-ended piles with a diameter of 35 mm were installed to a maximum penetration depth of 12.1 m in a very dense natural glaciofluvial sand deposit at a sand pit in Northern Germany (Fig. 4.1). Impact driving, pile jacking, and two scenarios of vibratory pile driving were used to install piles into the ground. The four installation methods vary with respect to the number of shear cycles the soil experiences during pile installation. Furthermore, the influence of potential corrosion was investigated by using two different steel qualities (i.e. mild steel, stainless steel). Because pile setup has been observed to affect pile shaft capacity alone (Skov and Denver, 1988; Axelsson, 1998) the piles in the present study were tested by static tension load tests. The testing concept addressed the following three questions:

1. How does a variation in installation method affect the initial capacity of displacement piles?

2. How does a variation in installation method affect the pile setup?

3. To what extent does the axial pile setup depend on potential corrosion of the pile material?

The onshore test site comprises dense glaciofluvial sands and can be seen as an equivalent to subsoils in the North Sea. The test site was also selected for two large-scale vibratory pile driving projects in the past, namely the VIBRO and VIBRO-REStrike project. Together with the present study and numerous similar geotechnical investigations, this onshore test site may be considered as one of the best investigated pile testing sites in the world (e.g. Gattermann, Herwig, and Moormann, 2015; Biryaltseva et al., 2016; Goodarzi et al., 2019; Quinteros et al., 2018; Achmus et al., 2020; Al-Sammarraie et al., 2020).

## 4.4   Study site

The study site is located in a sand pit at the northern part of the Cuxhaven - Bremerhaven ridge  7 km south of Cuxhaven, north Germany (Fig. 4.1A). The ground level of the test site will be used as a reference and is at an average height of 7.8 m above sea level. An anthropogenic layer 30- to 45-cm-thick of recycled sub-grade material builds up the topmost stratigraphic unit (Fig. 4.2A). The underlying natural glaciofluvial dense to very dense sand layers were deposited during the Middle Saalian ice advance of the Quaternary (Sindowski, 1963; Ehlers, 1990). They are mostly horizontally stratified and exhibit internal crossbedding of different dimensions from decimeters to meters. This crossbedding generates a certain degree of uncertainty when comparing cone penetration tests (CPT) performed throughout the test site (Al-Sammarraie, 2020). At around 4 m below ground level (mbgl), these sand deposits are interlayered with a 0.5 to 1.5-m-thick Saalian till layer composed of clayey silty sands and gravel. The water table is commonly located above the till layer at a depth of     3.5 mbgl but is subjected to seasonal and also daily fluctuations The groundwater can be classified as fresh water with chloride concentrations of     $50\ mg\ \ l^{-1}$ (González et al., 2021). The soils above the ground water table can be considered as moist but not fully saturated on an annual basis with water contents of 18-20% (Geo-Eng, 2014).
Sediment description, grain size analyses (DIN 18123, 2011), and minimum and maximum void ratios (DIN 18126, 1996), obtained from two boreholes near the test

site (SAM 1 & SAM 2), characterize the subsoil in the present study (Fig. 4.1 & Fig. 4.2A-C) (Geo-Eng, 2014; Geo-Eng, 2015). From ten cone penetration tests performed throughout the test site (Fig. 4.1C), cone resistances vary from few hundreds kPa for the till layer to maximal values of 45 MPa for the very dense sand intervals (Fig. 4.2 D). Considering the cone resistance – relative density relationship of Baldi et al. (1986), the sandy subsoil profile at the test site is classified as "very dense" for about 70% of the installation depth (Fig. 4.2E).
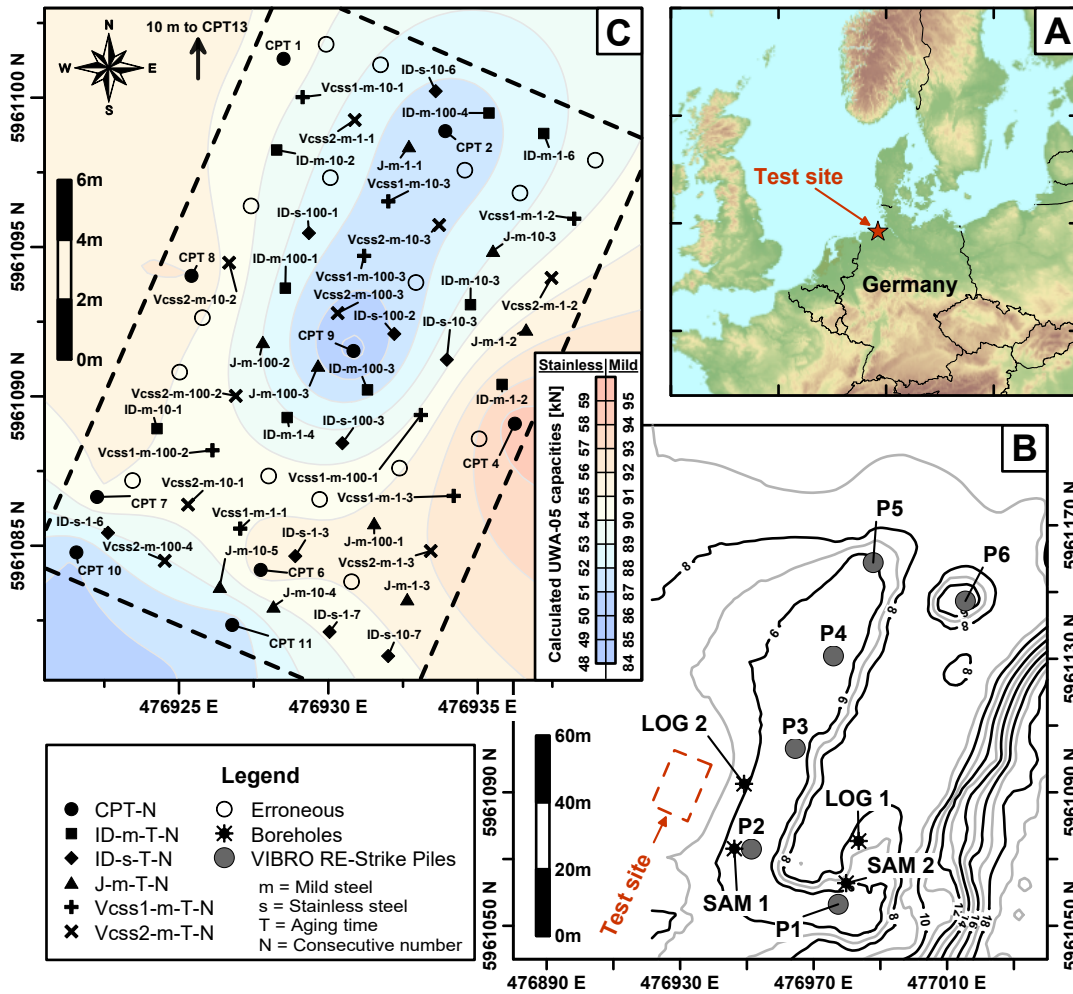


FIGURE 4.1: **A:** Location of the test site in Northern Germany. **B:** Location of test site with respect to VIBRO RE-Strike piles (P1-P6) as well as to the position of stratigraphic boreholes (SAM 1, SAM 2) and geophysical downhole logs (LOG 1, LOG 2) used to derive geotechnical and stratigraphic properties. **C:** Test layout of micro piles, overlain by the kriged pile tension capacity predictions calculated by the UWA-05 approach (Lehane, Schneider, and Xu, 2005) and based on static CPTs. Abbreviations of each test setting are explained in the text. Kriging was done by Golden Software Surfer using the following settings: component type = linear; anisotropy angle = 0; anisotropy ratio = 1; variogram slope = 1. Coordinate system: World Geodetic System 1984, Zone 32N. Source of map data: EuroGeographics for the administrative boundaries and the European Environment Agency (EEA) for topographic map.
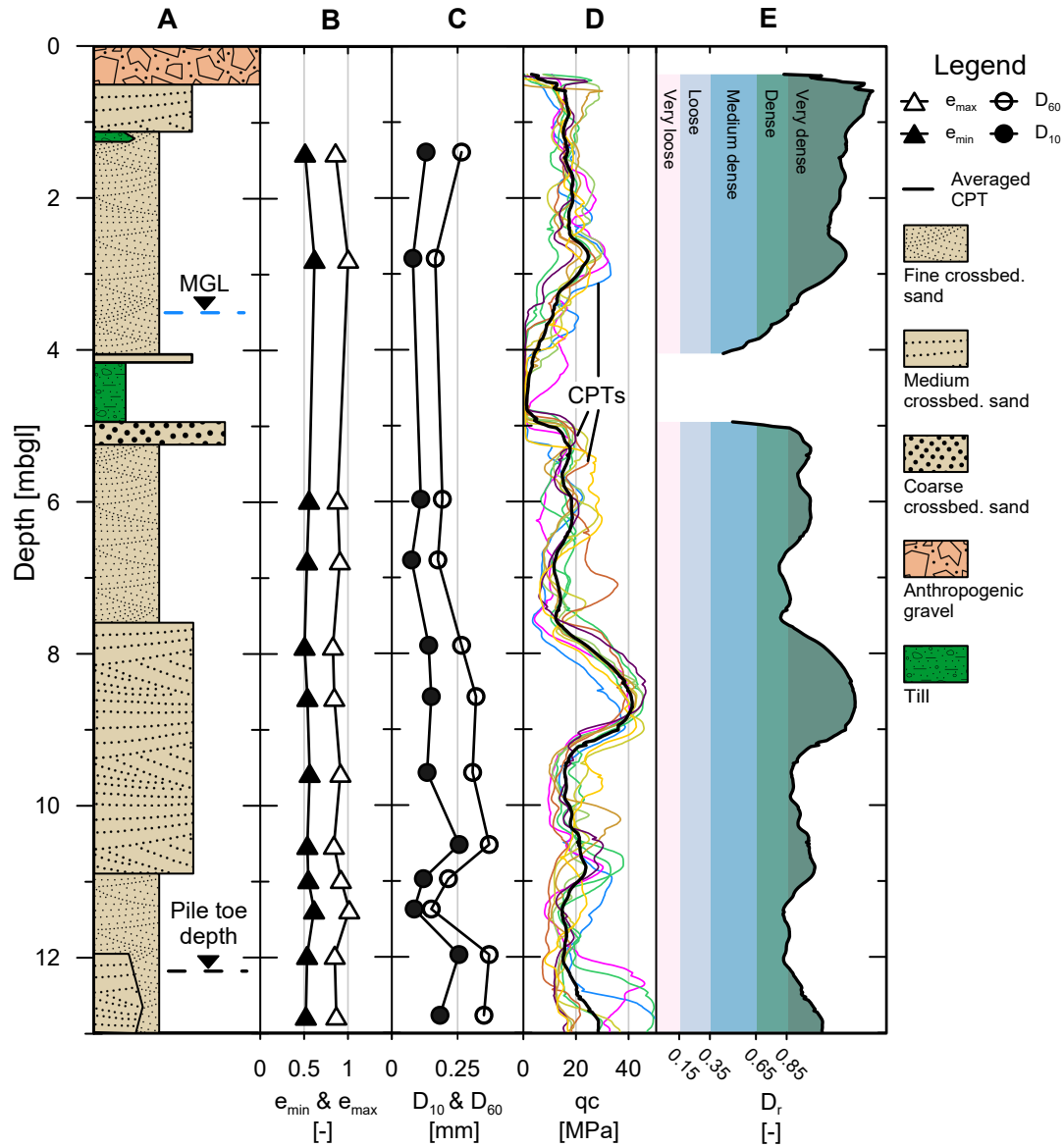
FIGURE 4.2: **A:** Lithology from borehole data SAM1 and SAM2, provided by Geo-Eng (2014) and Geo-Eng (2015). Layer boundaries are slightly depth-shifted in respect of static CPTs. MGL - mean groundwater level. **B:** Void ratios determined following DIN 18126 (1996). **C:** Grain size parameters determined following DIN 18123 (2011). **D:** Cone resistance of CPTs. **E:** Relative density calculated after Baldi et al. (1986). Colors represent the different grain size classes following DIN EN ISO 14688-2 (2020).

## 4.5 Methods

### 4.5.1 Installation concept and pile material

In the present study, 44 steel piles were installed in a rectangular grid (Fig. 4.1C) using one of four different installation methods: impact driving (ID), jacking (J), and vibratory driving with two different cyclic strain scenarios (Vcss1, Vcss2). The minimal spacing of 100 cm between piles and CPTs was chosen to minimize any interaction from the neighboring piles and CPTs following the recommendation of Al-Sammarraie (2020). The piles had an outer diameter of 35 mm, were closed-ended, and segmented into one-meter-long pieces. The pile segments were connected by headless screws and assembled with a fixed torque of 30 Nm. The pile toes comprised 60-degree cones in order to facilitate pile driving. 35 piles were constructed from mild steel (material number 1.0546 following DIN EN 10027-2 (2015), a steel type common in offshore pile foundations and not resistant against corrosion. In the following, tests with mild steel piles are labeled with an "m" hereafter. Nine piles were constructed from stainless austenitic steel (material number 1.4404 following DIN EN 10027-2 (2015) to exclude the influence of corrosion on test results. The stainless steel piles are labeled with an "s" hereafter. The final penetration depth was 12.1 m below ground level. For every pile, a 30- to 45-cm-long casing was used in order to avoid potential effects of the anthropogenic gravel layer and to provide a frictionless access to the natural sand deposits underneath (Fig. 4.3). The arithmetic average height parameter also known as center line average roughness $R_{CLA}$ after Gadelmawla et al. (2002) of both steel types were determined using a digital microscope (VHX 6000, Keyence) and was used for later capacity normalization. The center line average roughness for each steel type is summarized in Tab. 4.1. Some pile segments were reused for subsequent piles in order to reduce costs. After piles were extracted from the ground, they were carefully examined for potential changes that could have affected the pile capacity of subsequent piles. Pile segments were only reused, if they did not show any signs of surface deformations, such as scratches, corrosion, changes in color, and bending of entire segments.

TABLE 4.1: Use and properties of the steel types

| Steel type | Material No. | $R_{CLA}$ | Installation method | | | |
|---|---|---|---|---|---|---|
| | | | ID | J | Vcss1 | Vcss2 |
| Mild steel | 10,546 | 6.9 μm | x | x | x | x |
| Stainless steel | 14,404 | 2.9 μm | x | - | - | - |

Material number following DIN EN 10027-2 (2015).
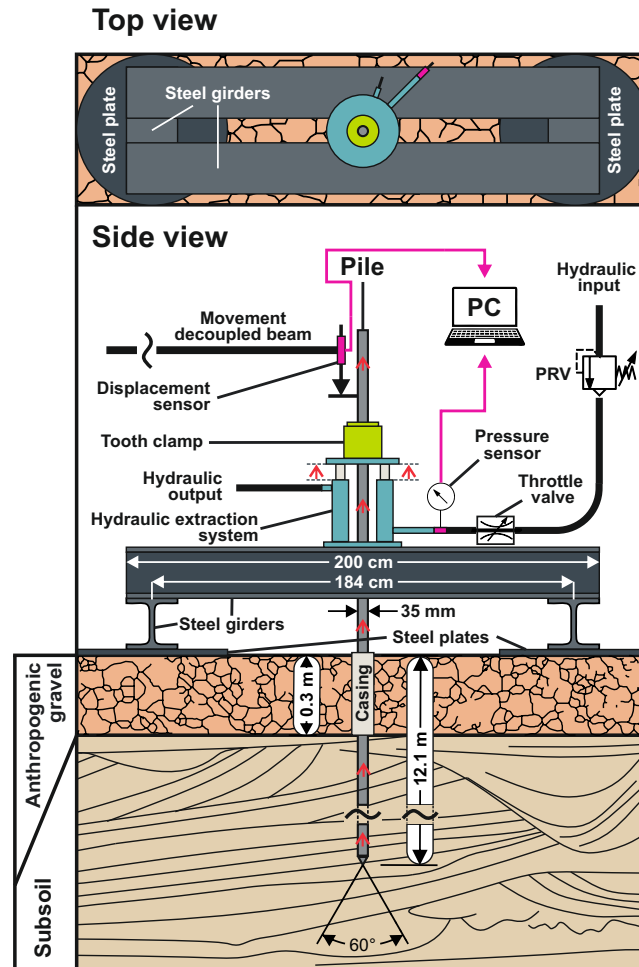
FIGURE 4.3: Technical design of tension loading. PRV - pressure relief valve.

### 4.5.2 Installation methods

Impact driving was performed using a standard rig for cone penetration testing. The rig was equipped with a free fall weight of 124 kg, which was dropped from 0.5 m. The pile head was guided along the mast of the rig to avoid lateral pile deflection. The top of the pile was equipped with a custom-made brass collar, which provided sufficient transmission of impact energy and prevented deformations at the pile top. Pile jacking was performed with a strain controlled hydraulic CPT jacking frame commonly used on CPT trucks. The penetration length of each push was between 0.5 and 1.2 m at a constant penetration rate of 20 mm/s. Vibratory pile driving was performed by a strain controlled hydraulic piston (Al-Sammarraie, 2020). Two different cyclic strain scenarios were used for vibratory pile driving. Both cyclic strain scenarios had the same single-displacement amplitude of 5 mm at a constant frequency of 20 Hz. This frequency is typically used for offshore and onshore installation of large piles (Rodger and Little John, 1980; Abdel-Rahman, 2011). In the first cyclic strain scenario (Vcss1) the pile was pushed at a constant penetration rate of 20 mm/s. In the second cyclic strain scenario (Vcss2) a larger penetration rate of 40 mm/s was used instead, thus reducing the number of shear cycles by 50%. The number of shear cycles necessary to install a pile up to its final depth per unit pile

mantle area, $N_{bA}$, has been used in the following to code each installation method with just one parameter (Eq. 4.1) following suggestions of Anusic et al. (2019a). Schematic penetration paths of the four installation methods are presented in Fig. 4.

$$N_{bA} = \frac{number\ of\ shear\ cyles}{effective\ mantle\ area\ [m^2]} \tag{4.1}$$
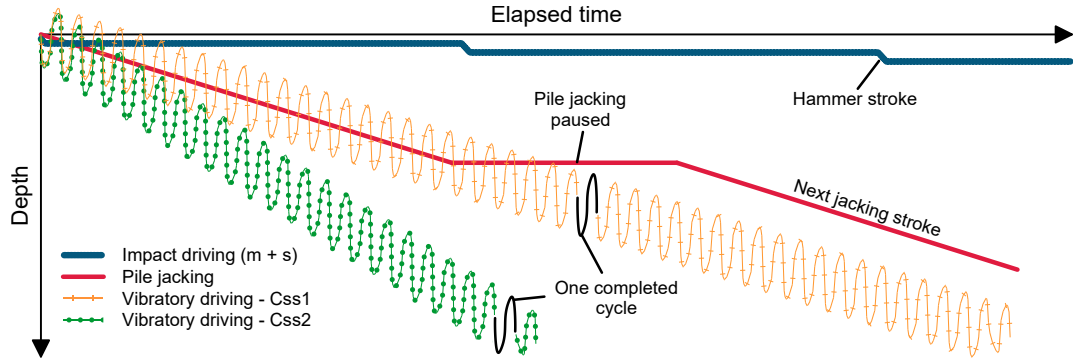


FIGURE 4.4: Simplified cyclic path of pile toe for each of the four installation methods.

### 4.5.3   Static tension loading procedure and data acquisition

Following recommendations of Bullock et al. (2005a), a reference time of 24 hours after end of driving (EoD) was defined to allow full pore water pressure dissipation (Fig. 4.5). Pile capacity was determined by performing a static tension load test using a hydraulic extraction system. Pile load was controlled by a manual pressure relief valve, which was located at the output of a hydraulic aggregate (Fig. 4.3). The hydraulic cylinders of the extraction system worked against a steel girder structure with two abutments placed on circular steel plates with distance of 40 cm to the pile (Fig. 4.3). This design distributed forces from the static tension load test to the ground avoiding any effects on the measurements. A conical tooth clamp transmitted the pulling forces of the hydraulic extraction system to the pile. The axial displacement of the pile head was measured in real time by a displacement sensor (Burster 8712-150), which was fully decoupled from the pile motion. Rapid movements of the extraction system at the time of break-off were prevented by a throttle valve located between pressure relieve valve and extraction system. On this way, the hydraulic volume flux and thus the potential movement of the pile could be limited. Pressure in the hydraulic system was recorded with a digital pressure sensor (Parker SCP01-250-44-77-07). For converting hydraulic system pressure into force, the hydraulic cylinders were calibrated for steady force increase against a 50 kN force sensor (S9M/50kN from HBM). Accuracy of the force determination is ±1% within the 50 kN test range.

The loading procedure followed the German recommendations of EA-Pfaehle (2012), for small piles. Loading was done in five to twelve steps with equally spaced loading increments until a continuous axial displacement at the pile head was established. Load increments were calculated as being one eighth of the predicted and assumed pile capacity. Loading was kept for three minutes while axial displacement was

recorded (EA-Pfaehle, 2012), If axial displacement exceeded a minimum displacement of 3.5mm (0.1 times the diameter), the pile was classified as "failed" and the maximum force applied was recorded for later processing. In contrast to EA-Pfaehle (2012), no reloading was done after pile failure was reached. After the initial tension load test, the piles were left in the ground for a time period of either 1, 10, or 100 days until each pile was tested a second time using the same testing procedure in order to obtain for its aged capacity. Due to the minor local soil heterogeneities, a two-time testing approach of each pile was chosen rather than the one-time testing procedure recommended by Jardine, Standing, and Chow (2006). The elapsed time in between the first and the second tension load test will be referred to as "aging time", hereafter. The flow diagram shown in Fig. 4.5 illustrates and summarizes the pile installation and testing procedure.

### 4.5.4   Data management and processing

**Shear stress calculation**

The maximum pile capacity $Q_t$ at failure was calculated from Eq. 4.2.

$$Q_t = F_{max} - F_{G, pile} \tag{4.2}$$

$F_{max}$ represents the maximal force that could be applied to the pile head at the pile break off and $F_{G, pile}$ is the weight of the pile. Examples for load-displacement curves and the determination of $F_{max}$ are given in Fig. 4.6. Eq. 4.3 yields an average shear stress $\tau_{avg}$ of the mantle by means of dividing the maximum pile capacity $Q_t$ by the effective pile mantle area, being determined from the effective pile length $L_{eff}$ and the pile diameter $D$.

$$\tau_{avg} = \frac{Q_t}{\pi D \cdot L_{eff}} \tag{4.3}$$

Using Eq. 4.3 axial pile capacities of different small piles can now be directly compared. In the following, "mantle shear stress" and "pile capacity" are used interchangeable dependent on the particular content.

**Pile capacity normalization using UWA-05 approach**

In order to eliminate the influence of small soil heterogeneities and to provide international comparability of pile capacities, all piles were normalized to their predicted axial tension pile capacities using the UWA-05 approach after Lehane, Schneider, and Xu (2005) and API (2006). Therefore, a theoretical pile tension capacity was calculated at each CPT location distributed throughout the test site. These theoretical pile tension capacities were calculated from the geometry of the small piles used in this study, their center line average roughness, and the individual CPT profile (see. Tab. 2). The theoretical UWA-05 pile tension capacities at the CPT locations are $85.5\,kN < Q_{UWA} < 94.6\,kN$ for the mild steel configuration. Due to lower surface roughness of the stainless steel piles ($R_{CLA} = 2.9\,\mu m$ instead of $6.9\,\mu m$), theoretical UWA-05 pile tension capacities are also reduced to $50.4\,kN < Q_{UWA} < 58.9\,kN$. In a next step, the theoretical UWA-05 pile tension capacities at the former CPT locations were interpolated within the entire test site using a kriging algorithm (Krige, 1951; Wackernagel, 2003) for both steel configurations (see contour map in Fig. 4.1 C). As a result, a predicted UWA-05 pile tension capacity was assigned to every pile on its planned pile location using the interpolated contour map. Predicted UWA-05 shear
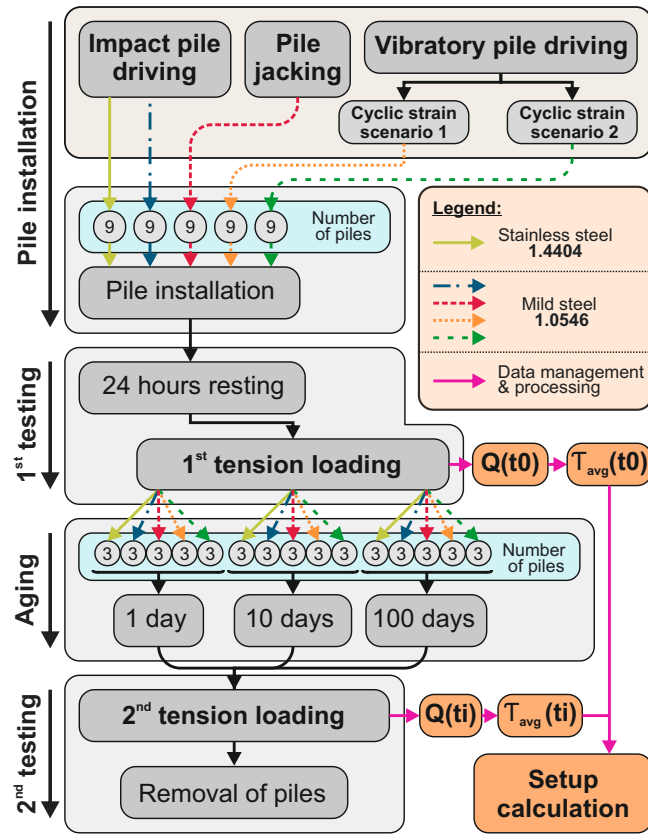
FIGURE 4.5: Schematic workflow of testing procedure. Arrows on the left are marking the different workflow phases.
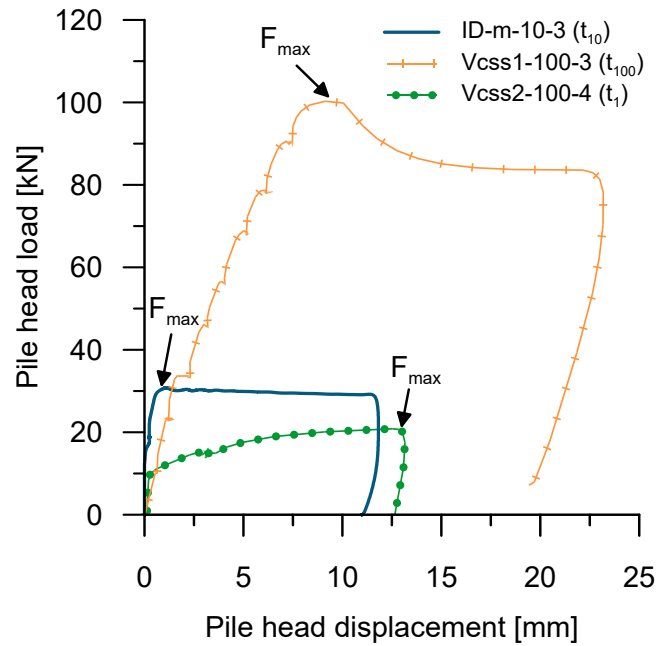


FIGURE 4.6: Three typical load - displacement curves and the determination of $F_{max}$ at pile break off. Shape of load displacement curves are not representative of the used installation method.

TABLE 4.2: Values used for UWA-05 calculation.

| Parameter | Values | Units | Source and explanations |
|---|---|---|---|
| $\rho_s$ | 2675 | kg m$^{-3}$ | density of quartz |
| $\rho_d$ | 1610 | kg m$^{-3}$ | drill core information and cylinder testing (Geo-Eng, 2014; Quinteros et al., 2018) |
| $\delta_{cv}$ | 28.81 | degree | $D_{50}$ based on ICP-05 guidelines ($D_{50} \approx 0.2$ mm) |
| $e_0$ | 0.56 | - | out of downhole logging (LOG1 & LOG2 at Fig.4.1) (Geo-Eng, 2015) |
| $R_{CLA}$ | 2.9 and 6.9 | μm | mean of measurements done with the digital microscope - VHX 6000 |
| $D$ | 0.035 | m | factory specification |
| $L$ | 12.10 | m | striven pile depth |
| $V$ | 0.35 | m | mean casing depth (zeros values up to this depth) |

$\rho_s$ - grain density; $\rho_d$ - bulk density; $\delta_{cv}$ - constant volume interface friction shear angle; $e_0$ - void ratio; $R_{CLA}$ - center line average roughness; $D$ - outer pile diameter

stresses $\tau_{avg,UWA}$ were calculated using Eq. 4.3 in combination with the predicted pile capacities extracted from the contour map (Fig. 4.1 C) and the effective pile length of the pile considered.

**Setup calculation**

The log-linear setup prediction approach after Skov and Denver (1988) was used in order to describe and classify the temporal change of pile tension capacities (Eq. 4.4).

$$\frac{\tau_{avg}(t_i)}{\tau_{avg}(t_0)} = 1 + A \log\left(\frac{t_i}{t_0}\right) \tag{4.4}$$

Where $\tau_{avg}(t_i)$ is the mantle shear stress averaged over the effective pile length at the time $t_i$ and $i$ represents the time in days after EoD. $\tau_{avg}(t_0)$ is the averaged shear stress of a pile at the time $t_0$ being measured 24h after EoD. In this study, the setup factor $A$ and the setup ratio $R_{set}$ after Eq. 4.5 were used to quantify the increase in pile capacity with time.

$$R_{set}(t_i) = \frac{\tau_{avg}(t_i)}{\tau_{avg}(t_0)} \tag{4.5}$$

**Curve fitting**

In order to make statements about the capacity and aging characteristics of piles that are generally applicable, curve fittings have been applied on the data. In these cases, fitting was done by the usage of the MATLAB curve fitting tool. Simplicity of the resulting function was prioritized if no significant increase of the coefficient of determination ($R^2$) might result by a formula of a higher degree. Fits were freely calculated by MATLAB using the LAR (least absolute residual) mode. Curve fitting parameters have not been given dimensions to ensure clarity. The fitting functions therefore only retain their validity in the dimensional frame of the axes used.

## 4.6  Results

### 4.6.1  Initial pile capacities

The installation methods influenced the initial capacities of the small piles tested in this study. Jacked piles failed at the highest initial average shear stress, all the impact driven, and vibratory driven piles failed at similar and lower initial averaged shear stresses (Fig 4.7A, Tab. 4.3). By normalizing the average shear stresses of each pile to their corresponding UWA-05 shear stress, the scatter in data could be slightly reduced in three out of the four methods and for both stainless steel and mild steel materials used for impact driving. This is shown by a reduction in the coefficient of variation in Tab.4.3, being calculated by dividing the arithmetic mean $\bar{x}$, by its related value for the standard deviation $SD$, or its range. Most of the initial shear stresses were overestimated by the UWA-05 prediction resulting in normalized average shear stresses smaller than 1 (Fig. 4.7B). In contrast, the jacked piles, exceeded the expected average shear stresses from the UWA-05 prediction (Fig. 4.7B). Impact driven piles for both pile materials were able to withstand shear stresses in between 30% and 49% of the UWA-05 prediction. Vibrated piles covered a wider range of capacities with shear stresses between 21% and 78% than those predicted by UWA-05 (Fig. 4.7B). The normalized average shear stress decreased exponentially with the number of shear cycles per m$^2$ effective pile mantle area (simply "number of shear cycles" hereafter) (Fig. 4.7C). Because of the exponential nature of this relationship, a power function with the coefficients a, b, and c was fitted to the experimental data (Eq. 4.6 and Fig. 4.7C).

$$\frac{\tau_{avg,t0}}{\tau_{avg,UWA}} = a \cdot N_{bA}^{\;b} + c \qquad a = 3.71;\; b = 0.62;\; c = 0.37 \qquad (4.6)$$

The normalized average shear stresses decreased with increasing number of shear cycles. Differences between the initial pile capacities seemed to be negligible for shear cycles roughly above a visual picked $N_{bA} = 300/m^2$. A lower bound equal to 40% of the UWA-05 prediction is approached for significant higher shear cycles than $300/m^2$. The initial pile capacity increased strongly towards lower values of $N_{bA}$.
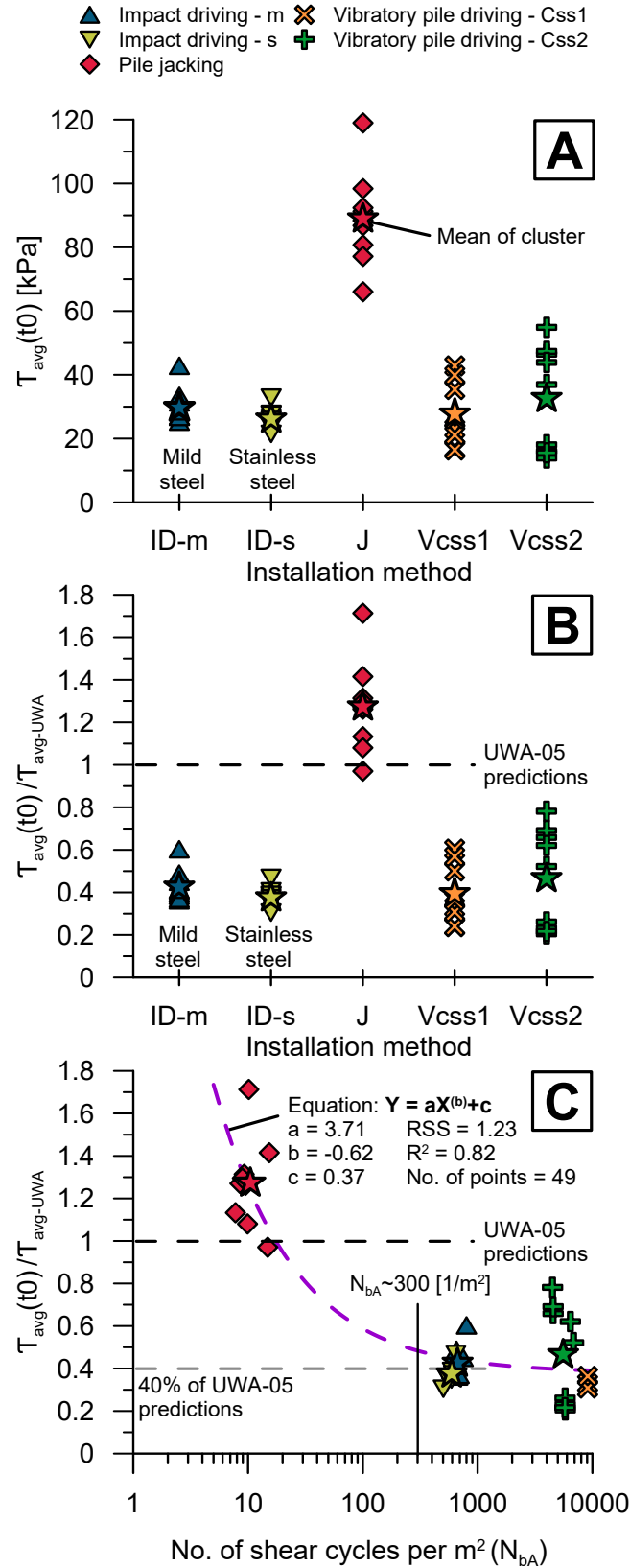
FIGURE 4.7: **A:** Initial averaged shear stresses for each pile. **B:** UWA-05 normalized initial averaged shear stresses. **C:** UWA-05 normalized shear stresses against number of shear cycles per effective pile mantel area.

TABLE 4.3: Statistical parameters for the initial averaged shear stresses with respect to applied installation method. Stainless steel and mild steel piles are considered separately although they reflect only one installation method.

| installation method | n | $_{avg}t0\ kPa$ | | | $_{avg}t0\ /\ _{avg}UWA$ | | |
|---|---|---|---|---|---|---|---|
| | | $\bar{x}$ | SD | Range | $\bar{x}$ | SD | Range |
| Impact driving - m | 9 | 29.2 | 5.6 19%* | 18.1 62%* | 0.43 | 0.08 19%* | 0.25 58%* |
| Impact driving - s | 9 | 26.1 | 3.2 12%* | 11.3 43%* | 0.38 | 0.05 13%* | 0.17 45%* |
| Jacking | 9 | 88.9 | 14.8 17%* | 52.9 60%* | 1.26 | 0.17 13%* | 0.61 48%* |
| Vibratory installation - Css1 | 8 | 27.7 | 10.3 37%* | 26.4 95%* | 0.4 | 0.14 35%* | 0.37 93%* |
| Vibratory installation - Css2 | 9 | 32.6 | 16.5 51%* | 41.0 126%* | 0.45 | 0.21 47%* | 0.49 109%* |

*Coefficient of variation – calculated by dividing the arithmetic mean $\bar{x}$ value by its related value for the standard deviation $SD$ or its range respectively, to allow comparison of this statistic characteristics beyond dimensional limits. n - distribution size; $\bar{x}$ - arithmetic mean; $SD$ - standard deviation; Range = maximum value – minimum value

### 4.6.2　Temporal development of pile capacities

The setup of pile capacities was visualized by means of average shear stresses normalized by the UWA-05 approach (Fig. 4.8A), by the setup factor (Eq. 4.4), and by the setup ratio (Eq. 4.5) (Fig. 4.8B). Piles did not exhibit significant increase in pile capacity after an aging time of one day. After an aging time of ten days, the jacked piles exhibited a capacity increase ($A$　0.5) reaching around 2.2 times the UWA-05 expectation. Setup of all other piles can be considered as negligible instead. For the aging period of 10 to 100 days, the average shear stresses of jacked piles continued to increase, reaching three times the UWA-05 expectation corresponding to an $R_{set}$ 100　2.7. Mild steel piles installed by impact driving and piles installed by vibratory pile driving reached average shear stresses, being around one to two times larger than those expected by the UWA-05 prediction (Fig. 4.8A). When considering setup ratios (Fig. 4.8B), four out of six piles installed by vibratory pile driving exhibited significantly higher setup than piles installed by impact driving or jacking (i.e. $R_{set}$ 100　4.8, $A$　2), whereas one out of three piles for each cyclic strain scenario showed a significantly lower setup (i.e. 2.5　$R_{set}$ 100　3.1, $A$　1). These moderate setup ratios for 100 days of aging were more similar to those generated by jacking and impact driving of piles constructed from mild steel. The stainless steel piles had constantly low capacities between 38% and 44% of the UWA-05 prediction after the 10 to 100 days aging period (Fig. 4.8A). Also, these stainless steel piles had again the lowest relative setup (i.e. 1.1　$R_{set}$ 100　1.3, $A$　0.1). The stainless steel piles failed at around one-third of the total average shear stresses of the mild steel piles after 100 days of aging and had less than one-tenth of their relative increases.

The setup relationships (i.e. both average shear stress normalized by the UWA-05 prediction and setup ratio) were extended by the number of shear cycles as a third dimension (Figs. 4.9A & B). For both cubes, a 3D plane was fitted for all mild steel

experiments using a polynomial function. The formulas for these fits are given in Eqs. 4.7 and 4.8, and depend on the number of shear cycles $N_{bA}$ in $cycles/m^2$ and time after EoD $ti$ in days (d).
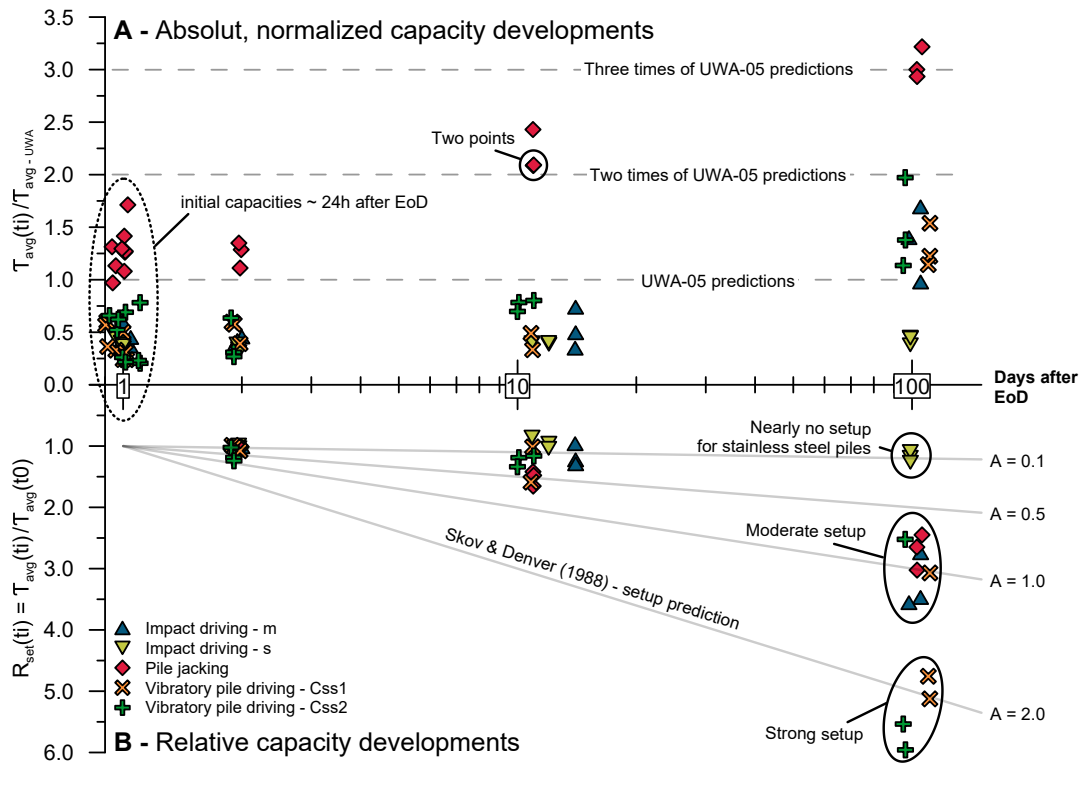


FIGURE 4.8: **A:** UWA-05 normalized initial and aged pile averaged shear stresses over time. **B:** Setup ratios over time after EoD. A - Setup factors after Skov and Denver (1988)

$$\frac{\tau_{avg}\ (ti, N_{bA})}{\tau_{avg\ UWA}} = 2.2 - 1.2\ log_{10}\ N_{bA} + 0.6\ log_{10}\ ti + 0.2\ (log_{10}\ N_{bA})^2$$
$$+ 0.2\ log_{10}\ N_{bA}\ log_{10}\ ti - 0.3\ (log_{10}\ ti)^2 \quad (4.7)$$

$$R_{set}\ (ti, N_{bA}) = 1 + 0.003\ log_{10}\ N_{bA} + 0.7\ log_{10}\ ti - 0.84\ log_{10}\ N_{bA}$$
$$log_{10}\ ti - 0.1\ (log_{10}\ ti)^2 - 0.1\ (log_{10}\ N_{bA})^2\ log_{10}\ ti \quad (4.8)$$
$$+ 0.3\ (log_{10}\ N_{bA})\ (log_{10}\ ti)^2$$

The two functions represent the experimental data reasonably well ($R^2 = 0.89$ and $R^2 = 0.92$ for Eqs. 4.7 and 4.8, respectively). Following the 3D planes, the normalized pile capacity is rising with decreasing number of shear cycles and with increasing aging time (Fig. 4.9A). The setup ratio increases with increasing number of shear cycles and with time after EoD (Fig. 4.9B). The trends displayed in both cubes indicate a nonlinear relationship between pile capacity, number of shear cycles, and elapsed days after EoD.
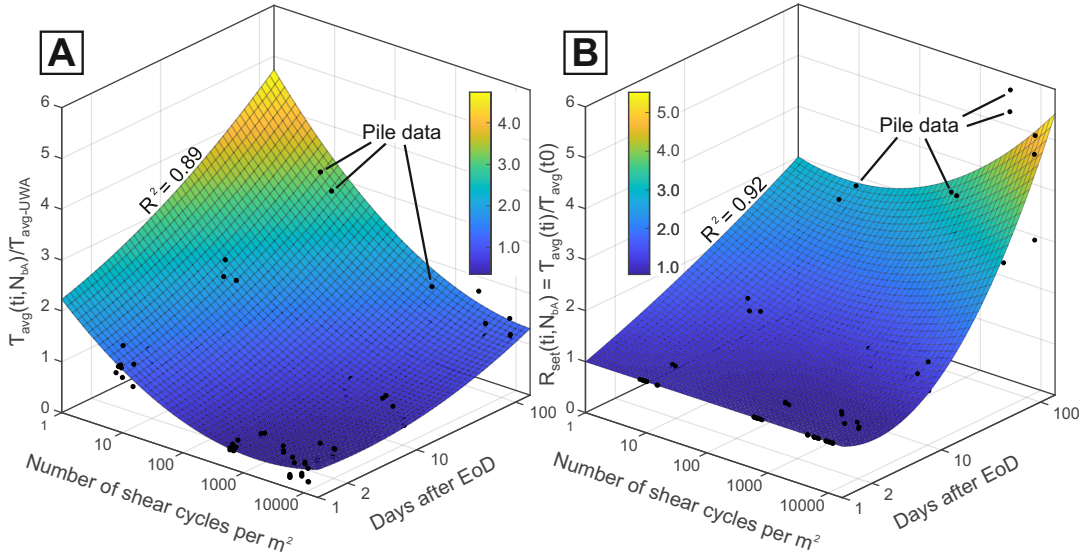
FIGURE 4.9: **A:** 3D pile capacity plane, describing pile capacity evolution in dependence to elapsed time after EoD and to number of shear cycles during driving. **B:** 3D pile setup ratio plane, describing evolution of setup ratios in the same dependency. Previous color coding of pile data was changed to provide better clarity. Initial pile capacities for $ti$ 1 were projected to $ti$ 1.01. 3D fitting was done using the MATLAB curve fitting tool. Fits were freely calculated using the LAR (least absolute residual) mode by minimizing $R^2$; Color of contour maps accompany values of vertical axes.

### 4.6.3 Field observations

After extracting the mild steel piles from the ground through hydraulic traction, it was observed that the pile surfaces of the uppermost two to three steel segments (reaching 2-3 mbgl) have been corroded. After one day of aging time, the pile surfaces had changed in color from glossy black-metallic to brown. After 10 and 100 days of aging, the pile surfaces of mild steel were extensively coated by brown-greyish agglomerates/crusts. Fig. 4.10A provides an example of a mild steel pile aged for 100 days. Exemplary sand crusts adhering the uppermost two to three pile segments are presented in Fig. 4.10B. Roughness measurements were performed on crust patches that were essentially unaffected by the extraction process and yielded a strong increase in mean centerline surface roughness from $R_{CLA}$ 6.9 µm before installation to 30 µm $RCLA$ 200 µm after 100 days of aging. No obvious change in crust thickness or shape could be observed when comparing pile segments used for the four different pile installation methods. Any signs of corrosion products rapidly decreased below the second up to the third mild steel segment. Glossy white-metallic steel dominated the pile surface from the fourth steel segment and below ( 4 mbgl). The stainless steel pile segments did not show any signs of crust formation or change in surface roughness.
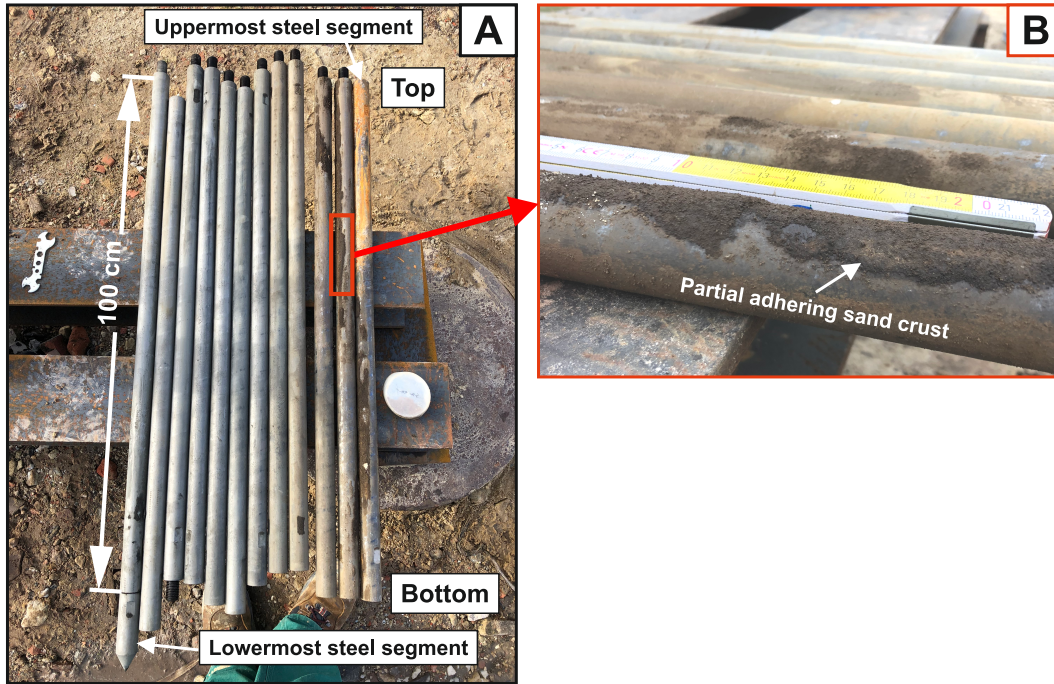
FIGURE 4.10: **A:** Photography of corroded mild steel segments, installed by jacking and left into the ground for 100 days. **B:** More detailed photography of partial adhering sand crusts from the same pile. Unit of the scale is in cm.

## 4.7 Discussion

### 4.7.1 Factors controlling initial pile capacities

Our 44 initial pile capacity measurements showed that the initial pile capacity highly depends on the method used for pile installation. Furthermore, the results presented herein confirm the approach of Anusic et al. (2019a) to code the pile installation method by means of its number of shear cycles during installation. By dividing the number of shear cycles by mantle area, the simple parameter $N_{bA}$ (Eq. 4.1), can be obtained to distinguish different pile installation methods and their resulting discrepancies in initial pile capacity. An increased number of shear cycles significantly lowers the mobilized averaged shear stresses of a pile, i.e. its axial capacity (Fig. 4.7C). This is in good accordance with observations of Anusic et al. (2019a) and Lim and Lehane (2014), who linked installation methods that cause low number of cycles (i.e. like pile jacking) to more capable piles. On the other hand, a lower initial capacity was observed by these authors, if the number of shear cycles was increased. However, with the results of this study we are able to complement their findings by incorporating the method of vibratory pile driving.

The proposed log linear relationship of Anusic et al. (2019a) does not describe the data of our study sufficiently. The presented data of this study have a more asymptotic relation between initial pile capacity and number of shear cycles and reach a constant lower capacity bound when $N_{bA}$ values of significantly more than $300 \, 1/m^2$ have been reached (Fig. 4.7). This lower initial capacity bound for moderate number of shear cycles has never been observed before. The similar initial capacities of piles installed by impact driving and vibratory pile driving observed in this study are in contrast with installations of large-scale piles, in which vibratory pile driving

commonly caused significantly lower axial capacities compared with impact driving (see e.g. DFI, 2014; Mosher, 1990). Reduced size centrifuge experiments conducted by El Haffar, Blanc, and Thorel (2017) observed higher capacities for cyclical than for monotonical jacked piles. Both studies stand in a clear discrepancy to our findings and might indicate that also the size of the pile and/or the equipment used for pile driving influences the initial pile capacity to some extent. Further research tackling this connection would be needed to provide a comprehensive answer to this question.

The axial pile capacity degradation with the number of shear cycles recognized for our pile size is in accordance with the theory of friction fatigue. Heerema (1978) as well as Jardine and Chow (1996) described this effect and e.g., Gavin and O'Kelly (2007), White and Lehane (2004), and Yang et al. (2014) could measure the impact of friction fatigue by analyzing stresses acting on model piles and their vicinity. Friction fatigue as a soil mechanism explains the reduction of the acting radial stress with a rising number of shear cycles in between the pile mantle and a distinct soil element: Each shear cycle or blow forces a small and densified soil element in the vicinity of the pile into a dilative response. As a consequence of multiple dilative responses, the granular structure becomes successively more disturbed. Previous force chains are interrupted and the transmission of lateral stresses to the pile mantle is hampered. Thus, the axial capacity of the pile is progressively diminished with a rising number of shear cycles (Lim and Lehane, 2015). White and Lehane (2004) observed the existence of a lower stress bound surrounding their model piles after a high number of cyclic movements, which is very similar to our lower capacity bound in Fig. 4.7C. Their interpretation involved the separation of radial stress in a static and a dilative component. The static component is reduced by each further shear cycle, whereas the dilative stress component can maintain its developed stress peaks even over a very high number of cycles. This dilative component occurs only when the pile induces a relative soil displacement (i.e. during pile loading). The lower capacity bound observed in Fig. 4.7C might be caused by the residual dilative stress component acting on the pile after all the previous static stress was reduced by cyclic pile movements.

The initial capacities of piles installed by vibratory pile driving observed in this study exhibited much higher variability than the capacities of piles installed by impact driving, which may have been caused by wobbling of the piles due to vibration. The magnitude of pile wobbling was potentially a function of soil properties (e.g., soil stiffness, soil strength, relative density). The pile wobbling may have been prevented, if a force-controlled installation method was used.

If maximum initial pile capacity is prioritized over drivability, a minimum of induced installation shear cycles must be aimed for. As a consequence, the installation methods of jacking and impact driving, which apply a low number of blows, are the preferred methods. If logistics, handling, noise, material fatigue, and installation speed are the priority, vibratory pile driving is the favored method. The lower initial capacity limit of 40% of the UWA-05 prediction (Fig. 4.7C) might be a value to be used for the preliminary design of initial pile capacity. These recommendations are only directly applicable to small piles in very dense sands and will become less reliable for deviating boundary conditions. Further studies are needed to extend our gained knowledge of initial pile capacity to more diverse soils and pile geometries.

### 4.7.2 Temporal evolution of pile capacities

Our data demonstrate that in addition to the initial pile capacity, the pile setup is highly depending on the pile installation method too (Fig. 4.8). This observation is in good accordance with experiments performed by Lim and Lehane (2014) as well as by Anusic et al. (2019a). The coding via the number of shear cycles suggested by Anusic et al. (2019a) seems also useful to distinguish pile setup characteristics (Fig. 4.9) in addition to initial capacity. However, we observed that the elapsed time after EoD remains an important parameter that influences setup. The effect of elapsed time after EoD was not considered by Anusic et al. (2019a) probably due a lack of pile data. The multi parameter approach, as developed in this study (Fig. 4.9), indicates that setup strongly depends on the number of shear cycles and the elapsed time after EoD. If only one of these factors was considered by itself, an accurate capacity prediction would be erroneous. This can be seen in Fig. 8B, where our data clearly not follow the log-linearly setup prediction approach of Skov and Denver (1988). All setup data from Anusic et al. (2019a) and our study that considered an aging time of more than 40 days, confirm that a pile subjected to a higher number of shear cycles exhibits a more pronounced setup (Fig. 4.11). This will also be valid, if we resort to a two-dimensional representation due to a lack of available data points for a more detailed 3D comparison. The theory of stress re-equilibration postulated by Lim and Lehane (2014) and supplemented by Zhang and Wang (2015) may be suitable to explain this general effect of a higher setup induced by more shear cycles. Both publications redefined setup to be a process of soil recovery rather than a process of capacity gain as it was previously described by Chow et al. (1998). Following Lim and Lehane (2014), the natural stress state is disturbed during pile installation. These disturbances in turn can be quantified by friction fatigue, which depends on the number of shear cycles. Subsequently, the stress disturbances re-equilibrate with time and lead to increasing normal stresses on the pile mantle. This results in a net increase in pile capacity. Our data show that more disturbance (caused by more shear cycles) generates a lower initial capacity but a more pronounced setup over time (Fig. 4.9B). Lim and Lehane (2014), thus combined the conceptual models of cycle-dependent friction fatigue, acting during installation, with soil and stress recovery over time (i.e. setup). The setup data of this study deviate from this theory of temporal stress re-equilibration in two points:

1. Following the stress re-equilibrium concept, mild and stainless steel piles installed by impact driving would both be expected to experience a similar setup. However, the setup for these two different steel types differed by one order of magnitude (Fig. 4.8A and B).

2. Only minimal setup is expected for jacked piles following the stress re-equilibration concept, as jacking represents the least disturbing installation method (i.e. lowest number of shear cycles). Our jacked mild steel piles however experienced a remarkably strong setup compared with the literature (Fig. 4.11).

An attempt is made to explain these two differences in the following chapter.

The influence of the in this study used two-time testing instead of one-time testing procedure recommended by Jardine, Standing, and Chow, 2006 can be considered as negligible. Otherwise, our 1-day aged capacities would be consistently smaller than the initial capacities measured 24 hours earlier. Since this is not the case (Fig. 4.8), the setup within this one day even for the stainless steel piles is larger than the damage caused by the two-time testing. We can recommend this procedure for test

sites where minor soil inhomogeneities might lead to a higher methodological error otherwise.
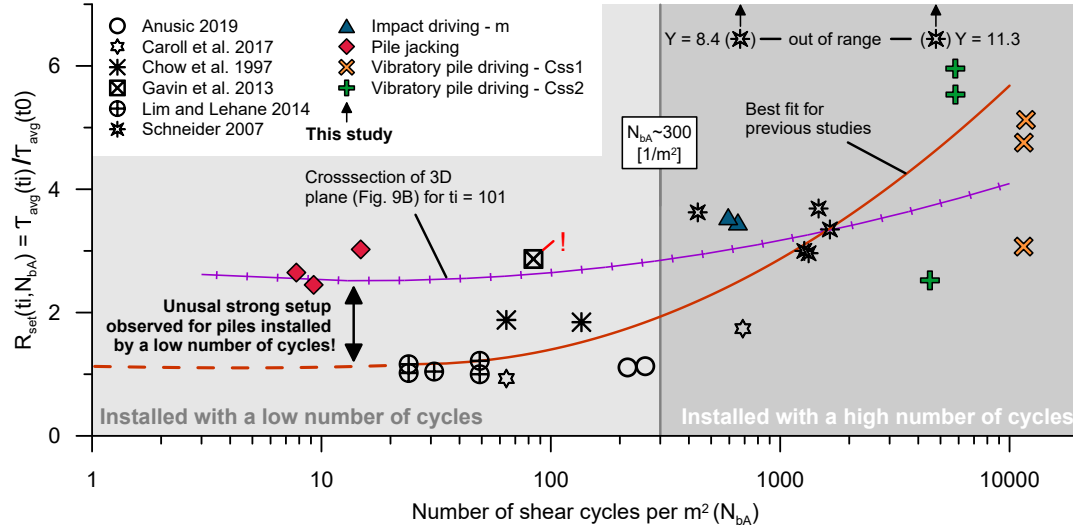


FIGURE 4.11: Setup ratios over the number of shear cycles per $m^2$ of active pile mantel area. Two points out of Schneider (2007) were down shifted parallel to Y-axes for better clarity.

### 4.7.3 Corrosion effects

The deviation of the stainless steel piles from the setup characteristics of the impact driven mild steel piles can - in absence of other differences except for the slightly lower initial roughness of the stainless steel piles – only be explained by their differing corrosion characteristics. Stainless steel piles had only 10% of the setup of their mild steel equivalents, indicating that corrosion controlled about 90% of the setup in this case (Fig. 4.8). This is in good accordance with findings from Carroll et al. (2017), Carroll et al. (2019), and Lehane et al. (2012), and White and Zhao (2006), who also identified corrosion as the major factor for their setups. Other publications, such as Gavin et al. (2015) instead, explicitly excluded corrosion as major factor since setup has also been observed in studies on wooden and concrete piles. The remaining 10% setup of our stainless steel piles proves that corrosion in turn is also not sufficient to explain this setup behavior alone. Only a combination of both factors – corrosion and stress re-equilibration – explain all observations. Since a strong dependency between the installation method and the setup could nevertheless be demonstrated for all the mild steel piles used (Fig. 4.9B), there has to be also an interaction/superimposing of corrosion – which should act equally for all mild steel piles – and the re-equilibration of the stress field. Otherwise, the differences in capacity between the individual installation methods for the same pile material could similarly not be explained. The unexpected setup of jacked piles is analyzed by plotting the setup ratios of piles installed with a low number of cycles against the cone resistances of their respective test sites (Fig. 4.12). Piles installed in denser soils by low number of shear cycles tended to exhibit higher setup ratios. All piles plotted in Fig. 4.12 were made from mild steel with directly or indirectly reported formation

of iron oxide incrustations. Thus, we conclude that additional friction due to the iron oxide crusts is transferred more efficiently into a larger soil volume around the pile in denser sands. This explanation is further supported by a pile from Gavin, Igoe, and Kirwan (2013) shown in Fig. 4.11 and Fig. 4.12 with an exclamation point. This pile was installed in a test location with high cone resistance resulting in a setup ratio comparable with this study.

Since there is evidence that corrosion effects have a disproportionate influence on capacity when dealing with relatively small piles (Carroll et al., 2019), these findings cannot yet be applied to larger diameters. Further experiments with different pile diameters are needed.
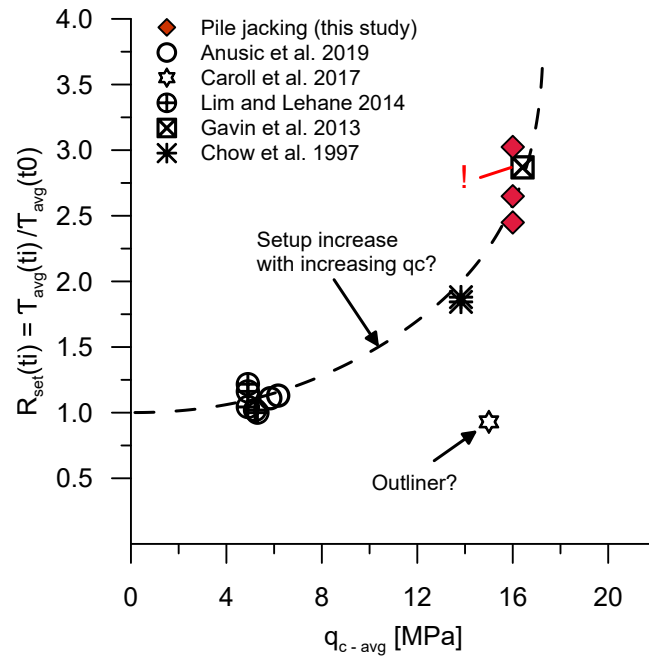


FIGURE 4.12: Isolated setup ratios for piles installed with low number of shear cycles in dependency to the averaged cone resistance encountered in the related test sites. Own pile data is combined with literature data with a maximum number of shear cycles of 300 m $^2$.

## 4.8   Conclusions

This study reports pile capacity measurements on 44 small piles performed in a dense natural sand deposit. Our approach of using mild and stainless steel piles as well as four different cyclic strain scenarios for pile installations provided a comprehensive insight into the initial pile capacity and setup characteristics. The following conclusions were made.

- The study supports the approach of Anusic et al. (2019a) to use the number of shear cycles as a suitable parameter to account for the soil disturbance during installation.  This value influences both, the initial capacity of a pile and its setup.

- A higher number of shear cycles resulted in a lower initial pile capacity.  A lower bound of capacity was observed for piles installed by significantly more than    $300 \, m^2$ shear cycles.

- The evolution of pile capacity can be described using a 3D plane as a function of the number of shear cycles induced during pile installation and the elapsed time after EoD.

- The relationship published by Skov and Denver (1988) for setup prediction seems to be oversimplified since the influence of pile installation is not taken into account.

- The setup of small piles made from mild steel that were installed in dense sand seems to be dominated by corrosion effects.

- Setup was explained by combination of at least two factors: Stress re-equilibration over time controlled by friction fatigue and the corrosion of the pile-soil system.

- Corrosion has to interact somehow with the installation dependent stress re-equilibration over time.

- Even mild steel piles subjected to a low number of shear cycles (   $300 \, m^2$) exhibited substantial setups due to corrosion (especially in dense sands) even though the stress re-equilibration theory after Lim and Lehane (2014) would have predicted otherwise.

More reliable pile capacity prediction can only be developed if the axial setup will be understood as a multidimensional and multi-factorial process. More studies using different pile diameters with inert and corrosive materials at test sites with wider ranges of soil densities are required.

## 4.9   Acknowledgments

**Chapter 5**

# Installation and time effects on large-diameter pile capacity

## 5.1 Authors

1. **Alexander V. Busch**[1]

2. **Majid Goodarzi**[1,2]

3. **Benjamin Ossig**[3]

4. **Akash Verma**[3]

5. **Pooyan Ghasemi**[2]

6. **Tobias Mörz**[1]

* These authors contributed equally to this work.

[1]MARUM – Center for Marine Environmental Sciences, University of Bremen, Bremen, Germany

[2]COWI A/S, Hamburg Branch Office, Hamburg, Germany

[3]Geo-Engineering GmbH, Bremen, Germany

Corresponding author: mgoodarzi@marum.de

## 5.2    Abstract

Large diameter open-ended piles are the most frequently used foundations for off-shore wind turbines. The well-established method of impact driving has some deficits in terms of driving induced fatigue, installation speed and noise emission. However, attempts to circumvent this problem by alternative installation methods such as vibratory driving often not welcomed due to lack of experiences with this installation method. A few large-diameter-size studies exist who could show how lateral and axial capacities vary, or their temporal behavior (setup) is influenced with an alternative installation method. This hampers adequate design predictions which nevertheless are mandatory for a project. In this study, results of dynamic axial pile capacity tests of three pairs of impact and vibratory driven piles with a diameter of 4.3 m are provided, reflecting their capacities after more than three years of aging. Regarding the impact-driven piles with several restrike tests, the temporal capacity developments showed a remarkably strong increased which was not following a straight log-linearly relationship generally considered for setup rate. In terms of installation effect, the vibratory pile installation seems to affect the long-term axial capacity more dramatic in comparison to its negative effect on lateral capacity previously published by Achmus et al. (2020). The presented data provides a fundamental contribution to the understanding of vibratory and impact driven piles behaviors in dense sand with potential impacts to improve pile design practices for the similar sub-soil condition.

## 5.3    Introduction

Making use of a resource available in a nearly endless amount is the promise of using wind turbines generating electrical power out of atmospheric movements. Efficiently increases were achieved by relocating these turbines in offshore areas caused by higher wind intensity and continuously as well as by the possibility for bigger wind turbines (Rohrig et al., 2013). This increase in efficiency was accompanied by increase in the costs for installation and production related challenges to such an adverse and rough environment. Whereas approx. 20% of the total costs of a wind turbine evolves out of the foundation for shallower water depths (10-20m) this portion increases up to 36% for water depths of around 40-50 m (Swart et al., 2009). Thus, an optimization of the turbine foundation and their installation provides the highest cost saving potential. Most frequently these turbines are founded offshore on open-ended mono-piles conventionally installed by hydraulic hammer pulses known as impact driving. Nevertheless, two main issues arise using this traditional way of pile installation. Firstly, a high sound pressure emerged during each hammer pulse dramatically disturbs sea mammals due to their acoustic sensitivity. As a result, pile driving is often limited to just a small time frame in the year or the use of expensive, sound mitigation techniques (see e.g. Nehls et al., 2016; Verfuss, Sinclair, and Sparling, 2019). A second issue arises out of the induces high stress gradient in the pile material during each hammer pulse. Special care must be given during the piles design to these induced stresses to avoid significant material failure. The thickness of the pile can be controlled by this factor (see e.g. Buitrago and Wong, 2003; Chung, Wallerand, and Hélias-Brault, 2013; Ozsu et al., 2013). With an increase in foundation size and therefore the required pile driving energy, it becomes more challenging to use this installation method. Finally preventing an endless scaling of the foundation for even bigger turbines. An alternative installation method called

vibratory pile driving might provide a solution, reducing sound pressure and pile fatigue to a minimum (Jonker, 1987; Elmer et al., 2007). In addition, faster installation, reduced pile-run problems and the possibility of removing and re-installing the pile in case of high inclination are further advantages of this installation method. However, first studies considering the capacity of identical piles driven by either impact driving or pile vibration recognized a significant reduction in axial capacity of -20% up to -42% for vibrated piles (Mosher, 1990; Fischer et al., 2013; DFI, 2014). It is suggested by Mosher (1990), DFI (2014), and Remspecher (2014), that this reduction might evoke out of a reduced pile toe capacity. Nevertheless, these low amounts of data, varying constrains and possible sources of error prevented the development of a vibro – pile capacity reduction factors in the past. Even more complexity is given by the fact that the capacity of these piles tends to increase over time. An effect described as setup effect and observed by many studies (e.g. Chow, 1996; Tavenas and Audy, 1971; Axelsson, 2000; Kolk, Baaijens, and Senders, 2005). Not seldom this capacity can be doubled in the first 1000 days after end of driving (EoD), again creating major importance in kind of an economic perspective. Although this effect is often described, not enough data exists equally trying to understand how setup is controlled by varying installation methods, especially when real offshore sizes are in demand. First studies considering reduced size piles by Lim and Lehane (2014) assumed, that previous differences in initial axial capacity initiated by different installation methods would fade away after sufficient time. A proof of this assumption is still missing regarding large diameter piles. To provide firstly some real size pile data combining the effect of time and installation on the capacity of large-diameter open-ended piles, this study presents the results of two joint industry projects. The tests included six 4.3 m diameter piles installed in dense sand in an onshore test site in Cuxhaven (Germany). Three of which were installed using a vibrator and three using an impact hammer. Aside from the lateral load tests (see Achmus et al., 2020), axial pile capacities were measured multiple times using dynamic pile load tests (DLT). These load tests took place at the EoD and around 2 weeks after EoD for the impact driven piles. After a resting phase of around 1000 days after EoD all piles – now also including the vibrated once – have been finally tested for their aged capacities.

Based on these tests, this study tries to address the following questions:

- Are differences in axial pile capacity induced by different installation methods recoverable after sufficient aging time?

- What would be the setup rate for large diameter piles in dense sand?

## 5.4   Case study of pile test in Cuxhaven, Germany

Lack of well documented experiences and consequently design standards for large diameter monopiles with vibratory pile driving was a major obstacle for its industrial application. Therefore, in 2014, a consortium of industrial groups led by RWE and supported by the Carbon Trust planned to carry out a large-scale pile testing in an onshore test site known as the VIBRO-Project. Six open-ended steel piles with 21 m length and 4.3 m of diameter were installed with a nominal embedment depth of approx. 18.5 m below ground level (in the following referred to "mbgl") as three pairs with the impact and the vibratory pile driving method. The major objective was to pull each pair of piles together as a lateral load test and evaluate the installation effect on the lateral bearing capacity. Several additional investigations including estimation of axial capacity through DLT on the impact-driven piles were considered. The temporal order of pile installation, multiple DLTs or the lateral loading of each individual pile is given in a detailed time bar in Fig. 5.1. Pile installation related properties for the impact driven piles are given in Tab. 5.1 and for the vibrated ones in Tab. 5.2. In 2017, more than two years after the initial test program, another project (VIBRO Restrike) was conducted to evaluate the change in the axial capacity of these open-ended piles. Therefore, several re-strike DLTs were performed on all six piles to determine the long-term axial capacity of both, impact driven and vibrated open-ended piles.
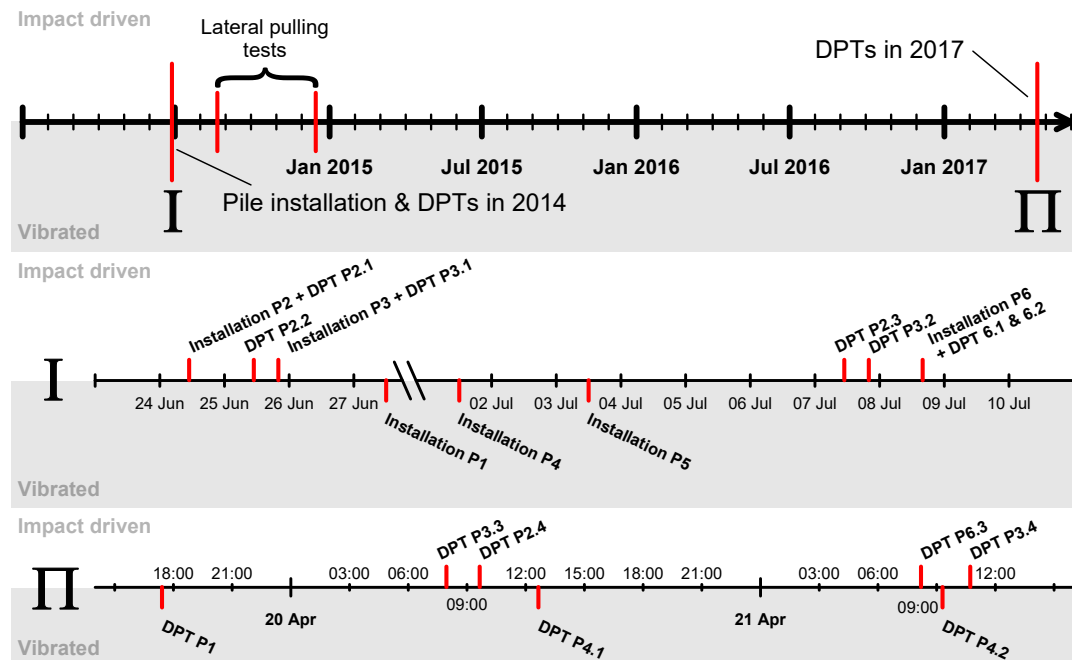


FIGURE 5.1: Time-line of pile installations, dynamic pile load tests (DLT) or lateral loading.

TABLE 5.1: Installation properties of impact driven piles.

| Pile | Date | Duration | Blows | Blow rate | Energy per blow |
|------|------|----------|-------|-----------|-----------------|
| P2 | 24 June 2014 | 29 min | 1785 | 40-50 min [1] | 238 kJ |
| P3 | 25 June 2014 | 48 min | 2944 | 70-85 min [1] | 166 kJ |
| P6 | 08 July 2014 | 32 min | 1328 | 40-50 min [1] | 542 kJ |

Energy per blow is averaged for the last 5 meter of piles installation. P3 wa installed using a high rate of blows with low energy (Hi-Lo method)

TABLE 5.2: Installation properties of vibratory driven piles.

| Pile | Date | Duration [min] | Frequency [Hz] | [Hz] | Vibrator power [bar] | [bar] | Transition depth mbsf |
|------|------|----------------|----------------|------|---------------------|-------|----------------------|
| P1 | 27 June 2014 | 16 | 12 | 22.5* | 150 - 200 | 380 | 9.5 |
| P4 | 01 July 2014 | 4 | 12 | 22.5 | 200 - 300 | 380 | 8.5 |
| P5 | 03 July 2014 | 3 | 12 | 22.5 | 200 - 300 | 380 | 9.5 |

*Vibratory driving started with a frequency of 15 Hz.

## 5.5 Side specification

The test site is located in a sand pit in the northern part of the Cuxhaven-Bremerhaven moraine ridge, approx. 7 km south of Cuxhaven – northern Germany. The ground mainly consists out of dense to very dense sands of glacio-fluvial origin deposited during the middle Saalien ice advance (Sindowski, 1963; Ehlers, 1990). These cross bedded sand deposits are interrupted by two 0.7-1 m thick till layers in depths of around 4.5 and 18 m below the ground level. The water table is commonly located underneath the uppermost till layer at a depth of 5 up to 6 m. A simplification of the lithology and some geotechnical parameters developed out of two drill cores at the test side were given in Fig. 5.2 with relative density calculated out of $q_c$ value using Baldi et al. (1986). The dense sedimentation as well as the sedimentological composition encountered in this sand pit creates an analogy comparable to the offshore north see ground situation making this place to an ideal testing side to reproduce offshore foundations in an onshore environment. Results of several laboratory and field geotechnical tests on Cuxhaven sand have already been published (Goodarzi et al., 2019; Achmus et al., 2020; Al-Sammarraie, 2020). For each pile, four CPTs were carried out in a hexagonal pattern around the pile with 2.6 m distance to the pile center. An averaged profile was generated by averaging as the representative profile for each location. CPT profiles are presented at Appendix A.1.
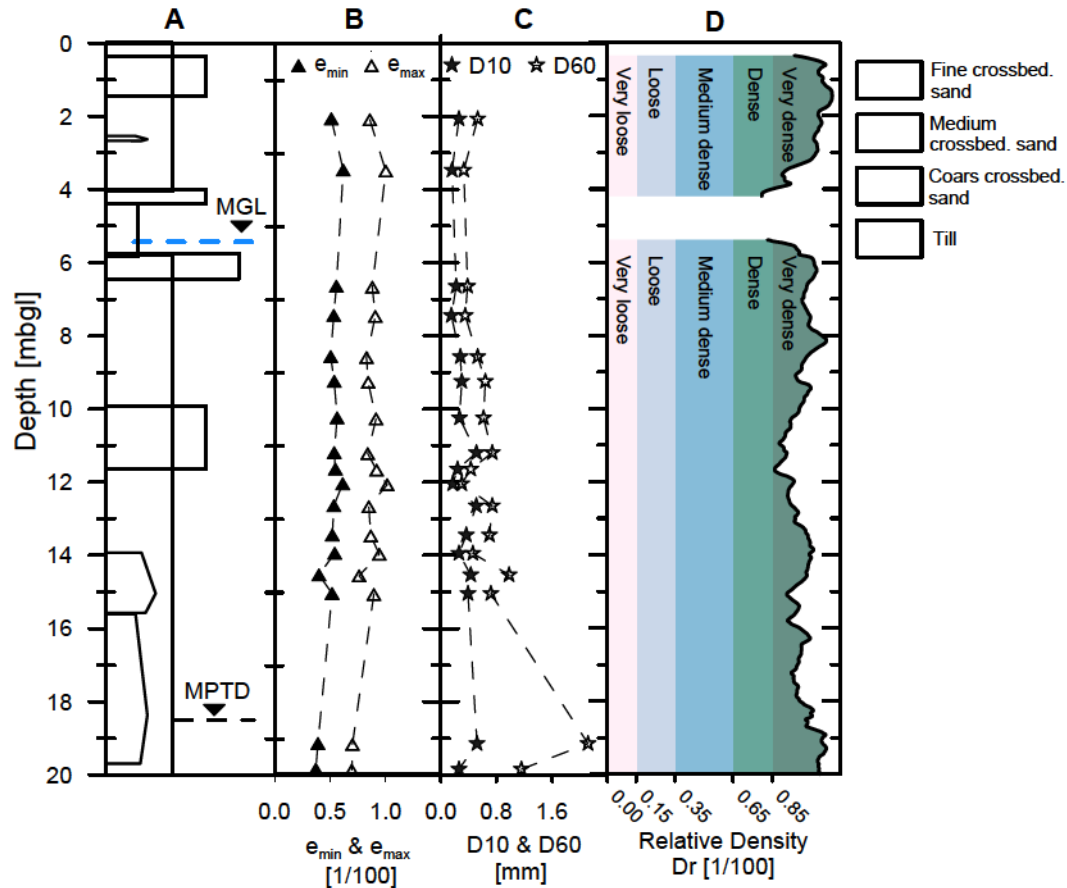
FIGURE 5.2: **A:** simplified lithology from borehole data encountered on the test side in Altenwalde presented in Geo-Eng (2014) and Geo-Eng (2015). **B:** Void ratios generated after DIN 18126 out of core samples. **C:** Grain size analyzes done after DIN 18123 out of core samples. **D:** Vertical relative densities calculated out of CPT data after Baldi et al. (1986). Colors represents soil classifications using relative densities after DIN EN ISO 14688-2, 2020. MGL - Mean groundwater level; MPTD - Mean pile toe depth

## 5.6   Methods

### 5.6.1   High strain dynamic load testing (DLT)

In the case of a large diameter pile, a static load test (SLT) is significantly costly and practically not attractive (Randolph, 2003). Alternative methods such as high strain dynamic load test (DLT), in which the pile driving hammer is used to apply a rapid dynamic load on top of the pile, is more desirable and feasible for a large pile. While the cost and effort for DLT are lower than for SLT, the output of the test is not directly the desired load-bearing capacity of the pile. During the dynamic pile test, a shock wave is generated by one blow of a hammer or a drop weight at top of the pile and travels along the pile downward. The initial shock wave is recorded by a set of acceleration and strain-gages sensors at top of the pile. The shock wave travels further downward and any interaction between the pile and soil layers, any damage in the pile structure, and also when the wave reaches the pile toe would lead to a partial reflection of the downward wave. The reflections are recorded as well

with the set of sensors at top of the pile (Salgado, 2008). The so-called CASE method was developed to estimate the static pile bearing capacity from a single hammer blow (Goble, 1980; Rausche, Goble, and Likins Jr, 1985). In this approach, the total resistance was assumed to consist of static and dynamic components, in which the dynamic resistance is linearly proportional to the velocity at the bottom of the pile. Several static and dynamic pile load tests were performed to calibrate the CASE method and a damping factor *J* was adopted to establish the relationship between dynamic soil resistance and the measured velocity. While the CASE method provides a simple solution for interpretation of dynamic pile tests, several assumptions such as rigid-plasticity for soil static behavior, lumped pile resistance, among others limit its capability (Salgado, 2008). Further improvement in the dynamic load test was achieved by adopting the concept of wave equation analysis, originally developed for pile driving analysis by Smith (1960) to perform a detailed analysis of a single blow. In this more sophisticated method, the pile is assumed as a linear elastic 1D-system and discretized (Fig. 5.3).
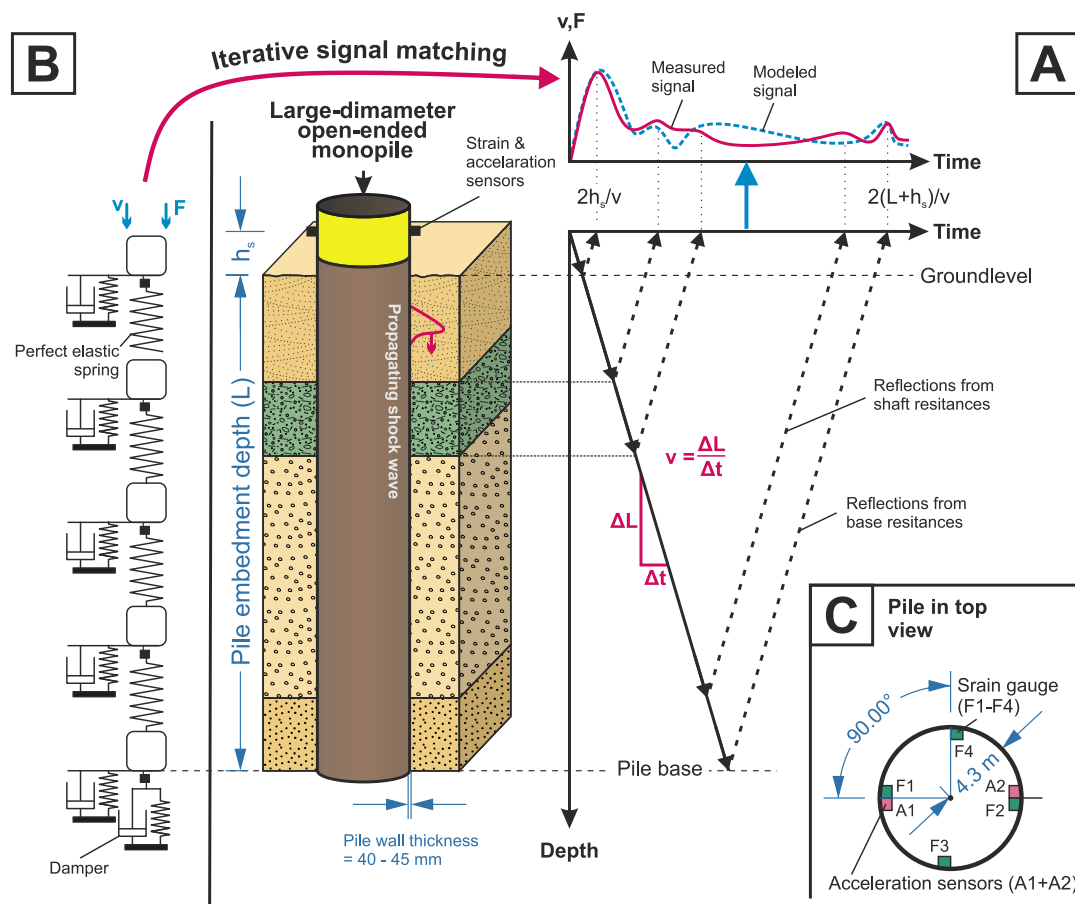


FIGURE 5.3: **A:** Simplification of pile geometries and dynamic load testing procedure; reworked after Randolph (2003). **B:** Spring - damper arrangement after Smith (1960). **C:** Cross-sectional view and sensor arrangement; $h_s$ - distance of strain and acceleration sensors above ground level, $v$ - wave speed, $t$ - elapsed time, $F$ - force

Compared to the CASE method, the static soil behavior is considered more re-
alistically with a linear elastic perfectly plastic model. The recorded shock wave is
applied at top of the model as a boundary condition and the propagation and re-
flection of the shock wave in the pile are simulated. The soil parameters for several
arbitrary pile segments along the shaft and at the toe are adjusted in an iterative
procedure until a reasonable match between the calculated and recorded force and
velocity is achieved. The work at Case Western Reserve University has led to a
package called CAPWAP (Case Pile Wave Analysis Program) which is still the most
popular commercial software for signal marching analysis (Pile Dynamics Inc., 2006;
Rausche, Moses, and Goble, 1972; Rausche, Goble, and Likins Jr, 1985). To perform
a signal matching analysis, in the simplest case, three parameters: maximum static
resistance $R_{Static}$, soil stiffness – represented as relative displacement of the pile to
soil known as quake $Q$ – and damping factor $J$ should be adjusted for each section
m along the pile. Fig. 5.4 simplifies the connection between the two proportions of
the ultimate resistance $Ru$, the maximum static resistance $R_{Static}$ and the dynamic
resistance $R_{Dynmaic}$ for one arbitrary pile segment $m$.
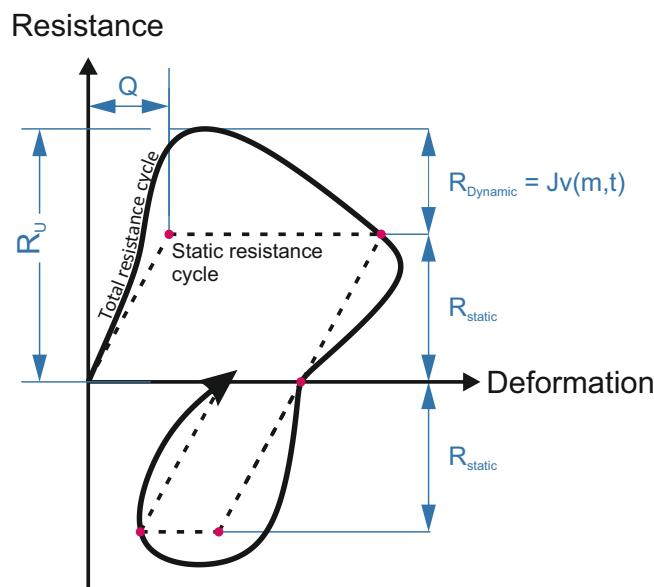


FIGURE 5.4: Visco-elasto-plastic load-deformation curve for one local
pile-soil interaction segment under dynamic loading. Modified after
Smith (1960). $Q$ - quake, $R_{Dynamic}$ - dynamic resistance, $R_{Static}$ - static
resistance, $Ru$ - total resistance, $J$ - damping, $v$ - velocity, $t$ - duration.

Although recommendations have been provided for damping and quake for each
soil type (Pile Dynamics Inc., 2006) the actual values used in different projects are
significantly scattered (Ng and Sritharan, 2013). Furthermore, the empirical nature
of the soil-pile interaction model of Smith does not allow for easy determination
of the parameters (Randolph, 2003). Although attempts had been made to further
improve the soil-pile interaction model (Lee et al., 1988), the original Smith's model
has remained the dominant idea. Some researchers argued that these parameters are
only related to soil type but also driving energy and time (McVay and Kuo, 1999).
Having force $F$ and velocity $v$ measurements at a single point versus all these un-
known parameters to adjust along the pile could lead to a non-unique result (Ng and
Sritharan, 2013). Different distributions of soil resistance along the pile shaft and at
the tip can potentially produce the same force and velocity history at top of the pile.

The accuracy of the dynamic pile test, in comparison with the static test, has been discussed in several studies (Likins and Rausche, 2004; Bradshaw and Baxter, 2006; Rausche, Nagy, and Likins, 2008; Rausche, Likins, and Hussein, 2008; Osman, Ahmed, and Ahmed, 2013; Ng and Sritharan, 2013; Moayedi, Mosallanezhad, and Nazir, 2017). Generally, it was concluded that the difference in the ultimate pile capacity obtained from dynamic and static pile tests varies between ±15%. Rausche, Nagy, and Likins (2008) showed that while ultimate capacities evaluated by different independent analysts are not that different, the ratio of shaft/toe capacity to the ultimate capacity may have a noticeable difference. This is because in signal matching with only one set of sensors on top of the pile, it is not always possible to separate the ultimate from shaft resistances close to the toe. Additional sensors along the pile could help to reduce this error (Alvarez, Zuckerman, and Lemke, 2006; Schilder et al., 2013). Due to elasticity of the pile and/or a not sufficient hammer size it sometimes appears, that the maximum possible pile toe capacity is not activated during the first hammer impact. At these cases, the ultimate pile capacity $R_u$ is composed out of the pile shaft capacity $R_s$ related to one of the first hammer impacts and a toe capacity $R_t$ out of some later impacts, representing standard procedure (Hussein, Sharp, and Knight, 2012).

### 5.6.2   Dynamic pile test in VIBRO and VIBRO-ReStrike projects

In the framework of VIBRO project in 2014, to keep the vibratory-driven piles undisturbed for lateral load test, only the three impact-driven piles were tested for axial capacity. All tests were performed as High-Strain-Dynamic-Test using the IHC-1200 hydraulic hammer. Two acceleration sensors and four strain gauges (DMS) are installed at a distance of 2 meter underneath the pile top. To offset possible eccentricities, the sensors are mounted in pairs on opposite sides of the inner. In order to avoid material failure in the pile stick up during lateral load test, the stick-up section was reinforced with concrete. Therefore, in 2017 tests, the sensors were placed further way from pile head to reduce any possible impact of this part on the recorded shock wave signal. Soil had to be sightly excavated around the pile to create more space for placing the sensors. This means the embedment depths of the piles are slightly different in 2014 and 2017 tests which should be considered when analyzing and comparing the results together. Fig. 5.3A and C gives an overview about the location of sensors in cross - and longitudinal section.

### 5.6.3   Axial capacity prediction

Axial pile capacities have been estimated using the three most common axial pile capacity prediction approaches, API-00, ICP-05 and UWA-05, firstly presented in commentary of the 22nd edition of the API-RP-2A recommendations 2006. The well-known methods of ICP-05 (Jardine et al., 2005) and UWA-05 (Lehane, Schneider, and Xu, 2005) use empirical relationships and material laws to generate pile toe and shaft capacities directly out of the in situ cone resistances $q_c$. The API-00, on the other hand, uses the vertical effective earth pressure gradient for these calculations combined with tabular values depending on the soil state for limiting shaft and toe capacity. Related formulas for each calculation are given in the primary literature as well as in the API (2006) collection. Caused by some typing errors even in the primary literature, all formulas used for these calculations were out of Schneider, Xu, and Lehane (2008). Values used for calculation are given in Tab. 5.3 and Tab. 5.4. For UWA-05 and ICP-05 predictions, the representative averaged CPT profile

TABLE 5.3: Pile embendment depts and sensor properties.

| Symbol | | Units | Explanations | P1 V | P2 ID | P3 ID | P4 V | P5 V | P6 ID |
|---|---|---|---|---|---|---|---|---|---|
| $h_s$ | L (2014) | m | sensor to toe | - | 19.00 | 19.00 | - | - | 19.00 |
| $h_s$ | L (2017) | m | sensor to toe | 16.90 | 17.10 | 17.35 | 17.40 | 17.04 | 17.11 |
| V | | m | excavation | 01.36 | 01.59 | 01.51 | 01.42 | 01.87 | 02.12 |
| L (2014) | | m | embedment | 18.08 | 18.70 | 18.53 | 18.54 | 18.53 | 19.13 |
| L (2017) | | m | embedment | 16.72 | 17.11 | 17.02 | 17.12 | 16.66 | 17.01 |

TABLE 5.4: Input values for pile capacity prediction.

| Symbol | Value | Unit | Sources and norms |
|---|---|---|---|
| $_s$ | 2675 | kg m $^3$ | tabular value |
| $_d$ | 1610 | kg m $^3$ | Geo-Eng (2015) and Quinteros et al. (2018) |
| $_{cv}$ | 28.8 | rad | Jardine et al. (2005) |
| $e_0$ | 0.56 | - | Geo-Eng (2015) |
| $R_{CLA}$ | 10 | µm | tabular value for mild steel |
| $D$ | 4.3 | m | pile factory specification |
| $w_1$ | 0.045 | m | pile factory specification |
| $w_2$ | 0.04 | m | pile factory specification |
| $c$ | 6.2 | m | pile factory specification |
| $MGL$ | 5.5 | m | out of CPT and drilling |
| $_{cv\ clay}$ | 30 | degree | Jardine et al. (2005) |
| $OCR$ | 2.7-2.9 | - | Quinteros et al. (2018) |
| $Si$ | 3.6 | - | Geo-Eng (2014) |
| $API_{max}$ | 96 | kPa | Schneider, Xu, and Lehane (2008) |
| $API_{Nq}$ | 40 | - | Schneider, Xu, and Lehane (2008) |
| $API_{qmax}$ | 10 | MPa | Schneider, Xu, and Lehane (2008) |

See list of symbols (1) for explanation.

for each pile location was used (see Appendix A.1). API-05 shear stress generated by the pile plug was assumed to be 50% the pile outer shear-stress for the considered depth.

### 5.6.4 Setup calculation

For defining pile setup, the log – linear simplification of Skov and Denver (1988) was used, shown in the following equation.

$$\frac{R_u\ ti}{R_u\ t0} \quad A \log \frac{ti}{t0} \quad 1 \tag{5.1}$$

Where the setup ratio $R_u\ ti\ /R_u\ t0$ is equal to tenth logarithm of the time ratio, multiplied with a setup factor A. $R_u\ ti$ here represents the aged ultimate capacity of each pile evaluated from a DLT at the time $ti$. The variable i represents the time in days after $t0$. $R_u\ t0$ represents the initial, ultimate capacity of the same pile at the time $t0$. Due to combining toe and shaft capacity out of different DLTs we project the

DLT capacity representing an initial pile capacity to $t0 = 1$ day. In this way, comparable setup factors with the literature can be generated following recommendations of (Bullock et al., 2005a). Short time setup effects – like pore water dissipation, falsifying this projection, can be excluded due to the high porosity of the encountered soil.

## 5.7 Results

### 5.7.1 DLT – capacities

Impact driven piles, P2, P3, and P6, show an ultimate axial capacity of 15.02, 17.06 and 18.44 MN, respectively (Fig. 5.5A and Tab. 5.5). The portion of the toe capacity on the ultimate capacity varies from 20 up to 40%. In 2017, the capacities of the impact driven piles were more than doubled, reaching axial capacities of 36.28 (P2), 40.88 (P3) and 43.40 MN (P6) (Fig. 5.5B and Tab. 5.5). Differences in capacity in between these three piles were amplified by maintaining the capacity order of 2014. The observed increase in capacity seems to be dominated by changes on shaft capacity. Remarkably lower axial capacities of 22.09 (P1) 18.17 (P4) and 14.96 MN (P5) could be associated with the installation method. Averaged axial capacities grouped by their installation method led to 54% reduced capacity for the vibrated piles in comparison to the impact driven ones. Toe and shaft capacity seems to be halved simultaneously for vibrated piles compared to the impact driven once, except for P1. Toe capacity of P1 seems to be more similar with the toe capacities of the impact driven piles. For each three piles, shaft capacity is responsible for a loss in capacity of around 20 MN. The toe capacities of the vibrated piles are instead reduced around, 2 MN. It should be noted again that, as explained in detail before, the most reliable results out DLT is the total pile capacity. The shaft shear stress evaluated from DLT are given in Appendix A.2.

### 5.7.2 Capacity predictions

The prediction approach ICP-05 generates the most optimistic capacities regarding the impact driven piles (Fig. 6A) whereas UWA-05 and API-00 provide constantly lower capacities. The increased two weeks capacities for P3 have overcome the UWA-05 predictions. The higher capacity for P6 is good predicted by all approaches by its general order. Order in between P3 and P2 instead is incorrectly predicted. All approaches expected a slightly reduced capacity for P3 compared to P2. Regarding their aged capacities in 2017, the impact driven piles have even overcome even the high-capacity predictions of ICP-05 (Fig. 5.6B). Vibrated piles are over-predicted by all approaches with expect to P1. P1 is just slightly over-predicted by API-00 and by ICP-05 and under-predicted by UWA-05. Compared to the other vibrated piles, P1 is predicted to show the lowest capacity for all methods. In contrast, P1 could generate the highest capacity during DLT. All predicted capacities and DLT results are given in Tab. 5.5. The calculated shaft shear-stresses over embedment depth for the approaches are given in Appendix A.2.
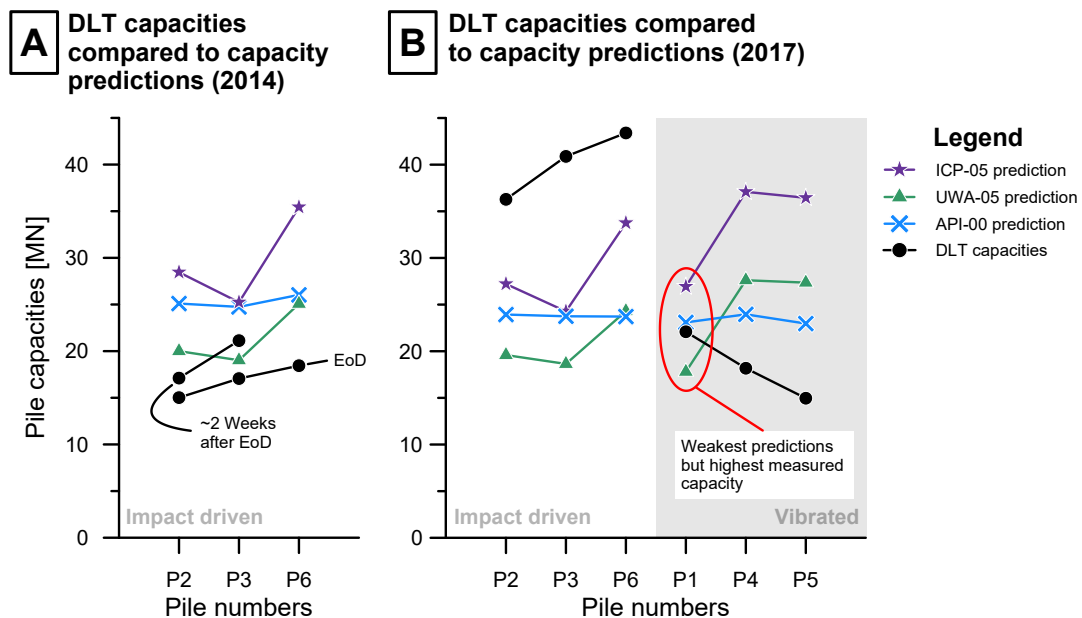


FIGURE 5.6: Comparison of total capacities developed by DLT and the most common pile capacity prediction approaches for 2014 **(A)** and 2017 **(B)**.

### 5.7.3 Setup of Impact-driven piles

Setup factors after Skov and Denver (1988) and setup ratios for the impact driven piles are given in Fig. 5.7. It can be seen, that pile P2 and P3 generated a moderate increase in capacity of +14% (P2) and +25% (P3), after an aging time of 13 and 14 days, respectively. This setup ratio corresponds to a setup factor of $A \approx 0.12$ for P2 and $A \approx 0.2$ for P3. After around 1000 days of aging, these setup factors increase for both piles reaching values of $A \approx 0.47$ (P2) and $A \approx 0.46$ (P3). P6 could generate a setup factor of $A \approx 0.45$ with its first restrike in 2017 after around 1000 days of aging. By averaging the individual setup ratios of all three impact driven piles for 2017, a capacity increase +138% is generated corresponding to a setup factor $\bar{A} \approx 0.46$.

TABLE 5.5: Measured pile capacities compared to pile predictions.

| Pile Unit | Method - | $t_i$ d | Rs MN | Rt MN | Ru MN | API MN | ICP MN | UWA MN | Ru\UWA MN |
|---|---|---|---|---|---|---|---|---|---|
| P2 | ID | 0 | 9.03 | 5.99 | 15.02 | 25.1 | 26.3 | 20 | 0.75 |
| P3 | ID | 0 | 13.72 | 3.34 | 17.06 | 24.74 | 25.24 | 19.02 | 0.9 |
| P6 | ID | 0 | 13.23 | 5.21 | 18.44 | 26.03 | 35.44 | 25.08 | 0.74 |
| P2 | ID | 14 | 12.76 | 4.35 | 17.11 | 25.1 | 26.3 | 20 | 0.86 |
| P3 | ID | 13 | 16.46 | 4.67 | 21.13 | 24.74 | 25.24 | 19.02 | 1.11 |
| P2 | ID | 1031 | 30.29 | 5.99* | 36.28 | 23.93 | 25.27 | 19.59 | 1.85 |
| P3 | ID | 1031 | 34.36 | 6.52 | 40.88 | 23.75 | 24.27 | 18.64 | 2.19 |
| P6 | ID | 1018 | 38.28 | 5.11 | 43.4 | 23.72 | 33.75 | 24.29 | 1.79 |
| P1 | V | 1027 | 16.46 | 5.62 | 22.09 | 23.09 | 24.9 | 17.8 | 1.24 |
| P4 | V | 1024 | 14.74 | 3.44 | 18.17 | 23.95 | 37.09 | 27.61 | 0.66 |
| P5 | V | 1022 | 12.42 | 2.54 | 14.96 | 22.96 | 36.45 | 27.35 | 0.55 |

*Toe capacity used from EoD due to insufficient toe activation in 2017 after Hussein, Sharp, and Knight (2012)
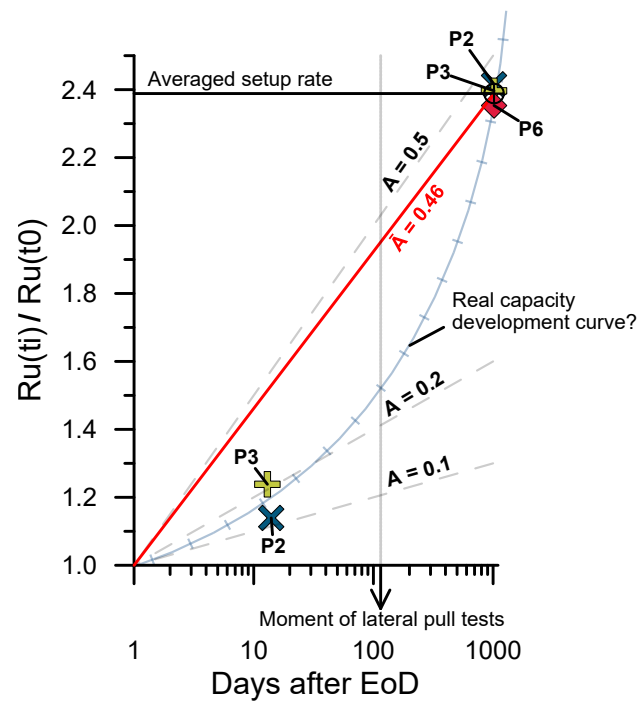


FIGURE 5.7: Setup ratios and setup rates after Skov and Denver (1988) for the three hammer driven piles and their calculated mean.

## 5.8 Discussion

### 5.8.1 Installation effects after 1000 days of aging

Our DLTs showed that various installation methods lead to dramatic varying axial capacities even after 1000 days of aging. The vibrated piles were not able to get in balance with the higher capacities of the piles installed with the same geometrics and in the same soil by impact driving (Fig. 5.5). By comparing the total capacity of vibrated and impact driven piles, an unadjusted reduction ratio of $ax.Red \approx 0.45$ can be calculated for the vibrated piles after Eq.5.2.

$$ax.Red \approx \frac{Ru\ V}{Ru\ ID} \tag{5.2}$$

Thus, this value represents a factor that capacity of an impact driven pile should be multiplied to get the capacity of its vibrated equivalent after 1000 days of aging. To get rid of interfering influence of different soil qualities, the total capacities $R_u$, obtained for DLT, were normalized to a pile capacity prediction method. Since the soil properties were already included into these calculations – in the form of cone resistance data – the effect of different soil profile can be minimized. The UWA-05 predictions out of Tab. 5.5 and Fig. 5.6 were used for these normalizations. As a result, the reduction factor evolves from $ax.Red_u \approx 0.45$ to 0.42 slightly amplifying the differences in axial capacity (Fig. 5.8).
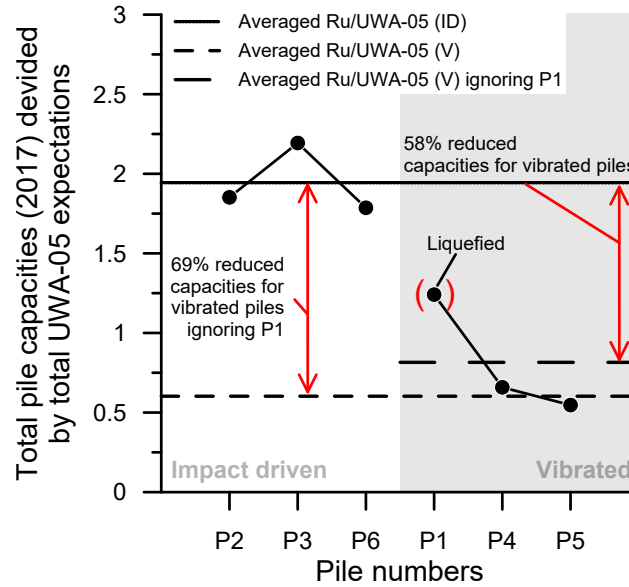


FIGURE 5.8: DLT capacities of 2017 normalized by UWA-05 expectations.

Further, P1, among the other two vibrated piles, stands out by showing much higher normalized capacity (Fig. 5.8). An explanation for its special behavior can be found from its installation procedure. In contrast to the other vibrated piles, P1 got stuck by reaching by arriving in thick till layer at 17 mbgl (see Fig. 5.9A). After around 3.6 min of active driving necessary to embed these 17 meters, 9 more minutes were needed for only one additional meter. A reduced installation frequency occurred during these second installation phase without changing any vibrator specification.

The subsequent observations such as massive shaking of the ground and the formation of a water fountain (Fig. 5.9B) together with a sinkhole (Fig. 5.9C) are interpreted as signs of an active liquefaction which seems to result out of this kind of hard driving. It can be assumed, that the liquefaction around P1 also led to its devi-
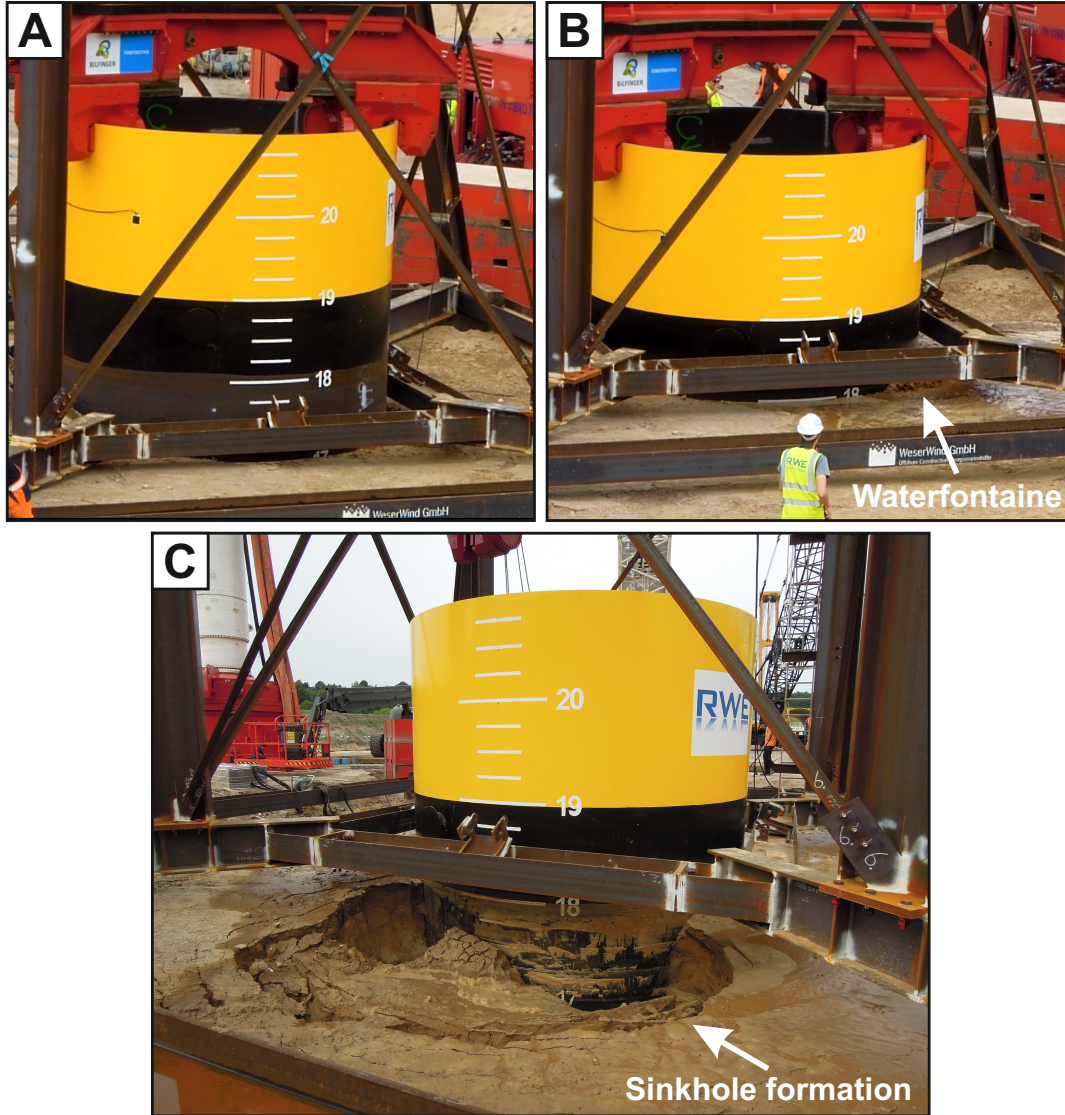


FIGURE 5.9: Impressions of vibratory pile driving of P1 (provided by Fraunhofer-Gesellschaft); **A:** Pile 1 reaches an embedment depth of 17 m after various driving interruptions and a summarized active installation time of 3.6 min; **B:** After additional 9 min of driving, an embedment depth of 18 m is reached. The formation of a water fountains could firstly be recognized at the southwestern side of the pile. **C:** Formation of a one-meter-deep sinkhole after driving and water drainage.

ating capacity. For this reason, P1 is excluded from further interpretations. Without P1, the differences between the three impact and the left two vibrated piles were strengthened, generating a final adjusted reduction factor of $ax.Red_u$ 0.31 (Fig. 5.8). Thus, a vibrated pile regarding our dimension and soil conditions were just able to show less than one third of the axial capacity of its impact driven pile equivalent. This amount of reduction is outstanding compared to existing literature, focusing on the same topic. Studies like Mosher (1990), Fischer et al. (2013), DFI (2014),

and Remspecher (2014) observed although the same trend of weaker vibrated piles, but recognized maximum reduction factors of $ax.Red$    0.58 in contrast. By investigating the sources of these deviating capacities, it seems that reductions in shaft as well as in toe capacities are responsible for the reduced vibrated ultimate capacities (Figs. 5.5 and 5.8). By normalizing the toe capacities out of DLT to their toe prediction, the deviations become more clearly (Fig. 5.10). A toe-reduction factor
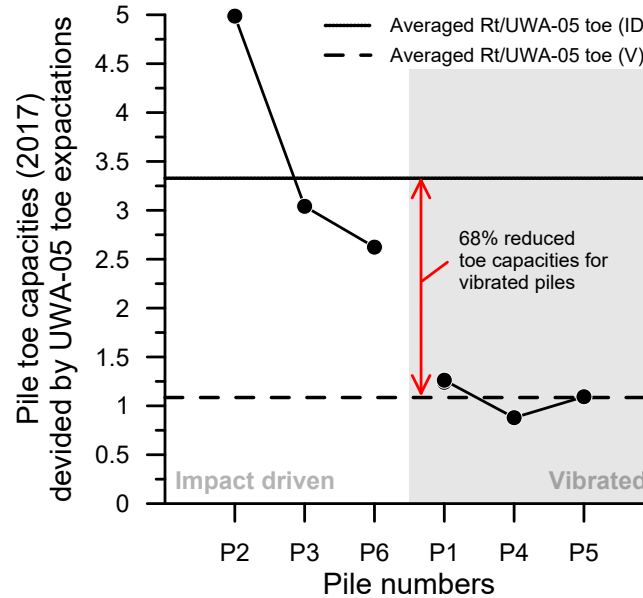


FIGURE 5.10: Toe capacities (2017) normalized by UWA-05 toe expectations.

of $ax.Red_t$    0.32 can be determined which is nearly identical to the ultimate reduction factor $ax.Red_u$    0.31 . Thus, assumptions undertaken by Mosher (1990), DFI (2014), and Remspecher (2014) that a usage of pile vibration for pile installation would lead to a reduced toe capacity might be confirmed, even if the difference in shaft capacity provides the highest portion. However, the assignment of the sub-capacitances from the CAPWAP data is done with an increased uncertainty, slightly lowering the expressive power of this toe-reduction factor. Because this toe-capacity is known to be less or even not effected by setup at all (Axelsson, 1998; Skov and Denver, 1988), we assume that these differences reflect mainly EoD conditions. Regarding the shaft capacities isolated, too many unknowns hamper further interpretation. We are unable to determine whether the differences in shaft capacity observed in 2017 between the two installation methods were already present in 2014 or developed over time out of different setup rates. A combination of both – different EoD capacity as well as different setup rates – would also be plausible. On the other hand, we can determine that these capacity behaviors dramatically deviate to reduced scale pile behaviors. In experiments using the identical test location and pile materials by Chapter 4, vibratory driven piles developed similar capacities shortly after EoD and even higher mean setup rates than their impact driven pile equivalents. Chapter 4 so partially confirmed assumptions done by Lim and Lehane (2014) or Anusic et al. (2019a) before, that a more disturbing installation method like pile vibration would lead to higher setup rates. This behavior cannot be confirmed by this study. Otherwise more similar axial capacities would be observable after these

three years of aging. Rather it seems, that the pile size or the magnitude of energy induced into the soil during driving also effects their capacity evolution. The so induced different setup might finally be responsible for the deviating behaviors of our big piles in contrast to smaller pile projects conducted by Lim and Lehane (2014) or Anusic et al. (2019a). This is consistent with the assumptions of other studies that relate either the initial pile capacity and/or its setup to size/energy used in its deployment (e.g. Randolph, Dolwin, and Beck, 1994; York et al., 1994; Rimoy et al., 2015; Zhang and Wang, 2015; Anusic et al., 2019a, or Chapter 4).

### 5.8.2   Comparison of axial and lateral loading data

It is of interest to compare the evaluated installation effect on the axial capacity with those of the lateral capacity of the same piles. Achmus et al. (2020) presented these lateral capacities in form of secant stiffnesses of the load-deflection curves reading three increasing static lateral load increments (Tab. 5.6). The results of the first load increment (in that study up to 5 MN) are used in the following, since the initial stiffness of the foundation is often very important for offshore piles design. They used 3D FEM analysis to correct the results for slightly different soil profile in each pile location and provide a reduction factor for the effect of vibratory installation in comparison for impact driving on the initial pile stiffness. A direct comparison of these ratios to the one determined in this study for axial capacity (Fig. 5.11) evaluates, that lateral initial stiffness and axial capacity are both constantly reduced due to pile vibration. Additionally, the very initial capacity is slightly less affected than the axial capacity in all three cases. This could indicate that the lateral capacity reacts less sensitive than the axial capacity to pile vibration, although a mean reduction in capacity of -44% appeared. Axial capacity was reduced in mean by -69% by pile vibration instead. We assume that this reduced sensitivity of the lateral capacity to the installation method is to be found in the volume of soil activated during loading. Where axial capacity is mostly generated by a thin soil layer around the pile mantel, the lateral capacity activates a hole soil wedge, and thus probably more distant and by installation less affected soil (Ashour, Norris, and Pilling, 1998). Conversely, a smaller reduction of this lateral stiffness (Fig. 5.11) could thus indicate that the disturbances induced by the pile vibration are also concentrated in the near-pile region. The fact that the differences in lateral load continue to equalize at higher lateral load levels (Tab. 5.6) support this assumption, since higher load levels also lead to the activation of even more soil further away for the pile. Literature data concerning the issue of lateral capacity and installation effect determined slightly contradictory behavior. The only one study exists tackling vibrated axial and lateral capacities in comparison to impact driven equivalents – to the authors knowledge – is given by (Anusic et al., 2019b; Anusic et al., 2019a). Where axial capacities in these studies were similarly reduced during pile vibration (already discussed), their lateral capacities provided a different behavior. Thus, the piles installed at Shenton Park (Western Australia) provided an increase in lateral stiffness instead. This improved lateral stiffness response is explained by Anusic et al. (2019b) in kind of a soil compaction that took place around the piles during vibration. It is conceivable that differences in soil density between these two test sites lead to these contradictory results. Where the soil in Altenwalde is mostly stored in a dense to very dense condition (Fig. 2D), the cone resistance at the test site of Anusic et al. (2019b) and Anusic et al. (2019a) indicates a much loose storage of the sand $5\,MPa \leq q_c \leq 10\,MPa$. Thus, we assume, that loose soils might be easily compacted during pile vibration in even more distant areas around the pile, leading to increases in stiffness i.e., lateral capacity. For dense

soils like encountered at the Altenwalde test site, loosening in these regions might dominate, reducing lateral capacity following pile vibration. Axial capacities seems to be dominated by other installations effects like explained by e.g. Chapter 4, more in-sensitive to soil primary conditions. It worth mentioning that the size or energy influence cannot be excluded due to the noticeable different pile sizes in these two experiments.
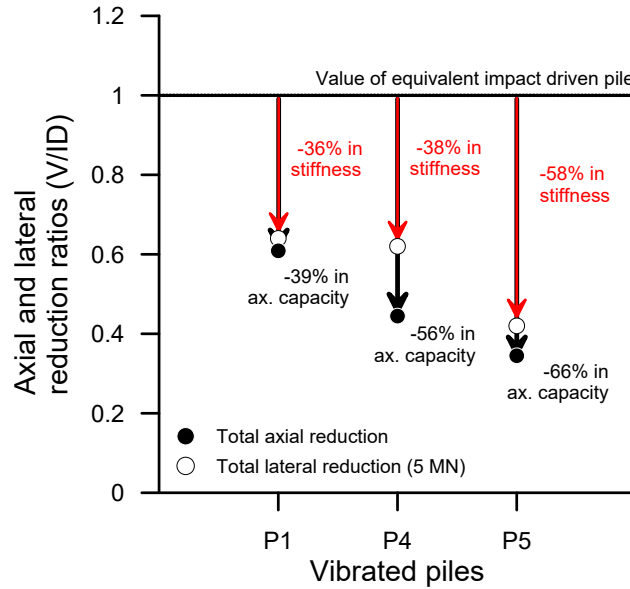


FIGURE 5.11: Comparison of lateral and axial capacity reduction ratios. Initial stiffness reductions out of Achmus et al. (2020).

TABLE 5.6: Lateral secant stiffnesses and reduction ratios out of Achmus et al. (2020).

| Pile | Method | $Ksec$ [MN m$^{-1}$] | $Ksec$ [MN m$^{-1}$] | V/ID (5 MN) | V/ID (15 MN) |
|------|--------|------|------|------|------|
| P1 | V | 294 | 136 | 0.64 | 0.96 |
| P2 | ID | 459 | 142 | | |
| P3 | ID | 435 | 124 | 0.62 | 0.76 |
| P4 | V | 268 | 94 | | |
| P5 | V | 205 | 80 | 0.42 | 0.61 |
| P6 | ID | 491 | 131 | | |

### 5.8.3 Setup of impact driven piles

A detailed setup history could be traced for the impact driven piles since multiple DLT exist at different times after EoD. Their capacity was increased up to 2.4 times compared to the initial EoD capacity after around 1000 days of aging. Referred to the log-linearly relationship developed by Skov and Denver (1988), this corresponds to an setup factor of $\bar{A}$ 0.43 (Fig. 5.7). This factor is in good agreement with other studies like e.g. Axelsson (2000) and Chow et al. (1998) recommending a setup factor of 0.15 $A$ 0.5 for a broad database of driven piles. Additionally, their

capacity development over time does not follow the straight log-linearly relationship proposed by Skov and Denver (1988). Instead, their capacity evolution is better represented by a strongly bended hyperbolic curve (see Fig 5.7). Capacity increase seems to be amplified after passing a midterm aging phase of around 2 weeks after EoD. This hyperbolic curve was also observed in reduced-scale pile experiments done at Chapter 4 concerning the identical test side. Because lateral loading test fell in between the last DLTs and most likely disturbed the natural aging characteristics, these setup values must even be seen as rather conservative. Also the partial excavation of the upper one up to two meters of the piles before the final DLT in 2017 – as well as the multiple axial testing of all piles itself (Jardine, Standing, and Chow, 2006) – must be mentioned as potential setup reducing factors. By focusing on the development of toe capacities in Fig 5.10, we could show, that toe capacity seems to be not involved into the setup at all. This finding is in a good accordance to e.g. Skov and Denver (1988) and Axelsson (1998), who also recognized a mostly unchanged toe capacity over time.

## 5.9 Conclusion

With the help of this study, we can conclude the following points:

- Three years aged vibrated, large diameter piles would tend to show just about one third of the axial capacity shown by its impact driven equivalent pile, when installed in dense sand.

- Shaft and base capacity seem to be similar responsible for capacity reductions resulting out of pile vibration.

- Axial capacity difference between impact driven and vibrated piles are increased for larger piles. A size and/or energy influence is assumed.

- Axial pile capacity reacts more sensitive to pile vibration than lateral capacity.

- The axial load capacity of large diameter impact driven piles in dense quartz sand could increase up to 2.4 times after 1000 days of aging.

- Setup characteristic of impact driven piles is best described by a strongly bended hyperbolic curve over the tenth logarithm of time.

Regardless of the reasons that may have caused the dramatic differences, further research in this area is imperative.

## 5.10 Acknowledgments

**Chapter 6**

# Corrosion effects on axial pile capacity

This study was submitted to Géotechnique on February 22th (2022) and is currently in revision.

## 6.1 Authors

1. **Alexander V. Busch**[1]

2. **Max O. Kluger**[1,2]

3. **Tobias Mörz**[1,3]

[1]MARUM – Center for Marine Environmental Sciences, University of Bremen, Bremen, Germany
[2]School of Science/Te Aka Mātuatua, University of Waikato, Hamilton, New Zealand
[3]Geo-Engineering GmbH, Bremen, Germany
 Corresponding author: abusch@marum.de

## 6.2   Abstract

Increase in surface roughness by corrosion processes has long been neglected as potential factor influencing pile setup. However, recently there has been an increasing number of studies who referred pile setups largely or solely to corrosion and sand incrustation. No research exists determining the potential impacts of corrosion to pile capacity development. Therefore, we sampled steel and crust surfaces from a steel monopile having been aged for four years in sand. Surface roughness measurements and interface direct shear testing were performed to quantify changes for friction angles. The impact of friction changes on pile capacity were modeled using ICP-05 and UWA-05 for a large- and small-diameter geometry and referenced by field data. We can show that corrosion can significantly contribute to temporal pile capacity gains. Evidence have been found that the maximum and critical interface friction angles evolve differently considering the same changes in roughness. Also, differences in shearing behavior to literature were observed, being potentially a result of the naturally corroded surfaces sheared in our study. A strong, maybe exaggerated sensitivity of the capacity prediction models to pile diameter was observed. Effects causing an increase in surface roughness, should be reconsidered as an important factor influencing pile setup.

## 6.3   Introduction

Axial capacity gain of piles over time is commonly described as aging or setup and was observed to play an important role for numerous types of materials (e.g. wood, concrete, mild steel, stainless steel), environments (e.g. field, laboratory), and soil conditions (e.g. degree of saturation, relative densities) (e.g. Chow, 1996; Axelsson, 2000; Bullock et al., 2005b; Lim and Lehane, 2014; Gavin et al., 2015; Rimoy et al., 2015; Carroll et al., 2017; Carroll et al., 2019; Gavin and Igoe, 2019; Bittar et al., 2020). Nevertheless, the driving mechanisms of setup are still poorly understood, hampering accurate setup predictions. A better understanding of the pile setup would have direct benefits for the design of piles and their efficiency. Since piles are often used as foundations for offshore wind turbines, a better predictable setup could directly contribute to the transition of the world's energy supply to more renewable sources. It is widely accepted that setup is mainly controlled by the stress field surrounding the pile, which changes with time from the moment the pile has been driven into the ground or during pile loading (Bullock et al., 2005b; Gavin, Igoe, and Kirwan, 2013; Zhang and Wang, 2015). The concepts of stress equilibrium and friction fatigue have been proposed in order to explain the influence of the stress field on pile setup (Lim and Lehane, 2014, and Chapter 4). Corrosion of the pile surface as another effect potentially influencing setup has often been considered just as minor contributor (e.g. Gavin et al., 2015). However, other researchers argued that changes in surface roughness due to progressive corrosion and iron oxide incrustation have the potential to significantly increase the friction of the pile surface and, thus, its capacity (Liu et al., 2019). Two commonly used pile capacity prediction models (i.e. ICP-05, UWA-05 after Jardine et al., 2005; Lehane, Schneider, and Xu, 2005; Lehane, Schneider, and Xu, 2007 consider surface roughness and interface friction into their capacity equations. This provides a potential gateway and enables capacity modeling to help solving this dispute. Challenge still exists to determine these two parameters in order to precisely predict setup from changes in surface roughness and friction behavior. In this study, interface friction was determined for steel surfaces and natural iron oxide

sand crusts of different roughness through a modified direct shear apparatus. The differences in surface roughness represent subsequent stages of aging and corrosion, ranging from uncorroded (i.e. directly after pile manufacturing) to heavily corroded (i.e. after four years in contact with the ground). The steel surfaces samples were drilled from a 20 m long, open-ended monopile with an inner diameter of 4.3 m, that was installed in a sand pit near Cuxhaven, Germany. This location has already been used for several large-scale industrial research projects as a test site due to similarity of its dense to very dense sand subsoil with typical ground conditions in the German North Sea (Achmus et al., 2020). Among others, this test site comprises pile setup data for six large-diameter, open-ended monopiles and 44 small-diameter, closed-ended piles (Chaper 4 and 5 or Goodarzi et al., 2019). We measured surface roughness and interface friction of 44 samples and determined the proportion of potential corrosion scenarios on pile setup by modeling using the ICP-05 and UWA-05 capacity prediction approaches. The modeled pile capacities and setups, using potential corrosion scenarios, were compared with those published for large- and small-diameter piles manufactured from the same steel type and installed at the same test site. The scale effect was considered. The following three questions are addressed in this study:

1. How do surface roughness and interface friction change with different stages of corrosion and incrustation?

2. How does interface friction depend on surface roughness?

3. How much of pile setup is governed by corrosion?

## 6.4   Materials and methods

### 6.4.1   Field sampling

The sand pit near Cuxhaven, Germany (53°48.0'N, 8°39.4'E), comprises dense to very dense sandy subsoil of Pleistocene age, being similar to ground conditions in the German North Sea (Fig. 6.1). Six open-ended monopiles with 4.3 m outer diameter ("large-diameter piles" hereafter) were installed in 2014 for studying the influence of different installation methods (i.e. impact driving, vibratory pile driving) on lateral bearing capacity (Achmus et al., 2020). Three of the large-diameter piles (P1, P3, P5) were installed by vibratory pile driving, whereas the others (P2, P4, P6) were installed by impact pile driving. Axial pile capacities and setups of the large-diameter piles were presented at Chaper 5 and by Goodarzi et al. (2019). In addition, 44 small closed-ended piles with a diameter of 3.5 cm ("small-diameter piles" hereafter) have been installed within 30 m distance to the large-diameter piles in order to further understand the influence of corrosion and installation methods on setup characteristics (Chaper 4). The steel surface samples tested in this study were obtained from the large-diameter pile P1 in April 2018. By this time, the pile had been in contact with surrounding natural sand deposits for  1,400 days (  4 years). Pile P1 was chosen for sampling because at the time of sample collection this large-diameter pile was the only one where access could be established. The other five large-diameter piles had been either already dismantled to follow environmental regulations or were cut close to the ground water level, being seasonally variable but averages at  2.5 m below the ground surface at the time of sampling. The outside surface of the uppermost parts of the large-diameter pile was painted by a corrosion protection (Fig. 6.2). The steel surface underneath the corrosion protection
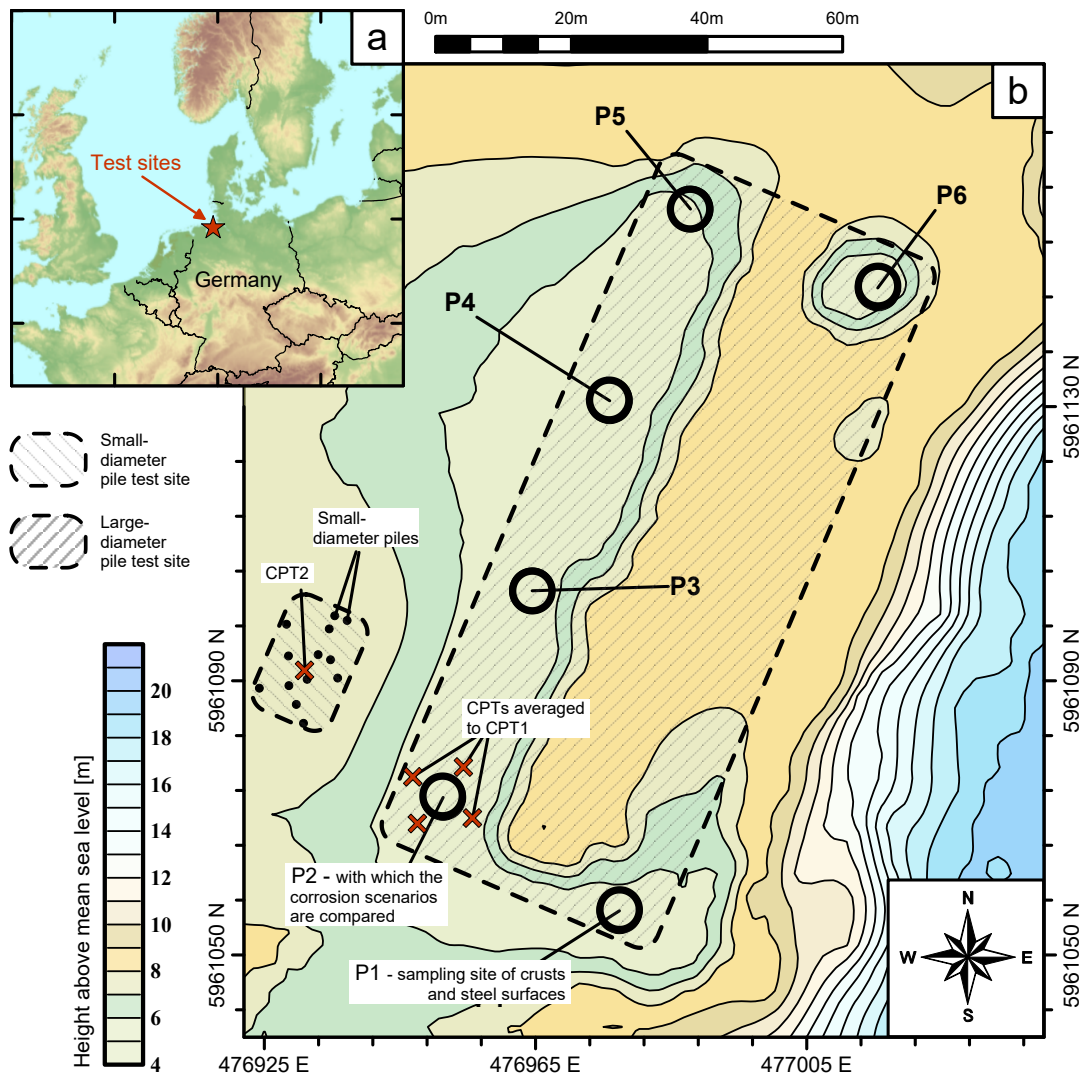
FIGURE 6.1: Location of both test sites in a sand pit near Cuxhaven, Germany. Large-diameter piles are labelled with P1-P6. Source of administrative boundaries and topography are EuroGeographics and the European Environment Agency (EEA), respectively.

paint was essentially unaltered since the time of painting shortly after pile manufacturing. In order to gain access to the corrodible surface below ground level, a 2.5-m-deep trench was excavated around the large-diameter pile within the unsaturated zone until the ground water level was reached (at 4 m below pile head). The steel surface below ground level was extensively covered by an up to 10-mm-thick sand crust, which is tentatively considered by us to be an iron oxide-rich corrosion and/or cementation product. Some of these sand crusts ($1m^2$) could be sampled by carefully separating them from the pile mantle using scrapers (Fig. 6.2b). In a later preparation step, these sand crusts were then mounted on dummy disks. This unique situation at the large-diameter pile P1, thus, enabled the sampling of five surface categories of different roughness, mostly representing different potential stages of corrosion (Fig. 6.3c). These are: (1) "preserved surfaces" (i.e. fresh steel underneath the corrosion protection); (2) "air-corroded surfaces" (i.e. inner pile steel surface above ground level having been only in contact with the air); (3)

"artificial surfaces" (i.e. underneath the removed sand crusts below ground level); and the sand crusts themselves, either as (4) "adhering crusts" or as (5) "mounted crusts". A total of 18 circular 110-mm-diameter steel disks were drilled from the large-diameter pile P1 using a magnetic core drilling unit MAB 1300V (developed by BDS Maschinen GmbH), which was equipped with a carbide drill crown (Fig. 6.3a). Nine samples have been drilled from surfaces painted with the corrosion protection and nine from surfaces below ground level. Canola oil was used as cooling liquid. The least possible amount of oil was used to facilitate drilling and care was taken not to contaminate the sand crusts and steel surfaces. Steel disks were 45-mm-thick and comprised an outer (convex) and inner (concave) surface yielding a total number of 36 surfaces for subsequent testing. Sand crusts and steel disks were stored in plastic containers for transport. Silica gel was used to remove humidity from air, stopping any potential corrosion process.
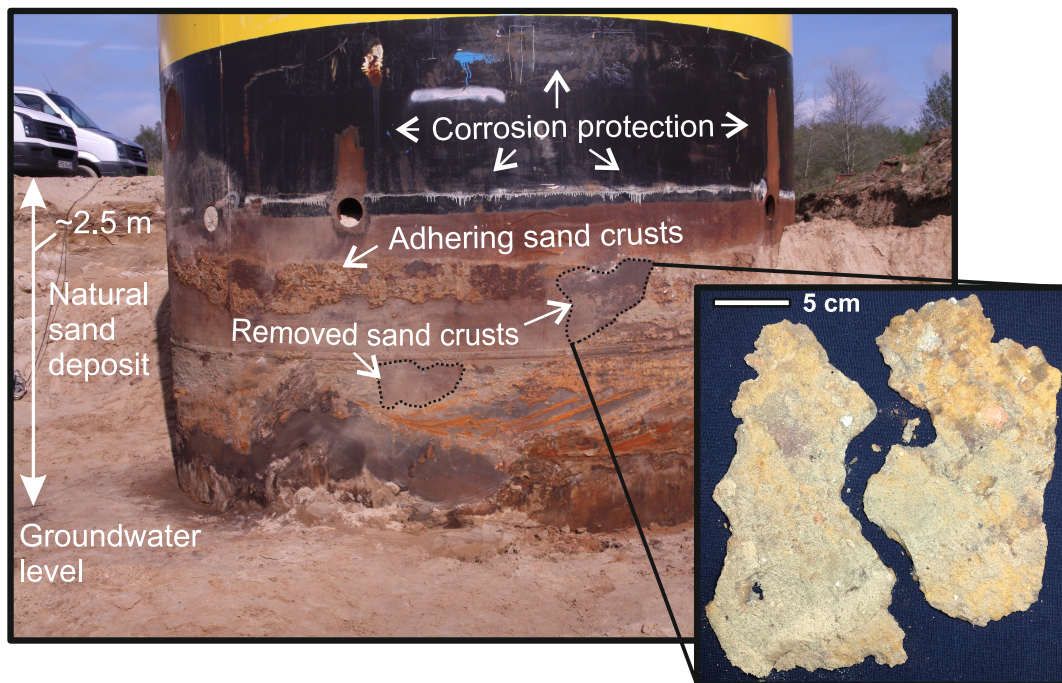


FIGURE 6.2: Excavated large-diameter monopile P1 after being in contact with the soil for ~1400 days. Inset shows iron oxide sand crust samples after being removed from the pile mantle.

### 6.4.2   Cuxhaven Sand

The Cuxhaven Sand, used for direct shear experiments, is a glacio-fluvial sediment that was deposited in the German Bight during glacial periods of the Pleistocene epoch (Sindowski, 1963; Ehlers et al., 2011). The Cuxhaven Sand was sampled from a location within the sand pit close to the large-diameter piles and has already been used in numerous laboratory studies (Fleischer et al., 2016; Kluger et al., 2021). Cuxhaven Sand is a fine to medium ($D_{50} \approx 200$ µm), poorly-graded (i.e. well-sorted) clean quartz sand with less than 3% fines content. Most grains have sub-angular to angular shapes (EN ISO 14688-1, 2018). A critical friction angle of $\varphi_{cv} \approx 32 \pm 2°$ was obtained from the angle of response (DIN ISO 4324, 1983). Minimum and maximum void ratios of $e_{min} \approx 0.47$ and $e_{max} \approx 0.85$ were determined (DIN 18126, 1996) together with a particle density of $\rho_s \approx 2650\,\text{kg m}^{-3}$ (DIN 18124, 2019).

### 6.4.3   Sample preparation

In order to facilitate direct shear testing, the diameter of the 18 steel disks was reduced to 97 mm by means of careful turning and then halved longitudinally by a cutting saw (Fig. 6.3b). Both processing steps were carried out without a cooling liquid to ovoid contamination. This process generated 36 samples with a flat base and a slightly curved shear surface (i.e. 17 concave and 18 convex steel samples) later used to determine interface friction behavior of surfaces $1-4$. Note that one concave sample was used for mineralogical analyses and therefore not further considered in this study. Strongly hardened cutting blades were used able to adjust sizes of steel samples without requiring a cooling liquid. The corrosion protection paint of the nine convex steel samples representing the outside of the large-diameter pile surface above ground level was removed using a mordant. The sand crusts collected from the large-diameter pile surface below ground level (i.e. surface 5) were mounted on a total of nine dummy disks using a low-viscous and slowly drying epoxy resin (Araldite 2020) (Fig. 6.3b). After a curing period of 24 hours, the mounted sand crusts were soaked by the same epoxy resin. Special care was taken so that only the grain framework of the crusts was slightly soaked to support their inner grain structure without too much affecting the outer surface roughness of the crusts. The soaking of sand crusts with epoxy resin may have affected the shear behavior in this study, a systematic error, which we did not quantify. Steel disk protruding parts of the sand crusts were carefully cut off by a sharp knife after another curing period of 24 hours.
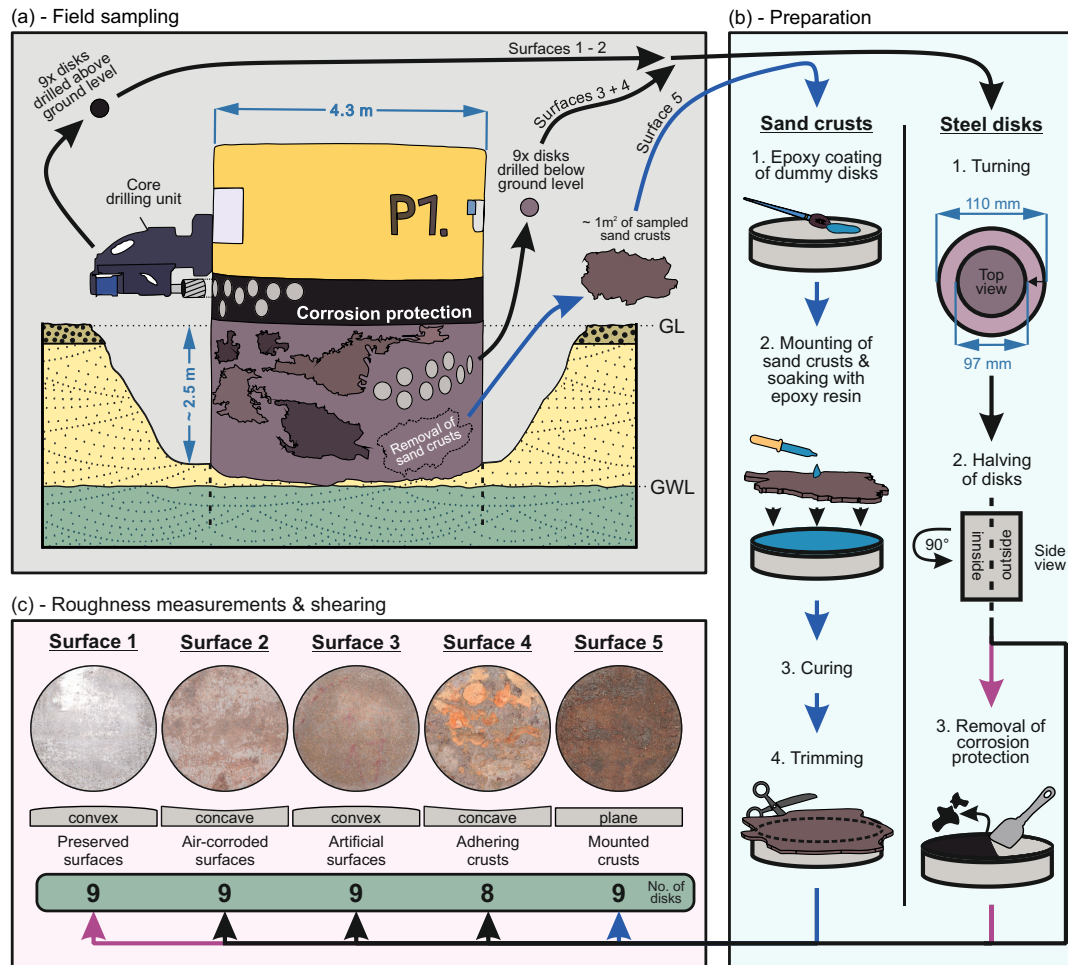
FIGURE 6.3: Sampling and sample preparation procedure. **(a):** Sampling of steel disks and sand crusts from large-diameter pile P1. **(b):** Preparation of steel disks. **(c):** Final grouping of the steel disks before roughness analyzes and shearing started. GL, ground level, GWL, ground water level

### 6.4.4 Surface roughness measurements

Surface roughness measurements of steel and sand crust samples were performed using strip projection (3D profilometer VR5000) and an optical digital microscope (VHX 6000). Strip projection was used for a precise quantification of initial surface roughness of all samples following DIN EN ISO 25178-3 (2012). The digital microscope was used to analyze changes in surface roughness after subsequent direct shear experiments. Changes in surface roughness due to direct shear experiments were always within the measurement tolerances of the digital microscope. Therefore, it was considered that the surface roughness was not significantly influenced by the direct shear experiments. Thus, the initial surface roughness values obtained prior to the shear experiments were used in the following to classify the surfaces. For reducing influences from the convex and concave curvature as well as microscopic roughness of the steel surfaces on roughness measurements, a square correction, a low pass filter of 0.2 mm, and a high pass filter of 100 mm were used during the post-processing phase. Mean centerline surface roughness Sa and mean peak height P were considered to quantify the surface roughness of steel surface and sand crust

samples. $Sa$ is the two-dimensional version of the commonly used one-dimensional mean centerline surface roughness $R_{CLA}$ after e.g. Gadelmawla et al. (2002). An average mean centerline surface roughness $\overline{Sa}$ was calculated for each of the five surfaces representing different stages of corrosion (Fig. 6.3c).

### 6.4.5    Direct Shear experiments

Direct shear experiments followed DIN EN ISO 17892-10 (2019) and were performed using GIESA shear apparatuses. Air pluviation was used to reconstituted Cuxhaven Sand into the direct shear sample boxes (Lagioia, Sanzeni, and Colleselli, 2006). Sand grains were pluviated through a 1-m-high pluviation tower, which was equipped with three diffusers to ensure even density distribution throughout the sample. An initial void ratio of $e_0 \approx 0.52 \pm 0.05$ was reached. This initial void ratio corresponds to a relative density of $D_R \approx 86\%$ and matches in situ values of $e_{field} \approx 0.56$, reported for the natural sand deposits at the test site (Geo-Eng, 2015). Maximum friction angles $\varphi_{max}$ and constant volume friction angles $\varphi_{cv}$ were obtained on Cuxhaven Sand samples by sand-to-sand shearing (Fig. 6.4a). Maximum interface friction $\delta_{max}$ and constant volume interface friction angles $\delta_{cv}$ were obtained on experiments that comprised one of the five surfaces fixed by screws in the lower shear box and Cuxhaven Sand in the upper shear box of the direct shear apparatus. Because surface samples exhibited slightly different heights, height adjustments (i.e. circular steel disks of different height) were used so that the top of each surface sample was aligned with the shearing gap. For compensation of the convex and concave surfaces of samples, the upper box of the direct shear apparatus was individually customized to provide opposite curvatures (Figs. 6.4b and 6.4c). Because of the different nature of surface samples, the shearing gap needed to be slightly adjusted between the different tests, being largest for the adhering and mounted sand crust samples (surfaces 4 and 5) due to their higher topography (Fig. 6.4d).

The shearing gap was chosen as small as possible to prevent collision between surface sample and upper shear box, while minimizing sediment loss through the shearing gap. The width of the shearing gap is known to influence the results of the shear experiments (e.g. angle of dilatancy) and especially the large strain friction behavior in direct shear (Fu et al., 2015). The angle of dilatancy was not further considered in this study. Each surface sample was sheared three times in order to obtain the direct shear response of the interface at three different normal consolidation stresses $\sigma_N$ of 100, 200, and 300 kPa. For every test, a new Cuxhaven Sand sample was reconstituted into the upper shear box of the direct shear apparatus. In addition, six direct shear tests were performed on Cuxhaven Sand with two for each of the three consolidation stresses. The normal stress was increased stepwise until the desired normal consolidation stress was reached. The sample was left for consolidation for at least 30 mins before sharing started. Shearing was performed at a displacement rate of $\dot{s} \approx 0.5\,\text{mm/min}$. The samples were sheared dry in order to prevent potential corrosion to take place during the experiment. Water saturation is known to have neglectable influence on shear behavior of sand (Skinner, 1969; Dai, Yang, and Zhou, 2016). The direct shear experiments ended after reaching a shear displacement of $s \approx 11\,mm$. Constant volume interface friction angles were determined from the average shear stress $\tau$ between shear displacements of $7\,mm \leq s \leq 11\,mm$. Finally, friction angles were calculated by plotting maximum and constant volume shear stresses vs. normal consolidation stress and by using a linear regression with zero intercept. The same procedure was used to derive maximum and constant volume interface friction angles.
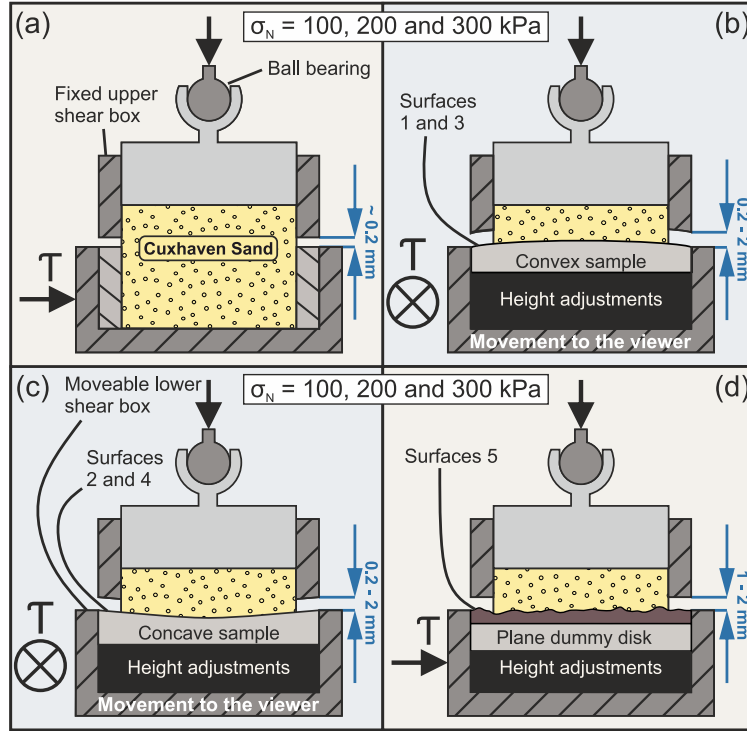
FIGURE 6.4: Side views of direct shear experiments. **(a):** Configuration for sand-to-sand shearing. **(b):** Configuration for shearing of surfaces 1 and 3 (i.e., preserved and artificial surfaces). **(c):** Configuration for shearing of surfaces 2 and 4 (i.e., air-corroded steel surfaces and adhering sand crusts). **(d):** Configuration for shearing of surface 5 (i.e., mounted sand crusts)

### 6.4.6 Axial pile capacity modeling

The influence of corrosion on axial pile capacity and setup was further studied by implementing values of mean centerline surface roughness and constant volume interface friction angle obtained in this study into ICP-05 and UWA-05 pile capacity prediction models (Eqs. 6.1 - 6.6).

$$Qs = \pi D \int_{z_{tip}-L}^{z_{tip}} \tau_f \, dz \tag{6.1}$$

Where $Qs$ and $\tau_f$ are the pile shaft capacity and shear stress along the pile surface, respectively, determined either by ICP-05 or UWA-05 pile capacity prediction models (Jardine et al., 2005; Lehane, Schneider, and Xu, 2005). $D$ is the outer pile diameter; $z_{tip}$ is pile tip depth; and $L$ is the embedment length of the pile. The shear stress along the pile surface via ICP-05 model is calculated following Eqs. 6.2 and 6.3.

$$\tau_{f,ICP} = a \left[ 0.029 b \, q_c \left( \frac{\sigma_{v0}}{100 \, kPa} \right)^{0.13} \left( max \left[ \frac{h}{R}, 8 \right] \right)^{-0.38} + \Delta\sigma_{rd} \right] tan \, \delta_{cv} \tag{6.2}$$

$$\Delta\sigma_{rd} = \left( 4 \cdot 185 \, q_c \, q_{c1N}^{-0.7} \right) \frac{2\overline{Sa}}{D} \tag{6.3}$$

Where a is 0.9 for open-ended piles in tension and 1.0 for all other cases; b is

0.8 for piles in tension and 1.0 for piles in compression; $q_c$ represents cone resistance data obtained for each depth increment; $\sigma_{v0}$ is the effective vertical stress; $h$ is the distance above pile tip depth; $R^*$ is the equivalent pile radius calculated from $R^* = \left(R^2 - R_i^2\right)^{0.5}$, with $R_i$ being the internal pile radius; $\Delta\sigma_{rd}$ is the dilative stress component; and $q_{c1N} = \frac{q_c}{100\,kPa} / \left(\frac{\sigma_{v0}}{100\,kPa}\right)^{0.5}$ is the normalized cone resistance. The shear stress along the pile surface via UWA-05 model is calculated following Eqs. 6.4 – 6.6 as well as by using Eq. 6.3.

$$\tau_{f,UWA} = c \cdot 0.03 \cdot q_c \cdot A_{rs,eff}^{0.3} \cdot max\left[\frac{h}{D}, 2\right]^{0.5} + \Delta\sigma_{rd} \cdot tan\,\delta_{cv} \qquad (6.4)$$

with

$$A_{rs,eff} = 1 - IFR\left(\frac{2R_i}{D}\right)^2 \qquad (6.5)$$

$$IFR = min\left[1, \left(\frac{2R_i}{1.5}\right)^{0.2}\right] \qquad (6.6)$$

Where c is 1 or 0.75 for piles tested in compression or tension, respectively; $A_{rs,eff}$ is the effective area ratio (Eq. 6.5); and IFR is the incremental filling ratio (Eq. 6.6). In Eqs. 6.2, 6.4 and 6.5, min and max indicate, whether the minimum or the maximum of the possibilities inside the square brackets after this math operator should be used, separated by the comma. Separate consideration of the lowest $\sim$ 2 meters of P2 and the use of the clay - calculation approach (ICP-05) is omitted to lower the level of complexity. Pile capacities were predicted for two potential pile geometries reflecting existing piles of previous large- and small-diameter projects (Chapters 4 and 5).

Five corrosion scenarios were considered in this study, following simplifications shown in Fig. 6.5, by using roughness and shearing parameters determined from our study. In situ subsoil properties were determined after Chapters 4 and 5. For the small-diameter pile calculations, one representative cone penetration test (CPT) profile was used located in the center of the test site (Fig. 6.1). For the capacity calculation of the large-diameter pile P2, four CPT profiles were averaged, which were located close to the large-diameter pile test site. The five corrosion scenarios used the identical in situ subsoil properties and pile geometries but considered different surface roughness and constant volume interface friction angles; both parameters being denoted in red in Eqs. 6.1 - 6.6.

For corrosion scenario 1, the recommended parameters after API (2006) were used, considering a surface roughness of $Sa \approx 10\,\mu m$, common for steel piles before installation. Additionally, the constant volume interface friction angle was determined in dependency to the mean grain size of the subsoil. With respect to our study, this led to a constant volume interface friction angle of $\delta_{cv} \approx 28.8°$ considering a mean grain size of $D_{50} \approx 0.2mm$ (Fig. 6.6).

The other corrosion scenarios included a pile composed entirely of uncorroded, preserved steel with surface roughness and shearing parameters of surface 1 (i.e., corrosion scenario 2); a pile that has been stored outside before installation and was therefore subjected to air corrosion with parameters of surface 2 (i.e., corrosion scenario 3); and a pile, heavily corroded while being in contact with the surrounding

sand deposits, now being covered by sand crusts representing surfaces 4 and 5 (i.e., corrosion scenario 5). Corrosion scenario 4 represents a transition stage between corrosion scenarios 3 and 5. In corrosion scenario 4, the ground water level was considered as a barrier hampering any further corrosion and, thus, iron oxide sand crusts below. As a result, the pile in corrosion scenario 4 was subdivided into an upper part (above ground water level), with the surface roughness and constant volume interface friction angle of the sand crusts of surfaces 4 and 5, and a lower part (below ground water level) with parameters of surface 2. Thus, corrosion scenario 4 represents the most likely field situation (Chaper 4). All relevant parameters (i.e. soil properties, pile geometries) used for modeling are provided in Fig 6.5.
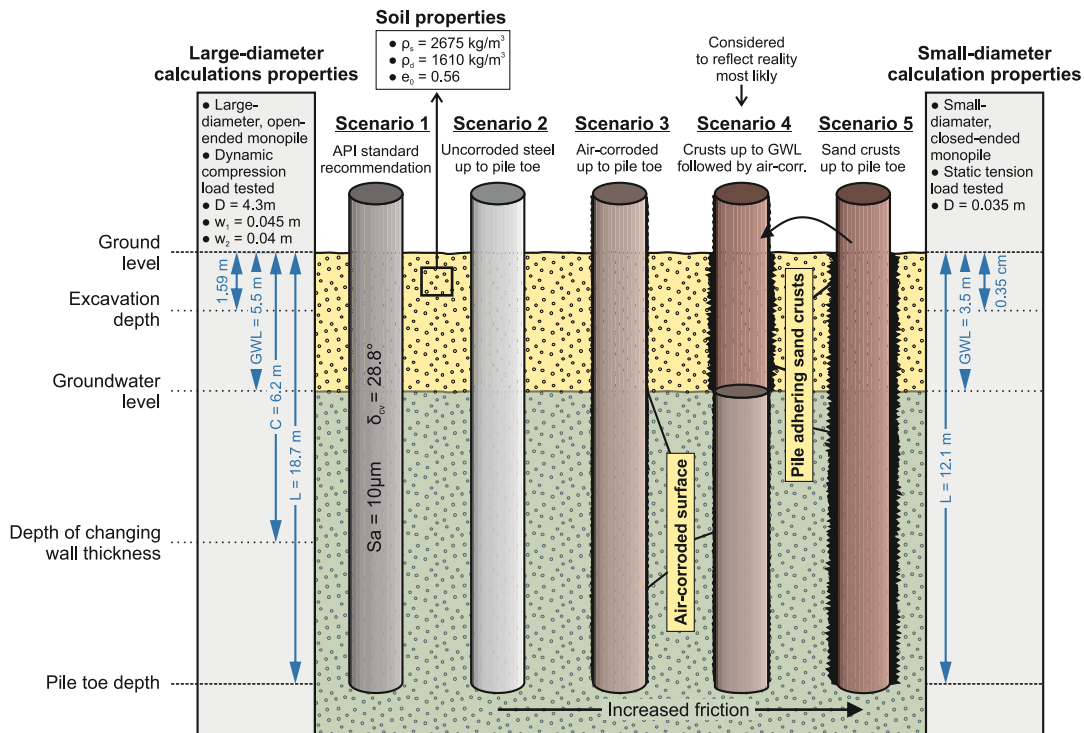


FIGURE 6.5: Corrosion scenarios and associated model input parameters for both pile geometries. $D$ - outer pile diameter; $w_1$,$w_2$ - wall thicknesses; $C$ - depth of changing wall thickness; GWL - ground water level; $L$ - pile embedment depth; $\rho_s$ - particle density; $\rho_d$ - bulk density; $e_0$ - initial void ratio.
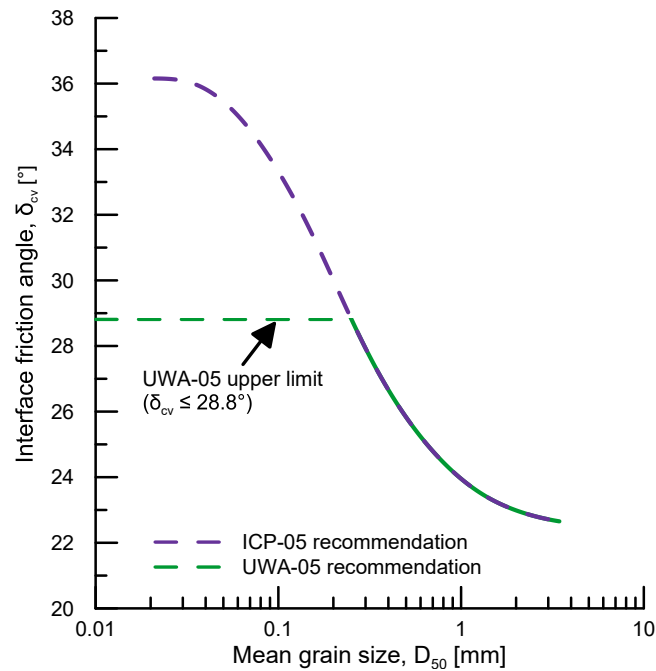
FIGURE 6.6: Relationships between interface friction angle and mean grain size used in UWA-05 and ICP-05 models as standard recommendation for pile capacity prediction following API (2006).

### 6.4.7   Comparing modeled and measured pile capacities

The potential impact of a changing surface to pile capacities was further studied by comparing the predicted pile capacities of corrosion scenarios 1 to 5 (obtained from both ICP-05 and UWA-05 models) to the pile capacities (i.e. initial and aged) measured in the field for large- and small-diameter piles. The large-diameter pile P1 (having been used for surface sampling) was not considered because it was installed by vibratory pile driving. Instead, the large-diameter pile P2 was considered, having been installed by impact driving, in order to avoid influences of the installation effect. Thus, aging times $ti$ in days after reference time, of $ti$  0, $ti$  14, and $ti$  1031, were available for large-diameter pile P2. Considering the small-diameter piles, nine shaft capacities for $ti$  1, three for $ti$  11, and three for $ti$  101 were chosen and averaged, respectively (Tab. 6.1). The field data did not provide aged pile capacities for $ti$  100 regarding the large-diameter piles and $ti$  1000 in case of the small-diameter piles. Here, aged capacities were estimated using the pile setup prediction approach of Skov and Denver (1988), together with the overall field setup trends (Tab. 6.1).

TABLE 6.1: Setup data of shaft capacities for large- and small-diameter piles installed at the test site near Cuxhaven, Germany. Capacity and setup factors from Chapters 4 and 5

|  | Shaft capacity - Qs [kN] | | | | Setup factor |
|--|--|--|--|--|--|
|  | *ti* 0 | *ti* 10 | *ti* 100 | *ti* 1000 | *A* |
| Large diameter pile P2 | 9025.0 | 12762 | 21479.5* | 30286.9 | 0.46 |
| Small diameter piles | 38.1 | 47.7 | 119.0 | 163.7* | 1.10 |

*Capacities were estimated after Skov and Denver (1988)

## 6.5 Results

### 6.5.1 Changes in surface roughness with stages of corrosion

The topography and centerline surface roughness strongly increased from surface 1 to surfaces 4 and 5, representing the different stages of corrosion and incrustations (Figs. 6.7 and 6.8). The sand crusts still adhering to the original pile surface samples or mounted on dummy disks (surfaces 4 and 5) exhibited similar surface roughness. The preserved steel surface (i.e., surface 1) provided the smoothest surface roughness (8 µm $Sa$ 15 µm) (Fig. 6.7). The steel surface corroded in contact with air (i.e., surface 2) and the artificial surfaces generated by removing former crusts from the pile (i.e., surface 3) (Fig. 6.7) provide a similar, slightly larger surface roughness (25 µm $Sa$ 108 µm). The sand crusts, having been either adhering to disk samples or mounted on dummy disks (i.e., surfaces 4 and 5) (Fig. 6.7), provided the highest surface roughness values of all surfaces (10 µm $Sa$ 668 µm). The mean peak height of all surfaces increased linearly (in log-log scale) with an increasing mean centerline surface roughness (Fig. 6.8). Individual surface samples exhibited some variability in centerline surface roughness when compared with their respective mean value, being calculated for the five different surfaces, respectively.
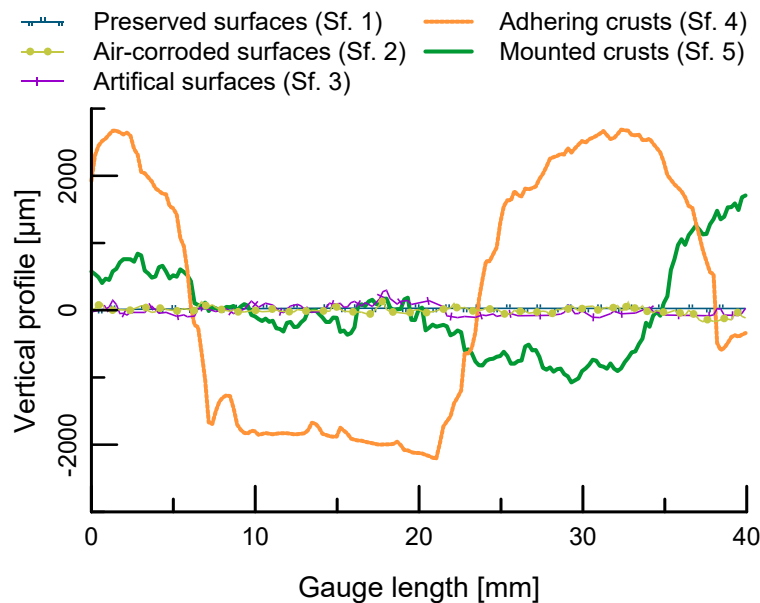


FIGURE 6.7: Exemplary topography profiles for surfaces 1 to 5. Sf. - Surface
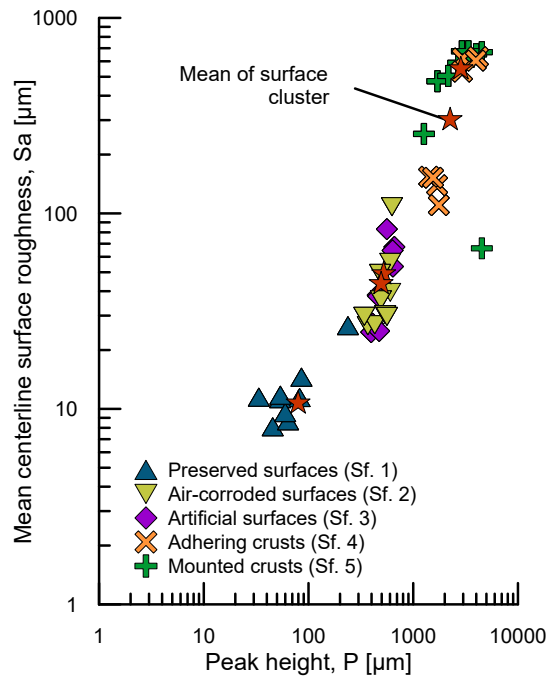
FIGURE 6.8: Surface roughness relationship for surface samples. Red star symbols indicate mean values calculated for each of the five surfaces, respectively. Sf. - Surface

## 6.5.2   Direct shear behavior of corroded surface samples

Surface roughness developments were compared to the interface friction angles with respect to the five types of surfaces representing different stages of corrosion (Fig. 6.9). Interface friction angles determined for the five surfaces at the maximum and constant volume states were observed to be always below the friction angles determined from sand-to-sand shearing. The five different surfaces systematically affected the maximum interface friction angle of Cuxhaven Sand. The preserved surfaces (surface 1) developed around 60% of the maximum friction angle determined from sand-to-sand shearing. For all other surfaces, a pronounced increase in interface friction angles appeared, reaching 92% up to 96% of the maximum friction angles determined from sand-to-sand shearing. A LOESS fit (locally weighted scatter-plot smoother) after Cleveland (1979) was performed in order to illustrate the relationship between surface roughness and maximum interface friction angles (red, solid line in Fig. 6.9a). Fitting was done using a quadratic polynomial degree and a span of 0.5. With this fit, an inflection point at a surface roughness of $Sa$    35 µm was determined. This marks the point at which the previous log-linear increase of maximum interface friction angles with surface roughness merged into the sand-to-sand shear behavior. Additionally, a significant drop in maximum interface friction angles was observed regarding the roughest surfaces (surfaces 4 and 5). The constant volume interface friction angles did not follow the same relationship observed for maximum interface friction angles. Instead, a log-linear increase in constant volume interface friction angles with surface roughness was observed without an inflection point present. Thus, the preserved surfaces (surfaces 1) generated around 70% and the air-corroded and artificial surface (surfaces 2 and 3) 80% of the constant volume friction angle determined from sand-to-sand shearing.

The constant volume interface friction angles of the adhering sand crusts (surface 4) reached the highest values with a mean of   90% compared to sand-to-sand shearing, although a larger scatter was observed. The constant volume interface friction angles of the mounted crusts (surfaces 5) dropped (in comparison with surface 4), being even more pronounced than the drop observed for maximum interface friction angles. Constant volume interface friction angles of the mounted crusts (surface 5) were more similar to those determined from the preserved surfaces (surface 1), despite having up to two magnitudes higher surface roughness. This phenomenon probably arose from the relatively large shearing gaps considered for surfaces 5, causing a non-homogeneous stress field inside the sample. The erroneous data are denoted with a black, dashed line in Fig. 6.9b and were not considered further. The remaining points can be described with good accuracy ($R^2$   0.98) by means of a half-logarithmic, linear relationship (red line in Fig. 6.9b). The sand-to-sand shear angles of the Cuxhaven Sand used as reference are given in the Tab. 6.2.
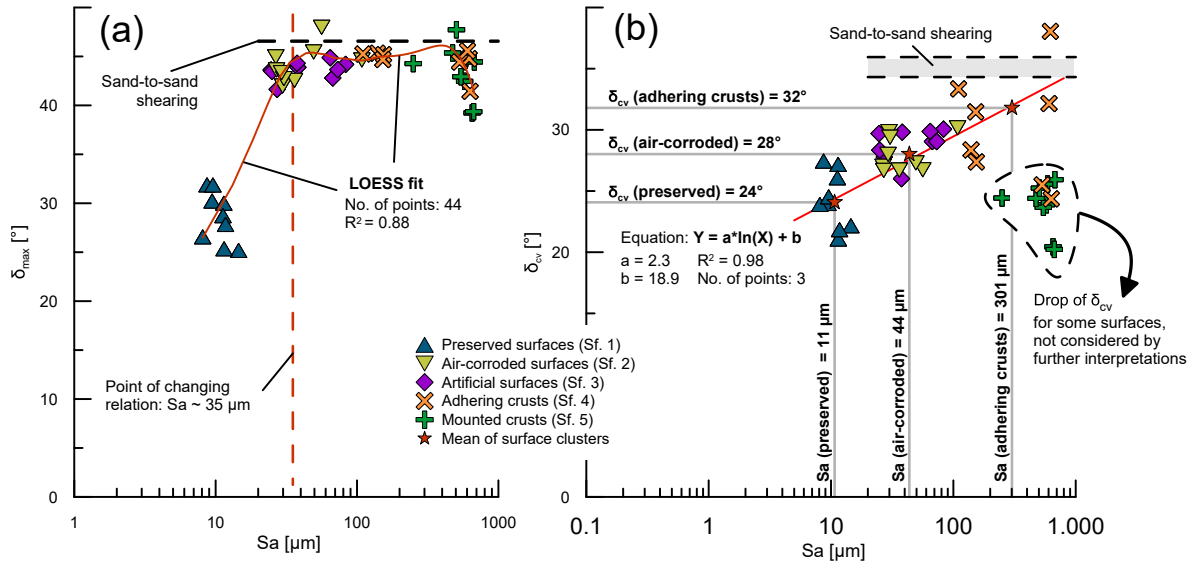


FIGURE 6.9: Friction angles vs. mean centerline surface roughnesses. **(a):** Maximum interface friction angles. **(b):** Constant volume interface friction angles and mean values (gray solid lines) used for pile capacity modeling. Gray-shaded areas represent means of sand-to-sand shearing ± 95% confidence interval.

TABLE 6.2: Results of direct sand-to-sand shear experiments on Cuxhaven Sand.

| No. | Experiment | $N$ [kN] | $max$ [kN] | $cv$ [kN] | $max$ [degree] | $cv$ [degree] |
|---|---|---|---|---|---|---|
| 1 | $SS_{1a}$ | 100 | 116 | 70 | 47 | 34 |
| 2 | $SS_{2a}$ | 200 | 215 | 120 | 47 | 34 |
| 3 | $SS_{3a}$ | 300 | 312 | 213 | 47 | 34 |
| 4 | $SS_{b1}$ | 100 | 118 | 72 | 47 | 36 |
| 5 | $SS_{b2}$ | 200 | 222 | 154 | 47 | 36 |
| 6 | $SS_{b3}$ | 300 | 305 | 214 | 47 | 36 |

### 6.5.3 Pile capacities derived from modeling

The surface roughness and interface friction parameters determined in this study were used to model the shaft shear friction along pile embedment depth (Fig. 6.10) and thus, the resulting capacities for the five corrosion scenarios (Fig. 6.5) using Eqs. 6.1 - 6.6. Parameters obtained for surfaces 3 and 5 were not considered in either of the five corrosion scenarios. Surface 3 represents the artificial surface below the sand crusts and therefore does not represent a potential corrosion stage. Surface 5 exhibited erroneous constant volume shearing behavior (Fig. 6.9). Mean values were calculated from surface roughness and interface friction angles of surfaces 1, 2, and 4 and used for further pile capacity modeling (Tab. 6.3). Modeled shaft shear stress profiles of large-diameter piles showed only small variation with respect to ICP-05 and UWA-05 approaches and the five corrosion scenarios considered (Fig. 6.10). Shear stresses were mainly controlled by the cone resistance profile used for modeling. Only corrosion scenario 5 (i.e. pile being considered to be fully covered with sand crusts) yielded significantly higher shear stresses than the other corrosion scenarios (Fig. 6.10). The modeled shaft shear stress profiles of the small-diameter piles strongly varied between corrosion scenarios (Fig. 6.10). Extremely high shear stresses would result in the part above ground water level, in case this part of the pile would be entirely covered by iron oxide sand crusts (corrosion scenario 4). For the ICP-05 model, a maximum shear stresses of 3000 kPa would be reached. The lower part below ground water level, would show similar shear stresses ( 1000 kPa) compared with those reached in corrosion scenarios 1 to 3, according to the prediction approaches. In corrosion scenario 5, the entire profile exhibited much higher pile capacities compared to scenarios 1 to 3, reaching shear stresses 3000 kPa for most of the profile considering the ICP-05 model.

TABLE 6.3: Mean surface roughnesses and shear angles for further modeling.

| Pucks | n | $\overline{Sa}$ [µm] | $cv$ [degree] |
|---|---|---|---|
| Preserved surfaces (surface 1) | 9 | 11 | 24 |
| Air-corroded surfaces (surface 2) | 9 | 44 | 28 |
| Adhering crusts (surface 4) | 8 | 301 | 32 |

All modeled large- and small-diameter pile capacities highly overestimated the measured end of driving (EoD) capacities measured in the field, when considering one

of the five corrosion scenarios (Fig. 6.11). The offset between modeled and measured pile capacities hampered direct comparison, thus, estimation of the corrosion effect on pile capacity. Therefore, this offset was corrected for both pile geometries and pile prediction approaches following Eq. 6.7.

$$Qs_{corr,x,y} \qquad Qs_{model,x,y} \qquad Qs_{model,x,y} \qquad Qs_{EoD,x} \qquad (6.7)$$

Where $Qs_{corr}$ is the offset-corrected ICP-05 or UWA-05 pile capacity modeled for one of the two pile geometries and five corrosion scenarios. Subscripts $x$ and $y$ denote different pile geometries (large- or small-diameter piles) and corrosion scenarios 1 to 5, respectively. Subscripts *model* and *EoD* denote whether pile capacities were determined from ICP-05 and UWA-05 models or from end of driving load tests in the field. Finally, the offset-corrected ICP-05 or UWA-05 pile capacities were normalized to the end of driving pile capacities measured in the field (Fig. 6.11).
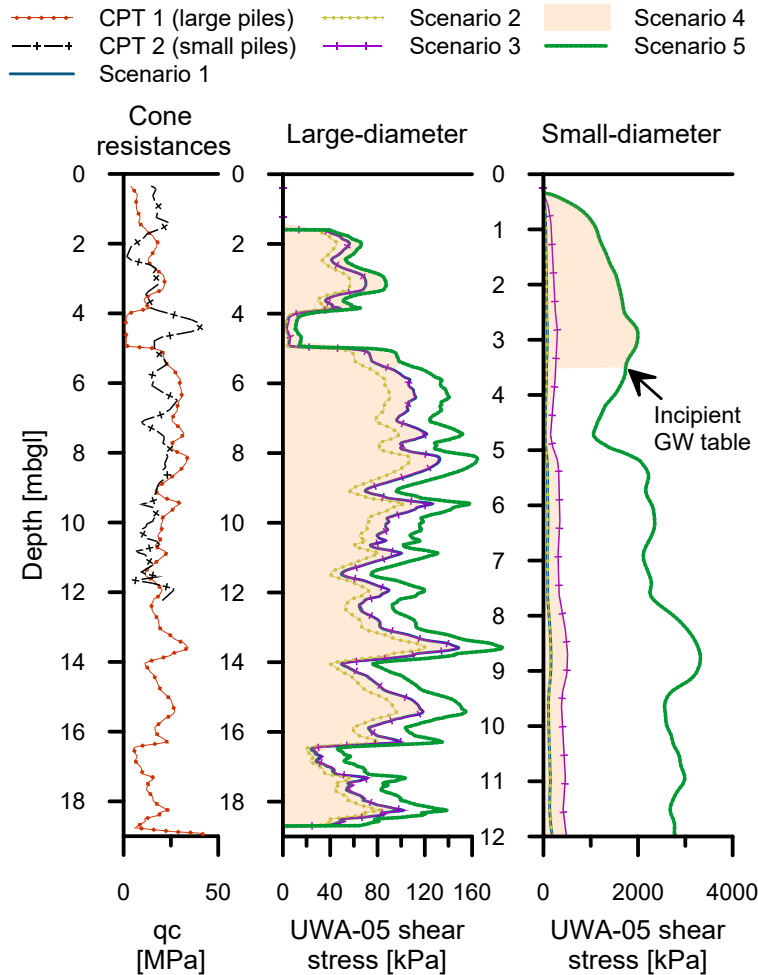


FIGURE 6.10: Cone resistance profiles and associated modelled pile capacities (i.e., shaft shear stresses) for large-diameter and small diameter piles considering five different corrosion scenarios. For clarity, only UWA-05 shear stresses are shown. More detailed representations of the shaft shear stresses are given in the supplementals (see Figs. A.3 & A.4)

For both pile geometries, the modeled pile capacities (resulting from the integrated shear stresses in Fig. 6.10 generally increased from corrosion scenarios 1 to 5. Only scenario 2, in which the entire pile was considered to comprise the surface roughness and shearing behavior of preserved steel, systematically exhibited a significantly lower capacity. The modeled corrosion scenarios highly depended on the pile diameter used. Regarding the large-diameter geometry, a capacity increase of +50% (i.e. $Qs_{corr}/Qs_{EoD}$    1.5) was modeled for scenario 5 when compared to the initial capacity. The measured capacity development in the field for the same geometry revealed a capacity increase of +240% after 1000 days of aging (see horizontal gray dashed lines in Fig. 6.11). In contrast, the small-diameter geometry, modeled for the same corrosion scenario (corrosion scenario 5), yielded an increase in capacity of +9,000% compared with those pile capacities measured shortly after end of driving. This increase exceeds by far the measured setup after 1000 days (Fig. 6.11) showing an increase of just +340%. Corrosion scenario 4, having been considered to represent field conditions most realistically, over predicted the 1000-days field capacity of the small-diameter piles by up to    460%. For the large-diameter piles instead, corrosion scenario 4 under predicted the 1000 days capacity and was just able to explain 4% of the overall increase. The pile shaft capacities modeled for each scenario, their evaluated offsets, and their final corrected shaft capacities are presented in Tab. 6.4.

TABLE 6.4: Modeled tension capacities with respect to corrosion scenarios

| Scenarios | Diameter | Method | Tension capacities [kN] | | | | |
|---|---|---|---|---|---|---|---|
| | | | 1 | 2 | 3 | 4 | 5 |
| Originals | Large | ICP-05 | 23695 | 19189 | 22917 | 23307 | 26932 |
| | | UWA-05 | 17700 | 14351 | 17798 | 18506 | 23725 |
| | Small | ICP-05 | 159 | 138 | 550 | 1212 | 4174 |
| | | UWA-05 | 120 | 105 | 414 | 842 | 2757 |
| Offsets | Large | ICP-05 | | | 14670 | | |
| | | UWA-05 | | | 8676 | | |
| | Small | ICP-05 | | | 120 | | |
| | | UWA-05 | | | 82 | | |
| Corrected | Large | ICP-05 | 9025 | 7309 | 8729 | 8878 | 10258 |
| | | UWA-05 | 9025 | 7318 | 9075 | 9436 | 12097 |
| | Small | ICP-05 | 38 | 33 | 132 | 291 | 1002 |
| | | UWA-05 | 38 | 33 | 131 | 267 | 873 |
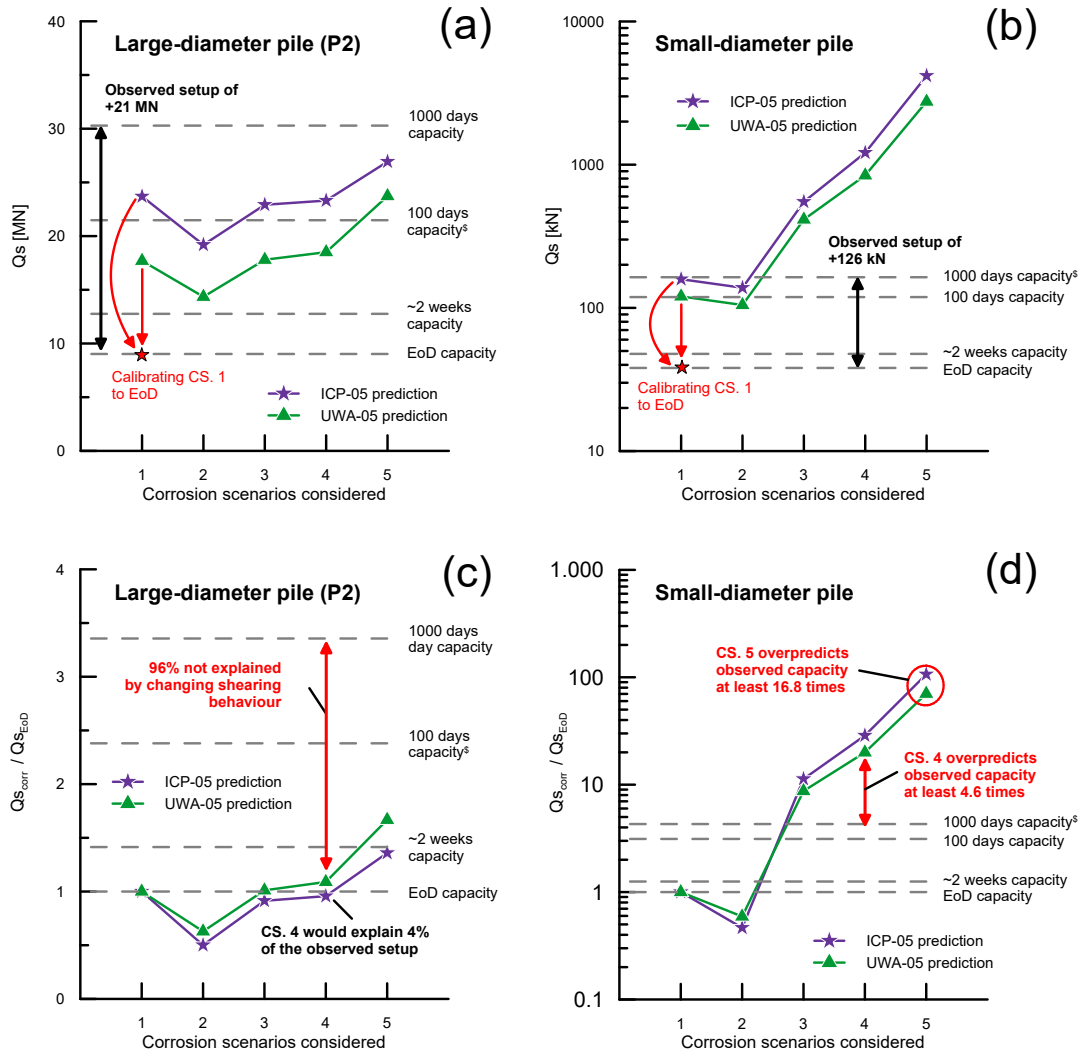
FIGURE 6.11: Comparison between modeled pile capacities (using UWA-05 and ICP-05 prediction approaches) and pile capacities measured in the field by means of the five corrosion scenarios. CS. - Corrosion scenario

## 6.6 Discussion

### 6.6.1 Relationship between shearing behavior and surface roughness

The interface shear experiments on Cuxhaven Sand revealed that the friction behavior of interfaces depends on surface roughness (Fig. 6.9a and b). The increase in maximum and constant volume interface friction angles with surface roughness has already been observed before (Kishida and Uesugi, 1987; Subba Rao, Allam, and Robinson, 1998). In order to establish compatibility with existing literature, Sa was normalized to mean grain size $D_{50}$ of the Cuxhaven Sand, whereas interface friction angles, $_{max}$ and $_{cv}$, were normalized to friction angles obtained from sand-to-sand shearing, $_{max}$ and $_{cv}$ (Figs. 6.12 and 6.13). This normalization reduced effects of grain size, relative density, grain shape, and consolidation stress between the different experiments (Kishida and Uesugi, 1987; Jardine, Lehane, and Everton, 1993; Han et al., 2018). The normalized surface roughness allowed classifying surfaces

into three categories, namely "smooth", "intermediate", and "rough". Following Paikowsky, Player, and Connors (1995), smooth surfaces commonly mobilize a constant low portion ( 30%) of the maximum and constant volume friction angles determined from sand-to-sand shearing, which is considered to be mainly caused from rolling of individual sand particles over the smooth surface (Kishida and Uesugi, 1987). Rough surfaces commonly mobilize the full maximum and constant volume friction angles determined from sand-to-sand shearing, being attributed to a complete shift of the shearing zone from the interface into the sand sample. Intermediate surfaces mobilize friction, being in between 30% and 100% of the maximum and constant volume friction angles determined from sand-to-sand shearing. Within the intermediate surfaces, interface friction angles increase linearly with normalized surface roughness (in linear-logarithmic scale). When considering normalized interface roughness values from relevant literature (Kishida and Uesugi, 1987; Porcino et al., 2003), no clear transition point between roughness categories could be found. By means of normalized surface roughness, the transitions between roughness categories appeared to vary between different sands. Following the surface categories described above, the surfaces tested in this study may be classified as intermediate (i.e. surface 1) and rough (i.e. surfaces 2 – 5) by means of their maximum interface friction angles (Fig. 6.12). The transition point between these two categories was determined at $Sa/D_{50}$ 0.175 for this study. However, when considering the constant volume interface friction angles, all surfaces were classified as intermediate because they did not completely reach sand-to-sand conditions. In case of constant volume interface friction angles (Fig. 6.13), the transition point between intermediate and rough surfaces seemed to be reached at a way higher normalized surface roughness of $Sa/D_{50}$ 6 (being estimated from the equation denoted in Fig. 6.9b) for this study. Relationships between interface friction angle and surface roughness derived for Cuxhaven Sand were compared with those derived from various quartz sands from literature (Porcino et al., 2003; Lings and Dietz, 2005; Dietz and Lings, 2006; Han et al., 2018). The sands used in the literature varied by means of particle shapes and grain size distributions (Fig. A.5 & Tab. B.5). The relationship between normalized maximum interface friction angles and normalized surface roughness of Cuxhaven Sand was compared with those relationships determined from three poorly-graded fine to coarse quartz sands (Lings and Dietz, 2005) (Fig. 6.12).

The normalized maximum interface friction angles of Cuxhaven Sand were found to be shifted towards a larger normalized surface roughness (i.e. indicating a lower maximum interface friction for the same surface roughness) when compared to the three sands from the literature. A shift of the intermediate zone to rougher normalized surfaces has not been observed in other experiments before, regarding the maximum interface friction angle. The relationship between normalized constant volume interface friction angles and normalized surface roughness of Cuxhaven Sand was compared with those determined from various poorly-graded fine to coarse sands and one well-graded coarse sand (Porcino et al., 2003; Dietz and Lings, 2006; Han et al., 2018) (Fig. 6.13). Similar to the maximum state (Fig. 6.12), the normalized constant volume interface friction angles of Cuxhaven Sand were observed to be shifted towards higher surface roughness. This implies that Cuxhaven Sand behave differently compared to sands from literature, with regard to their sand-to-sand- and likely also their interface shearing behavior. The offset between the interface friction – surface roughness relationships between Cuxhaven Sand and sands from literature indicates the existence, of an additional influencing factor, not affected by
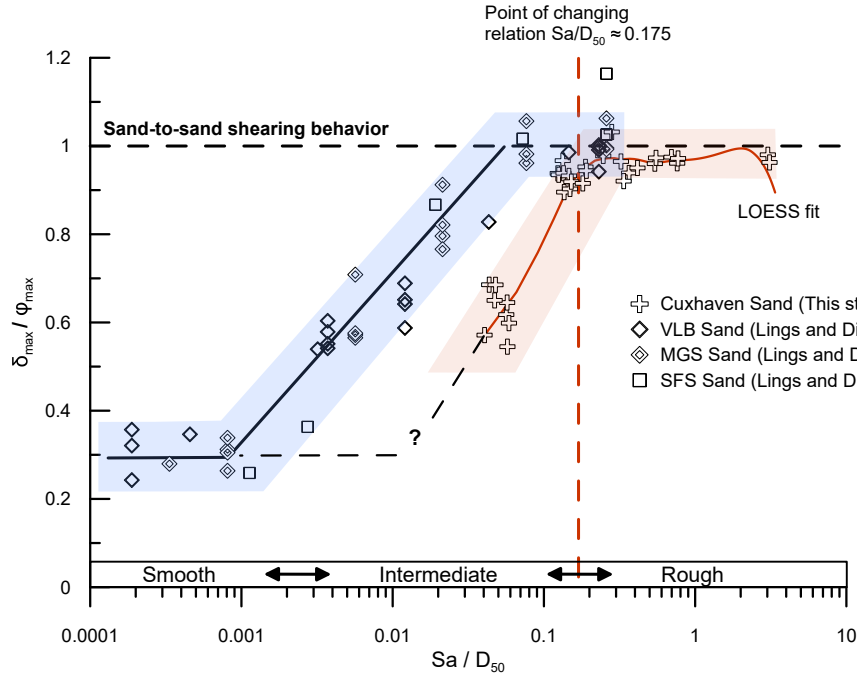
FIGURE 6.12: Normalized maximum interface friction angles vs. normalized surface roughness of Cuxhaven Sand compared with different poorly-graded sands from the literature.
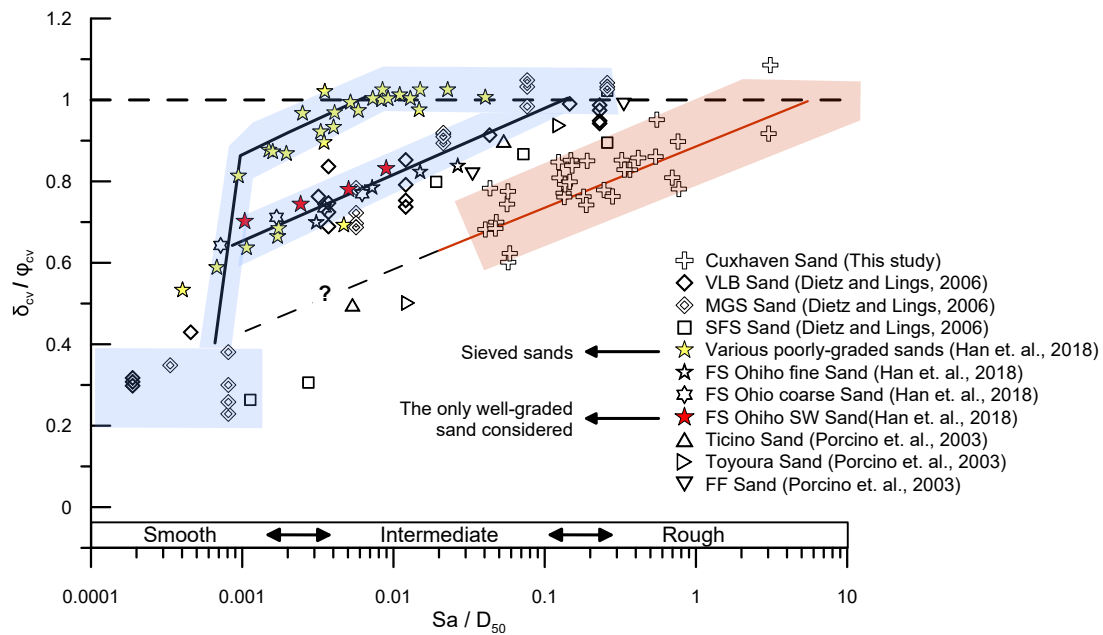


FIGURE 6.13: Normalized constant volume interface friction angles vs. normalized surface roughness of Cuxhaven Sand compared with different poorly-graded and well-graded sands from the literature.

normalization. An observation firstly made by Han et al. (2018) for the constant volume state. The authors postulated that the observed shift was caused by the increase in gradation between their artificially sieved sands (marked as yellow stars in Fig. 6.13) and their natural, but also poorly-graded sands (unfilled stars in Fig. 6.13). The

smaller particles present in the natural sands should facilitate rolling and shearing of larger particles, lowering the overall friction response (Han et al., 2018). However, some data from literature do contradict this explanation. The SFS Sand tested by Lings and Dietz (2005) and the FF Sand tested by Porcino et al. (2003) provide the highest fines contents (Fig. A.5), but similar interface shearing behaviors than the natural sands of Han et al. (2018) (Fig. 6.13). The only well-graded sand after the Unified Soil Classification System (USCS) (Fig. B.5), named SF Ohio SW Sand and denoted by red stars in Fig. 6.13, generated intermediate normalized friction angles compared with the other sands considered (when considering the same normalized interface roughness), clearly contradicting the postulation of Han et al. (2018). Several processes may explain why the relationships between interface friction angles (for maximum and constant volume states) were shifted towards a larger normalized surface roughness:

(1) The methods to determine interface friction angles and surface roughness differed systematically between our and other studies. For example, the dimensions or type of the shear apparatus (direct or ring shear), the width of the shearing gap, the displacement interval at which the constant volume friction angle was determined, and the displacement rate are potential factors influencing friction behavior. Lings and Dietz (2005) used displacement rates being more than two times higher than in the present study ($\dot{s}$ 1.2 $mm/min$ instead of $\dot{s}$ 0.5 $mm/min$). It is also conceivable, that the rather simple roughness parameter $R_{CLA}$ (widely used in the literature considered) may not be suitable after all to fully describe the roughness of a surface and the resulting shear properties.

(2) In our study, natural surfaces from steel piles and adhering sand crusts were sheared (which was never done before), whereas all sands from literature were sheared over artificial surfaces like sandpaper, exhibiting a much more homogeneous roughness distribution. The corrosion products on our steel surface and in our sand crusts may have lowered the corresponding interface friction angles to some extent.

(3) Particle breakage due to shear could possibly explain the lower normalized interface friction angles at a higher surface roughness. Particle breakage would artificially change the gradation of the sand, thus, the process described by Han et al. (2018), that smaller particles would then facilitate the rolling of larger particles, would take place. However, the sands considered in this literature comparison are all hard-grained and are likely non-crushable within the stresses applied during the shear experiments.

(4) Interface clogging effects like described by Martinez and Frost (2017), may also influence the results. More direct shear experiments, using a wider spectrum of soils (e.g. fine grained soils, crushable soils) and surfaces (i.e. natural as well as artificial surfaces), are necessary to better understand the relationship between surface roughness and interface friction angles.

### 6.6.2   Modeling of corrosion effects

Our modeled large- and small-diameter pile capacities highly overestimated the initial pile capacities measured in the field shortly after end of driving for all five corrosion scenarios considered. This is not surprising, since the ICP-05 and UWA-05

prediction models were not calibrated to the very dense subsoil conditions encountered at our test site near Cuxhaven, Germany. Additionally, both capacity prediction models are based on pile datasets that mainly comprise pile capacities measured a few days after their installation. As a result, a small pile setup may have already been included in both capacity prediction models. We were able to overcome these uncertainties by using the offset-corrected pile capacity $Qs_{corr}$ (Eq. 6.7, Tab. 6.4). Furthermore, our study provided evidence that corrosion-related changes in surface roughness and friction behavior provide a theoretical capability for significant capacity gains. Just slight increases in surface roughness highly increased the resulting interface friction angles, thus, the capacity of some piles (Fig. 6.11). Our evidence thus support observations made previously from field studies (Lehane et al., 2012; Carroll et al., 2017; Carroll et al., 2019; Gavin and Igoe, 2019, or Chapter 4) and chamber experiments (White and Zhao, 2006), who also referred their observed setups largely or solely to corrosion and the formation of sand crusts. On the other hand, our evidence contradicts findings of Gavin et al. (2015) who suggested that an increase of the interface friction angles up to sand-to-sand behavior (due to corrosion), might never result in significant capacity gains, independent of the considered pile size. We suggest that the influence of corrosion, or more generally the possibility of a pile surface to change over time, should more significantly be (re-)considered as contributor to pile setup. Even for piles, such as wooden or concrete piles, for which corrosion does not play a significant role, other processes may change their surfaces over time when being in contact with saturated or partial saturated soil. For example, the decay of wooden piles and deterioration of reinforced concrete piles might lower their inner stability, but also increase their outer surface roughness after some time, thus, resulting in (short term) capacity gains. Chow et al. (1998) postulated that corrosion and/or physio-chemical processes affecting the pile mantle over time are likely to be one of the three major factors causing the pile setup. This statement is formulated broadly enough so that any effect with positive impact on surface roughness of the pile is covered. Therefore, the frequently used argument against corrosion as a major process affecting pile setup – that setup can be observed for wooden and concrete piles (Gavin et al., 2015) – thus becomes questionable. Corrosion in the form of iron oxidation is likely to be the most common cause of such a change in surface roughness but should not be considered as a mandatory criterion. Additionally, our study demonstrated that the ICP-05 and UWA-05 models are in principle able to predict the pile capacity change due to a change in surface roughness (e.g. corrosion), but that this prediction includes a high level of uncertainty. The effect of corrosion scenarios was found to be extraordinarily sensitive to the pile diameter (Fig. 6.11). The pile diameter $D$ is an important parameter in the calculation of the dilative stress component $_{rd}$ (Eq. 6.3), thus, leading to neglectable shaft shear stress gains for large-diameter piles and unreasonably high shaft shear stresses for small-diameter piles (Figs. 6.10. Even if this sensitivity to the pile diameter is justified for small-diameter piles to a certain degree, it seems to be too high in comparison with the pile setup observed in the field. The pile diameter is used inversely in Eq. 6.3 proposed by Lehane et al. (1993), which has already been argued by others (e.g. Zhang and Wang, 2015) to be responsible for the high sensitivity in capacity prediction. In order to calibrate this equation unambiguously, data must be available that allow the corrosion proportion to be clearly separated from other setup influencing factors, such as stress relaxation (Lim and Lehane, 2014). Since these experiments require a high technical effort, data in this respect are rather scarce. However, the field experiment at Chapter 4 reveals, corrosion and/or physio-chemical processes are responsible for up to 90% of the overall proportion of the setup for small-diameter

piles. Field and lab observations as presented by this study may be used to further calibrate existing pile capacity prediction models. By improving the existing and well-working mechanical models, like those of ICP-05 and UWA-05, the possibility might be given in the future to better estimate the corrosion-related proportion of the pile setup. Engineering practice could highly benefit from such models because the appearance of corrosion seems to be more easily predictable compared to other mechanisms contributing to setup (e.g. stress equilibration).

## 6.7   Conclusion

In this study, we sampled steel and sand crust surfaces from a large-diameter, open-ended steel monopile having been aged for four years in very dense natural sand deposits. Surface roughness measurements and direct interface friction experiments were performed in order to quantify the proportion of corrosion on interface friction angles and, thus, on pile capacity predictions. Two different pile diameters were considered. The following conclusions were made.

- The surface roughness of steel piles increased with progressive stages of corrosion (i.e. preserved surfaces, air-corroded surfaces, sand crusts).

- The interface friction angles of corroded surfaces strongly correlated with surface roughness.

- Our surfaces exhibited lower normalized maximum and constant volume friction angles compared with other experimental data from the literature. This phenomenon might be a result of the naturally corroded steel surfaces and sand crusts sheared in our study.

- All model pile capacities using the ICP-05 and UWA-05 approach with one of five corrosion scenarios overestimated the measured pile capacities installed in the field.

- A strongly varying sensitivity of the modeled pile capacity to corrosion-related changes in surface roughness and shearing behavior was recognized for the two different pile diameters considered.

- For large-diameter piles the prediction models were just able to explain 4% of the setup observed in the field using the most reasonable corrosion scenario. For small-diameter piles instead, the models overestimated by far the capacities measured in the field.

## 6.8   Acknowledgments

# Chapter 7

# Conclusion - the principles of the axial pile setup

The doctoral thesis at hand contributed to the understanding of the setup as a multi-factorial and multidimensional process. Initial pile capacities and their temporal evolution (setup) are investigated in two independent field studies concerning small- and large- (Chapter 4 and 5) diameter piles. The importance of the installation method effecting the initial capacity as well as their setup- behavior could be demonstrated. A third study targets the friction behavior of a continuously corroding pile shaft and investigates its potential contribution to the setup in general (Chaper 6). The following section summarizes the findings with regards to the research hypotheses defined in Chapter 2.9.

In addition to research hypothesis 1, we could reveal that the $N_{bA}$ value is a suitable parameter to account for soil disturbances induced during pile installation. A more disturbing installation method – resulting in higher $N_{bA}$ values – would result in a reduced initial capacity but simultaneously in a more pronounced setup. In our experiment, the vibratory pile driving method caused the highest $N_{bA}$ values, led to the lowest initial pile capacities (Fig. 4.7C) and to the highest relative setup rates (Fig. 4.8, lower part). Vibrated piles reached an equal capacity as impact driven piles after only 100 days of aging. In addition, they showed a clear tendency to outperform the impact driven piles in the near future due to their increased setup rates. Research hypothesis 1 is thus confirmed. However, the deviating capacity development of the stainless steel piles (Fig. 4.8) indicates, that the stress equilibration – caused by the previously induced soil disturbances and driven by friction fatigue after Lim and Lehane (2014) – is superimposed with an also time-dependent corrosion effect. Therefore, the $N_{bA}$-value only encodes the extend of the effect, but not its individual root cause. A clear quantification of the contribution of stress equilibrium and corrosion to the overall setup could not be achieved.

The evaluation of a capacity monitoring of six large-diameter piles revealed, that vibratory driven, large-diameter piles exhibit only 31% the axial capacity of an impact driven equivalent, even after three years of aging (Fig. 5.8). The setup -behavior of these large-diameter piles contradicts our previous assumptions that were based on the small-diameters setup trends. Additionally, also our research hypothesis 2 has to be rejected. The installation of offshore-size diameter piles through vibratory driving might cause a more profound disturbance of the soil, but does no longer result equally in a setup more pronounced to what has been shown for its impact driven equivalents. Otherwise, the capacity gap between piles driven by either impact or vibratory driving would be less severe (Fig. 5.8). Unfortunately, due to the missing initial capacities of the vibrated large-diameter piles, no additional precise

conclusions can be drawn at this point.

The findings of the final study (Chapter 6) reveals, that the corrosion of the pile mantle and the related incrustations lead to a strong increase in pile surface roughness (Fig. 6.8). As a result, also the shear resistance increases (Fig. 6.10) and lead to dramatic, principal increase in pile capacities (Fig. 6.11b and d). With respect to the modeled pile diameter, this dramatic increase could be confirmed for small-diameter piles, but must be rejected if the pile diameter reaches offshore dimensions (Fig. 6.11c and d). The reliability of the used models and their diameter dependency has been discussed critically. Thus, hypothesis 3 can only partially be confirmed.

With the help of these combined information and the deeper insight provided by previous studies, I would like to draw a rough picture of the setup effect and its principles as understood by me (Fig. 7.1).
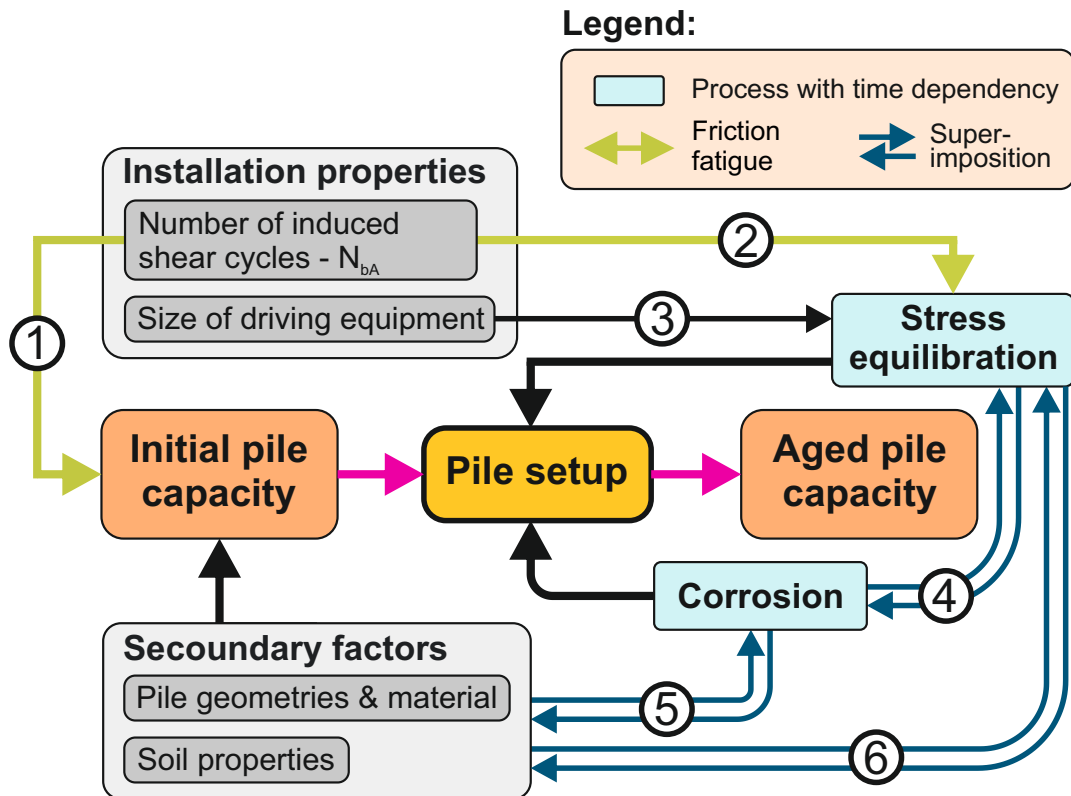


FIGURE 7.1: The axial pile setup and its principles as elaborated by this dissertation.

Looking at the setup effect from the perspective of Lim and Lehane (2014), the installation method of a pile is crucial as it defines the piles initial capacity and its subsequent setup behavior. By increasing the number of cycles during installation $N_{bA}$, the surrounding soil is progressively disturbed by friction fatigue effects. Its ability to transmit lateral stresses is hampered and thus, the initial pile capacity is reduced (process (1) at Fig. 7.1). Simultaneously, the potential for a strong setup is provided – As the extend of soil disturbance increases, the potential for a capacity increase rises (process (2) at Fig. 7.1; see Fig. 4.9). However, if the level of soil

disturbance exceeds a critical threshold, the equilibration of stresses either fail entirely or took to long that it appears to become negligible (Fig. 5.8). The size of the pile driving equipment is included as a setup influencing factor (process (3) at Fig. 7.1). Furthermore, this size related soil and stress disturbance should have a different effect than the kind of disturbance dominated by friction fatigue effects. Thus, this kind of disturbances is not longer encoded via the $N_{bA}$ value. Another parameter to quantify the size-effects associated disturbance is needed. Apart from these size-dependent disturbance, other processes like corrosion alter the surface of a pile and interact with the ongoing, equilibrating stress field (process (4) at Fig. 7.1). If corrosion can mostly be neglected (e.g. for stainless steel piles), the stress equilibration with all the associated sub-mechanisms (increase in stiffness and lateral acting stress) will exclusively occur as previously suggested by Lim and Lehane (2014).
If instead, the pile is prone to corrosion – not necessarily limited to iron oxidation – corrosion directly affects the mobilized shaft shear stresses (Fig. 6.11) and unfold its positive impact on the pile capacity more promptly and more effective as less disturbed the soil remained after pile installation. For an identical degree of corrosion, jacked piles are expected to show an earlier capacity gain than its impact driven or vibrated equivalents (jacked piles at Fig. 4.8). If the soil around the pile is heavily disturbed instead – after being subjected to a high $N_{bA}$ number during installation or, alternatively, due to the size effect of the driving equipments – this corrosion will have no consequence for the beginning. Only when the equilibration of the stress field reaches a certain level, the changes on the pile surface would reveal their effect on pile capacity. This would result in a delayed setup. However, since corrosion and stress equilibration simultaneously start to reveal their impacts at this point, a particular strong setup could be established for a limited period of time. It is likely, that, e.g. after a completed incrustation – which might already be established after moderate aging periods – the strong setup would be considerably weakened.

Relative density as secondary, setup influencing factor is likely to interact mainly with corrosion (process (5) at Fig. 7.1). Even in case of a pile installation with close to no disturbance (e.g. by pile jacking), incipient corrosion in a dense soil can lead to considerable capacity gains (see e.g. Figs. 4.11 and 4.12). Since almost no setup occurs for piles in loose soils that are subjected to an identical less disturbing installation procedure – although corrosion can be indirectly confirmed – the influence of corrosion seems to be minimalized with a more loose soil packing. Conversely, stress equilibration effects should be much more unambiguous in these cases, revealing a more unbiased relationship to $N_{bA}$ and friction fatigue (process (6) at Fig. 7.1). A final elucidation of the impact of all mechanisms and, above all, an accurate breakdown of the overall acting setup into its stress equilibration and corrosion proportion could only be achieved by directly measuring the temporal evolution of the stress field around a driven pile. Such measurements are extremely difficult to perform, but could be realized. This thesis expands the state of knowledge regarding the important pile installation related setup effect and discusses, how various related effects and processes have to be considered. The findings are ultimately summarized in Figure 7.1. Future studies should aim for testing and potentially confirming these relations.

# Appendix A

# Supplemental figures
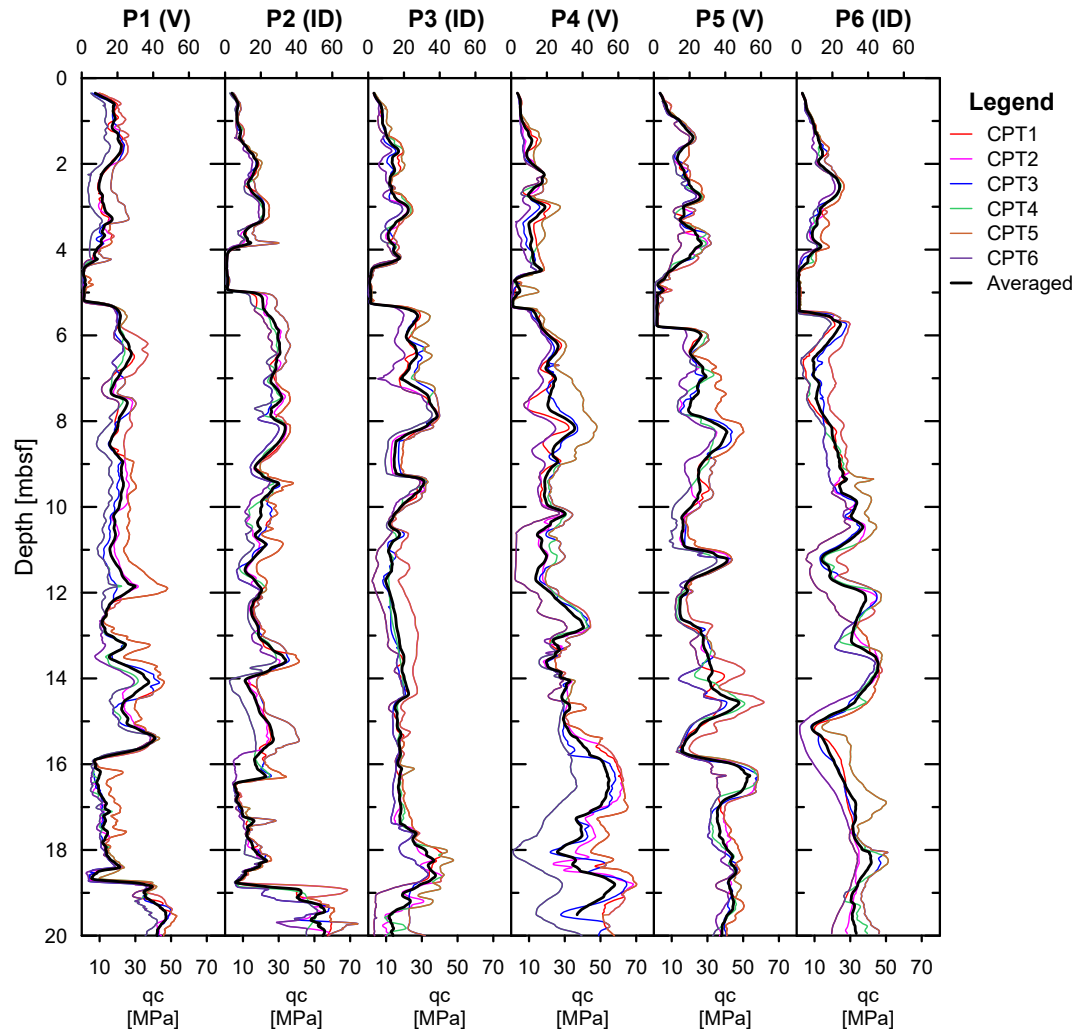
FIGURE A.1: CPT profiles for each large-diameter pile locations -
Chapter 5.
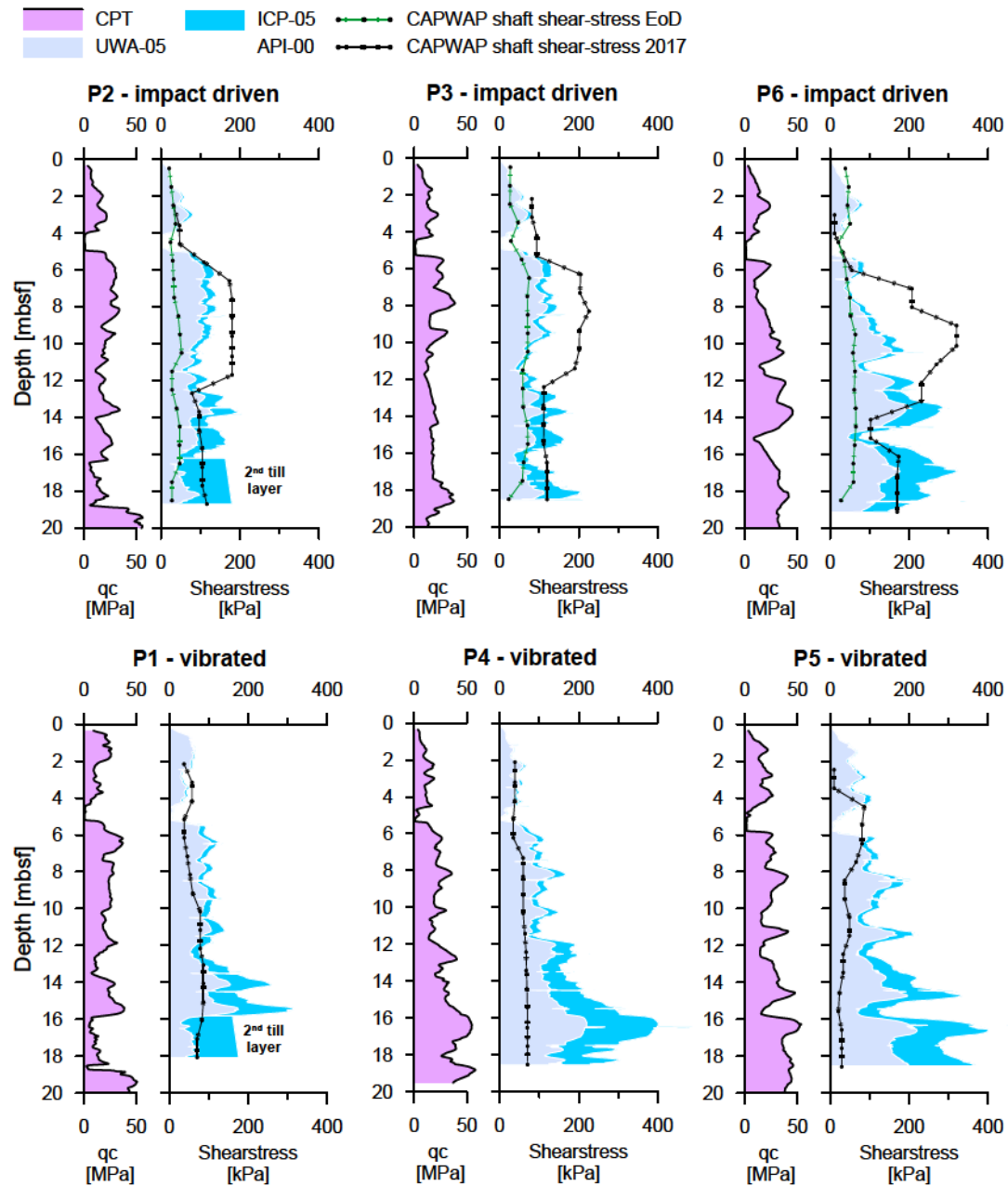
FIGURE A.2: Comparison of ICP-05 and UWA-05 predicted to calculated shaft shear-stresses - Chapter 5.
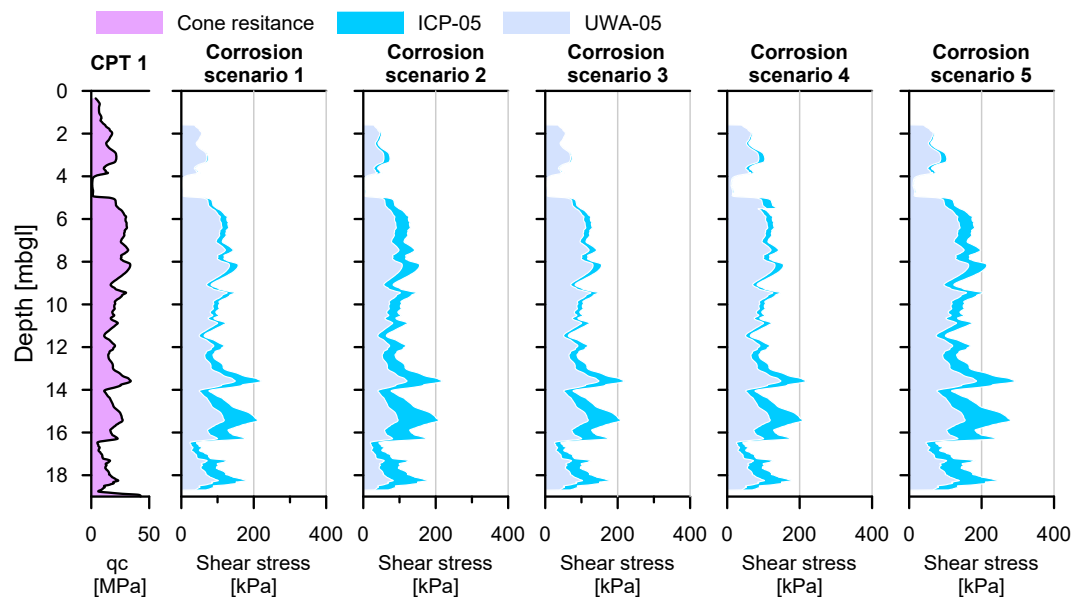
FIGURE A.3: Modeled UWA-05 and ICP-05 pile capacities (i.e. shaft shear stresses) for large-diameter piles regarding five different corrosion scenarios - Chapter 6.
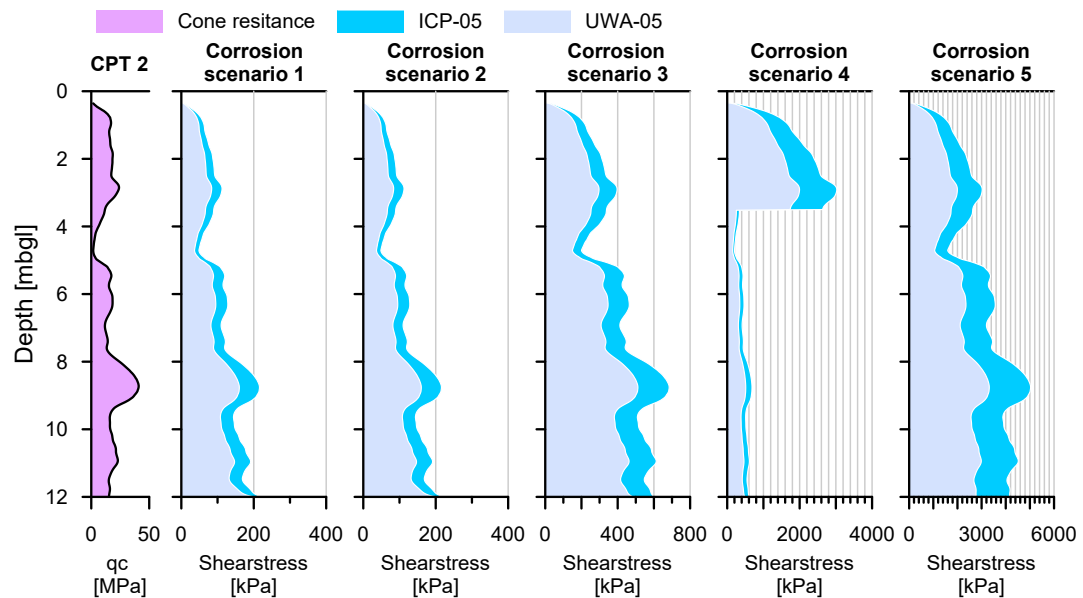


FIGURE A.4: Modeled UWA-05 and ICP-05 pile capacities (i.e. shaft shear stresses) for small-diameter piles regarding five different corrosion scenarios - Chapter 6.
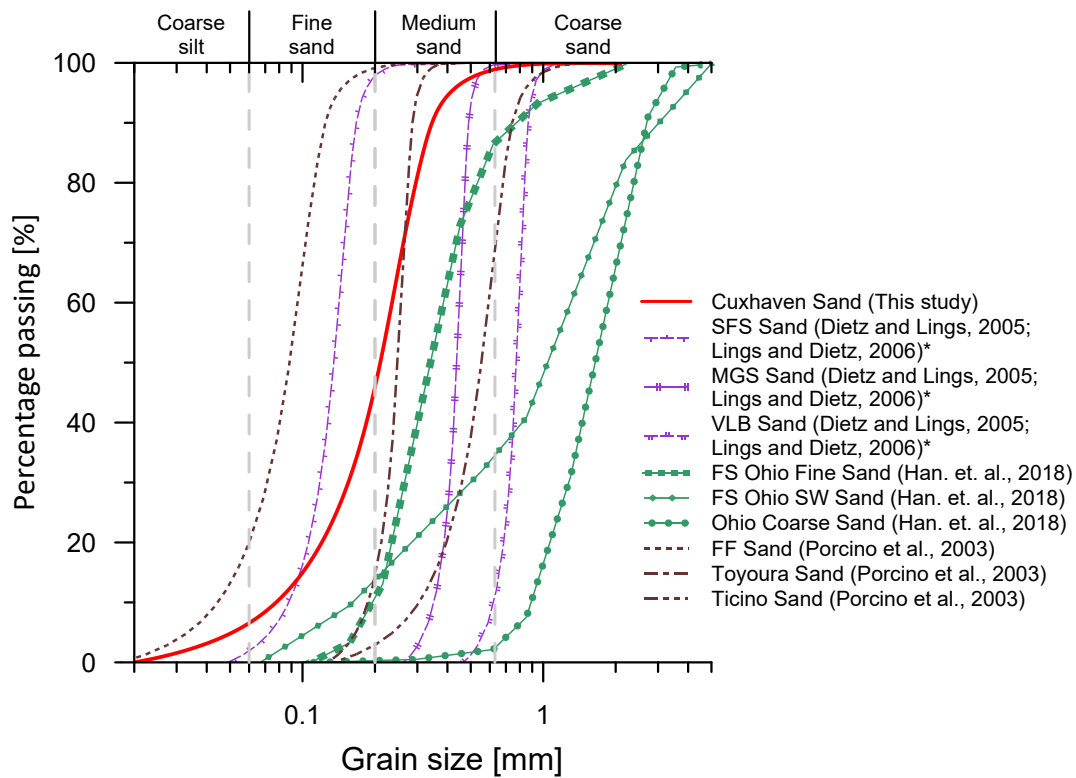
FIGURE A.5: Grain size distribution curves of Cuxhaven Sand and sands used for literature comparison. Curves marked with an asterisk in the legend were estimated from $D_{10}$, $D_{50}$ and $D_{60}$ values due to limited information in the primary literature - Chapter 6.

# Appendix B

# Supplemental data

## B.1 Evaluated - supplemental data

TABLE B.1: Pile properties and shear stresses out of SPT and Chapter 4. A - averaged shear stress 24 hours after driving; B - time after EoD; C - averaged mantle shear stress after aging; D - calculated UWA-05 averaged mantle shear stress for pile location; E - initial averaged mantle shear stress (A) normalized by its expected UWA-05 – shear stress (D) ; F - averaged mantle shear stress after aging time (B) normalized by its UWA-05 shear-stress expectation (D); G - number of shear cycles per m2 of effective pile mantle area; L - setup ratio (C divided by A).

| | No. | Pile ID | Ma. | Leff [m] | A [kPa] | B [d] | C [kPa] | D [kPa] | E - | F - | G [m $^2$] | L - |
|---|---|---|---|---|---|---|---|---|---|---|---|---|
| Impact driving | 1 | ID-m-100-1 | m | 11.80 | 24.7 | 104.1 | 67.7 | 201.4 | 0.12 | 0.34 | 590 | 2.74 |
| | 2 | ID-m-100-3 | m | 11.55 | 33.4 | 104.1 | 115.9 | 198.3 | 0.17 | 0.58 | 654 | 3.47 |
| | 3 | ID-m-100-4 | m | 11.60 | 27.0 | 97.2 | 96.0 | 191.3 | 0.14 | 0.50 | 593 | 3.56 |
| | 4 | ID-m-10-1 | m | 11.70 | 42.8 | 13.0 | 52.5 | 209.2 | 0.20 | 0.25 | 801 | 1.23 |
| | 5 | ID-m-10-2 | m | 11.80 | 27.0 | 13.0 | 34.8 | 199.1 | 0.14 | 0.17 | 624 | 1.29 |
| | 6 | ID-m-10-3 | m | 11.55 | 25.3 | 13.0 | 24.3 | 195.9 | 0.13 | 0.12 | 672 | 0.96 |
| | 7 | ID-m-1-2 | m | 11.70 | 26.8 | 0.9 | 28.6 | 199.1 | 0.13 | 0.14 | 691 | 1.07 |
| | 8 | ID-m-1-4 | m | 11.60 | 31.4 | 1.0 | 31.7 | 203.0 | 0.15 | 0.16 | 749 | 1.01 |
| | 9 | ID-m-1-6 | m | 11.78 | 28.6 | 1.0 | 29.2 | 192.8 | 0.15 | 0.15 | 648 | 1.02 |
| | 10 | ID-s-100-1 | s | 11.52 | 26.5 | 98.0 | 31.3 | 171.0 | 0.15 | 0.18 | 648 | 1.18 |
| | 11 | ID-s-100-2 | s | 11.70 | 23.8 | 98.0 | 25.9 | 169.4 | 0.14 | 0.15 | 557 | 1.09 |
| | 12 | ID-s-100-3 | s | 11.85 | 24.6 | 98.1 | 31.1 | 172.5 | 0.14 | 0.18 | 551 | 1.26 |
| | 13 | ID-s-10-3 | s | 11.75 | 32.8 | 9.9 | 28.0 | 170.2 | 0.19 | 0.16 | 646 | 0.85 |
| | 14 | ID-s-10-6 | s | 11.60 | 27.7 | 11.0 | 26.5 | 164.7 | 0.17 | 0.16 | 635 | 0.95 |
| | 15 | ID-s-10-7 | s | 11.40 | 27.5 | 11.0 | 28.5 | 168.6 | 0.16 | 0.17 | 604 | 1.04 |
| | 16 | ID-s-1-3 | s | 11.80 | 24.8 | 1.0 | 24.4 | 173.3 | 0.14 | 0.14 | 592 | 0.98 |
| | 17 | ID-s-1-6 | s | 11.68 | 25.8 | 0.9 | 26.9 | 173.3 | 0.15 | 0.16 | 617 | 1.04 |
| | 18 | ID-s-1-7 | s | 11.70 | 21.5 | 1.0 | 22.1 | 169.4 | 0.13 | 0.13 | 503 | 1.03 |
| Pile jacking | 19 | J-100-1 | m | 11.70 | 80.7 | 101.9 | 213.8 | 200.6 | 0.40 | 1.07 | 8 | 2.65 |
| | 20 | J-100-2 | m | 11.80 | 91.2 | 105.1 | 223.5 | 203.0 | 0.45 | 1.10 | 9 | 2.45 |
| | 21 | J-100-3 | m | 11.65 | 66.0 | 102.1 | 199.7 | 199.8 | 0.33 | 1.00 | 15 | 3.02 |
| | 22 | J-10-3 | m | 10.75 | 119.0 | 9.9 | 168.8 | 194.4 | 0.61 | 0.87 | 10 | 1.42 |
| | 23 | J-10-4 | m | 11.50 | 88.4 | 9.9 | 146.2 | 197.5 | 0.45 | 0.74 | 9 | 1.65 |
| | 24 | J-10-5 | m | 11.30 | 98.4 | 10.0 | 145.5 | 197.5 | 0.50 | 0.74 | 15 | 1.48 |
| | 25 | J-1-1 | m | 11.77 | 86.8 | 1.0 | 87.9 | 192.0 | 0.45 | 0.46 | 8 | 1.01 |
| | 26 | J-1-2 | m | 11.72 | 92.4 | 1.0 | 96.2 | 196.7 | 0.47 | 0.49 | 9 | 1.04 |
| | 27 | J-1-3 | m | 11.95 | 77.1 | 1.0 | 79.4 | 198.3 | 0.39 | 0.40 | 10 | 1.03 |
| Vibratory pile driving Vcss1 | 28 | Vcss1-100-1 | m | 11.60 | 16.8 | 109.9 | 86.2 | 199.1 | 0.08 | 0.43 | 11792 | 5.13 |
| | 29 | Vcss1-100-2 | m | 11.65 | 35.4 | 110.0 | 108.6 | 206.1 | 0.17 | 0.53 | 11515 | 3.07 |
| | 30 | Vcss1-100-3 | m | 11.70 | 16.4 | 109.0 | 78.1 | 195.9 | 0.08 | 0.40 | 11543 | 4.76 |
| | 31 | Vcss1-10-1 | m | 11.85 | 23.1 | 10.0 | 23.4 | 196.7 | 0.12 | 0.12 | 9095 | 1.01 |
| | 32 | Vcss1-10-3 | m | 11.70 | 21.1 | 9.8 | 33.5 | 194.4 | 0.11 | 0.17 | 9095 | 1.59 |
| | 33 | Vcss1-1-1 | m | 11.68 | 42.8 | 1.0 | 42.3 | 203.0 | 0.21 | 0.21 | 10263 | 0.99 |
| | 34 | Vcss1-1-2 | m | 11.74 | 39.9 | 1.0 | 40.4 | 194.4 | 0.21 | 0.21 | 10257 | 1.01 |
| | 35 | Vcss1-1-3 | m | 11.80 | 26.2 | 1.1 | 28.3 | 199.8 | 0.13 | 0.14 | 9095 | 1.08 |
| Vibratory pile driving Vcss2 | 36 | Vcss2-100-2 | m | 8.70 | 54.9 | 95.0 | 138.4 | 205.3 | 0.27 | 0.67 | 4495 | 2.52 |
| | 37 | Vcss2-100-3 | m | 11.70 | 13.9 | 93.9 | 76.9 | 197.5 | 0.07 | 0.39 | 5808 | 5.54 |
| | 38 | Vcss2-100-4 | m | 11.80 | 16.1 | 95.1 | 95.7 | 199.1 | 0.08 | 0.48 | 5800 | 5.96 |
| | 39 | Vcss2-10-1 | m | 11.95 | 46.5 | 9.2 | 55.3 | 205.3 | 0.23 | 0.27 | 4547 | 1.19 |
| | 40 | Vcss2-10-2 | m | 11.78 | 36.9 | 9.0 | 49.4 | 205.3 | 0.18 | 0.24 | 6856 | 1.34 |
| | 41 | Vcss2-10-3 | m | 11.74 | 47.4 | 10.0 | 55.0 | 193.6 | 0.24 | 0.28 | 4547 | 1.16 |
| | 42 | Vcss2-1-1 | m | 11.80 | 18.1 | 0.9 | 21.4 | 194.4 | 0.09 | 0.11 | 5784 | 1.19 |
| | 43 | Vcss2-1-2 | m | 11.70 | 43.9 | 0.9 | 44.9 | 195.2 | 0.22 | 0.23 | 6428 | 1.02 |
| | 44 | Vcss2-1-3 | m | 11.75 | 15.5 | 0.9 | 19.3 | 199.1 | 0.08 | 0.10 | 5770 | 1.24 |

Ma. - used pile material; m - mild steel; s - stainless steel; Pile Vcss1-10-2 was not tested due to problems during pile installation.

TABLE B.2: Comparable pile setup data from other studies - Chapter 4. A - test location; B - pile installation method; C - pile material; D - pile tip condition; E - pile outer diameter; F - wall thickness; G - pile embedment length; L - averaged cone resistance for test location; M - plug length ratio; N - $N_{bA}$ number; O - time after $t0$ (aging time); P - averaged pile shaft shear stress; Q - averaged shear stress prediction after UWA-05; R - setup ratio $R_{set}$ after Eq. 4.5

| No. | A | B | C | D | E [mm] | F [mm] | G [m] | L [MPa] | M [-] | N [$m^2$] | O [d] | P [kPa] | Q [kPa] | R [-] |
|---|---|---|---|---|---|---|---|---|---|---|---|---|---|---|
| 1 | SP | ID | m | OE | 88.9 | 2.6 | 4 | 6 | 0.8 | 1470 | 4 | 16 | 46 | |
| 2 | SP | ID | m | OE | 88.9 | 2.6 | 4 | 6 | 0.8 | 1470 | 376 | 59 | 46 | 3.69 |
| 3 | SP | ID | m | OE | 88.9 | 2.6 | 2.5 | 3 | 0.6 | 437 | 5 | 16 | 33 | |
| 4 | SP | ID | m | OE | 88.9 | 2.6 | 2.5 | 3 | 0.6 | 437 | 259 | 58 | 33 | 3.63 |
| 5 | SP | ID | m | OE | 88.9 | 5 | 4 | 6 | 0.8 | 1647 | 3 | 23 | 45 | |
| 6 | SP | ID | m | OE | 88.9 | 5 | 4 | 6 | 0.8 | 1647 | 374 | 77 | 45 | 3.35 |
| 7 | SP | ID | m | OE | 114.3 | 3.2 | 4 | 6 | 0.9 | 1274 | 3 | 20 | 39 | |
| 8 | SP | ID | m | OE | 114.3 | 3.2 | 4 | 6 | 0.9 | 1274 | 374 | 60 | 39 | 3 |
| 9 | SP | ID | m | OE | 88.9 | 3.2 | 4 | 6 | 0.8 | 1330 | 3 | 26 | 44 | |
| 10 | SP | ID | m | OE | 88.9 | 3.2 | 4 | 6 | 0.8 | 1330 | 374 | 77 | 44 | 2.96 |
| 11 | SP | ID | m | CE | 88.9 | 5 | 4 | 6 | 0 | 3888 | 4 | 7 | 55 | |
| 12 | SP | ID | m | CE | 88.9 | 5 | 4 | 6 | 0 | 3888 | 375 | 79 | 55 | 11.29 |
| 13 | SP | ID | m | CE | 88.9 | 2.6 | 2.5 | 3 | 0 | 646 | 5 | 7 | 34 | |
| 14 | SP | ID | m | CE | 88.9 | 2.6 | 2.5 | 3 | 0 | 646 | 259 | 59 | 34 | 8.43 |
| 15 | SP | J | m | CE | 101.5 | — | 3.72 | 5 | 0 | 13 | 1 | 46 | 45 | |
| 16 | SP | J | m | CE | 101.5 | — | 3.1 | 5 | 0 | 31 | 72 | 48 | 44 | 1.04 |
| 17 | SP | J | m | CE | 65 | — | 3.14 | 4 | 0 | 48 | 1 | 46 | 46 | |
| 18 | SP | J | m | CE | 65 | — | 3.1 | 5 | 0 | 49 | 70 | 56 | 53 | 1.22 |
| 19 | SP | J | m | CE | 134.6 | — | 3.16 | 4 | 0 | 24 | 1 | 37 | 34 | |
| 20 | SP | J | m | CE | 134.6 | — | 3.1 | 5 | 0 | 24 | 71 | 43 | 41 | 1.16 |
| 21 | SP | J | m | CE | 134.6 | — | 2.73 | 5 | 0 | 23 | 1 | 43 | 50 | |
| 22 | SP | J | m | CE | 134.6 | — | 2.77 | 5 | 0 | 24 | 41 | 43 | 51 | 1 |
| 23 | SP | ID | m | OE | 165.1 | 5 | 4 | 6 | 0.6 | 288 | 6 | 18 | 26 | |
| 24 | SP | ID | m | OE | 165.1 | 5 | 4 | 6 | 0.5 | 216 | 114 | 20 | 26 | 1.11 |
| 25 | SP | ID | m | OE | 165.1 | 5 | 4 | 6 | 0.6 | 364 | 7 | 23 | 27 | |
| 26 | SP | ID | m | OE | 165.1 | 5 | 4 | 6 | 0.6 | 258 | 119 | 26 | 27 | 1.13 |
| 27 | DK | ID | m | OE | 457 | 13.5 | 19.31 | 22 | 0.6 | 90 | 9 | 52 | 53 | |
| 28 | DK | ID | m | OE | 457 | 13.5 | 18.85 | 22 | 0.5 | 84 | 235 | 119 | 50 | 2.29 |
| 29 | DK | ID | m | OE | 324 | 19.1 | 11.1 | 14 | 0.5 | 64 | 188 | 34 | 50 | |
| 30 | DK | ID | m | OE | 324 | 19.1 | 11.1 | 14 | 0.5 | 64 | 1991 | 64 | 50 | 1.88 |
| 31 | DK | ID | m | OE | 324 | 19.1 | 22 | 14 | 0.6 | 136 | 188 | 77 | 52 | |
| 32 | DK | ID | m | OE | 324 | 19.1 | 22 | 14 | 0.6 | 136 | 1988 | 142 | 52 | 1.84 |
| 33 | DK | ID | m | OE | 51 | 8 | 2 | 40 | 0.2 | 687 | 1 | 157 | 93 | |
| 34 | DK | ID | m | OE | 51 | 8 | 2 | 40 | 0.2 | 687 | 85 | 273 | 93 | 1.74 |
| 35 | BL | ID | m | OE | 340 | 14 | 7 | 16 | 0.7 | 93 | 1 | 46 | 64 | |
| 36 | BL | ID | m | OE | 340 | 14 | 7 | 16 | 0.7 | 84 | 220 | 132 | 68 | 2.87 |

References: No. 1-14 Schneider (2007), No. 15-22 Lim and Lehane (2014), No. 23-26 Anusic et al. (2019a), No. 27-28 Jardine, Standing, and Chow (2006), No. 29-32 Chow et al. (1997); No. 33-34 Carroll et al. (2017), No. 35-36 Gavin, Igoe, and Kirwan (2013); SP - Shenton Park (Western Australia), DK - Dunkirk (France), BL - Blessington (Ireland), m - mild steel, OE - open ended, CE - closed ended

TABLE B.3: UWA-05 capacity prediction for specific CPT positions - Chapter 4.

| CPT | UWA-05 calculated tension capacities [kN] | |
| --- | --- | --- |
| | RCLA = 6.9 µm mild steel | RCLA = 2.9 µm stainless steel |
| CPT 1 | 90.6 | 55.4 |
| CPT 2 | 87.01 | 51.95 |
| CPT 4 | 94.63 | 58.92 |
| CPT 6 | 91.55 | 56.07 |
| CPT 7 | 90.94 | 54.8 |
| CPT 8 | 92.01 | 55.75 |
| CPT 9 | 85.53 | 50.42 |
| CPT 10 | 87.01 | 51.92 |
| CPT 11 | 87.38 | 52.52 |
| CPT 13 | 92.07 | 55.88 |

TABLE B.4: Final values used for modeling of corrosion scenarios - Chapter 6.

| | Symbol | Unit | Corrosion scenarios | | | | |
| --- | --- | --- | --- | --- | --- | --- | --- |
| | | | 1 | 2 | 3 | 4 | 5 |
| Used for both | $s$ | kg m$^{-3}$ | 2675 | 2675 | 2675 | 2675 | 2675 |
| | $d$ | kg m$^{-3}$ | 1610 | 1610 | 1610 | 1610 | 1610 |
| | $e_0$ | - | 0.56 | 0.56 | 0.56 | 0.56 | 0.56 |
| | $cv$ (us) | degree | 28.8 | 24 | 28 | 32 | 32 |
| | $cv$ (ls) | degree | 28.8 | 24 | 28 | 28 | 32 |
| | Sa (us) | µm | 10 | 11 | 44 | 301 | 301 |
| | Sa (ls) | µm | 10 | 11 | 44 | 44 | 301 |
| Large-diameter | Loading | - | c | c | c | c | c |
| | D | m | 4.3 | 4.3 | 4.3 | 4.3 | 4.3 |
| | V | m | 1.59 | 1.59 | 1.59 | 1.59 | 1.59 |
| | L | m | 18.7 | 18.7 | 18.7 | 18.7 | 18.7 |
| | $w_1$ | mm | 45 | 45 | 45 | 45 | 45 |
| | $w_2$ | mm | 40 | 40 | 40 | 40 | 40 |
| | C | m | 6.2 | 6.2 | 6.2 | 6.2 | 6.2 |
| | MGL | m | 5.5 | 5.5 | 5.5 | 5.5 | 5.5 |
| | CPT | - | 1 | 1 | 1 | 1 | 1 |
| | Opening | - | OE | OE | OE | OE | OE |
| Small-diameter | Loading | - | t | t | t | t | t |
| | D | mm | 35 | 35 | 35 | 35 | 35 |
| | V | cm | 35 | 35 | 35 | 35 | 35 |
| | L | m | 11.75 | 11.75 | 11.75 | 11.75 | 11.75 |
| | MGL | m | 3.5 | 3.5 | 3.5 | 3.5 | 3.5 |
| | CPT | - | 2 | 2 | 2 | 2 | 2 |
| | Opening | - | CE | CE | CE | CE | CE |

us - upper segment, ls - lower segment, OE - open ended, CE - closed ended

TABLE B.5: Combined grain size data for various compared sands - Chapter 6.

| Sands | $D_{10}$ [mm] | $D_{30}$ [mm] | $D_{50}$ [mm] | $D_{60}$ [mm] | Cu - | Cc - | GRAD. - | REF - |
|---|---|---|---|---|---|---|---|---|
| Cuxhaven Sand | 0.08 | 0.16 | 0.2 | 0.24 | 3.0 | 1.3 | PG | TS |
| SFS Sand | 0.09 | 0.11 | 0.13 | 0.14 | 1.6 | 1.0 | PG | [1][2] |
| MGS Sand | 0.34 | 0.4 | 0.44 | 0.45 | 1.3 | 1.0 | PG | [1][2] |
| VLB Sand | 0.64 | 0.7 | 0.78 | 0.81 | 1.3 | 0.9 | PG | [1][2] |
| FS Ohio Fine Sand | 0.2 | 0.27 | 0.35 | 0.3 | 1.5 | 1.2 | PG | [3] |
| FS Ohiho SW Sand | 0.18 | 0.5 | 1.04 | 1.2 | 6.7 | 1.2 | WG | [3] |
| FS Ohiho Coarse Sand | 0.9 | 1.3 | 1.5 | 1.9 | 2.1 | 1.0 | PG | [3] |
| FF Sand | 0.05 | 0.07 | 0.09 | 0.1 | 2.0 | 1.0 | PG | [4] |
| Toyoura Sand | 0.19 | 0.21 | 0.22 | 0.24 | 1.3 | 1.0 | PG | [4] |
| Ticino Sand | 0.35 | 0.44 | 0.56 | 0.62 | 1.8 | 0.9 | PG | [4] |

Classification according to Unified Soil Classification System; Cu - coefficient of uniformity, Cc - coefficient of curvature, GRAD. - graduation, REF- reference, PG - poorly graded; WG - well graded, TS - this study; [1] - Lings and Dietz (2005), [2] - Dietz and Lings (2006), [3] - Han et al. (2018), [4] - Porcino et al. (2003)

TABLE B.6: Interface shear data for for preserved surfaces - Chapter 6

| | No. | Surface | Exp. | $Sa$ | $N$ | $max$ | $cv$ | $max$ | $cv$ |
|---|---|---|---|---|---|---|---|---|---|
| | - | - | - | [µm] | [kN] | [kPa] | [kPa] | [degree] | [degree] |
| | 1 | PA01_0 | PS03.1 | 15 | 300 | 138 | 122 | 25 | 22 |
| | 2 | PA01_1 | PS03.2 | 15 | 200 | 96 | 81 | 25 | 22 |
| | 3 | PA01_2 | PS03.3 | 15 | 100 | 51 | 44 | 25 | 22 |
| | 4 | PA02_0 | PS04.1 | 11 | 300 | 134 | 109 | 25 | 21 |
| | 5 | PA02_1 | PS04.2 | 11 | 200 | 105 | 87 | 25 | 21 |
| | 6 | PA02_2 | PS04.3 | 11 | 100 | 51 | 39 | 25 | 21 |
| | 7 | PA03_0 | PS08.1 | 9 | 300 | 174 | 134 | 30 | 24 |
| | 8 | PA03_1 | PS08.2 | 9 | 200 | 120 | 90 | 30 | 24 |
| | 9 | PA03_2 | PS08.3 | 9 | 100 | 54 | 42 | 30 | 24 |
| | 10 | PA04_4 | PS01.4 | 8 | 100 | 51 | 44 | 27 | 24 |
| | 11 | PA04_2 | PS01.2 | 8 | 200 | 111 | 94 | 27 | 24 |
| Preserved surfaces (surfaces 1) | 12 | PA04_3 | PS01.3 | 8 | 300 | 143 | 129 | 27 | 24 |
| | 13 | PA05_0 | PS10.1 | 11 | 300 | 169 | 151 | 30 | 27 |
| | 14 | PA05_1 | PS10.2 | 11 | 200 | 121 | 109 | 30 | 27 |
| | 15 | PA05_2 | PS10.3 | 11 | 100 | 61 | 49 | 30 | 27 |
| | 16 | PA06_0 | PS12.1 | 9 | 300 | 186 | 160 | 32 | 27 |
| | 17 | PA06_1 | PS12.2 | 9 | 200 | 127 | 103 | 32 | 27 |
| | 18 | PA06_2 | PS12.3 | 9 | 100 | 57 | 43 | 32 | 27 |
| | 19 | PA07_0 | PS13.1 | 11 | 300 | 168 | 148 | 29 | 26 |
| | 20 | PA07_1 | PS13.2 | 11 | 200 | 105 | 97 | 29 | 26 |
| | 21 | PA07_2 | PS13.3 | 11 | 100 | 52 | 49 | 29 | 26 |
| | 22 | PA08_0 | PS14.1 | 10 | 300 | 187 | 138 | 32 | 25 |
| | 23 | PA08_1 | PS14.2 | 10 | 200 | 123 | 91 | 32 | 25 |
| | 24 | PA08_2 | PS14.3 | 10 | 100 | 62 | 44 | 32 | 25 |
| | 25 | PA09_0 | PS17.1 | 12 | 300 | 166 | 127 | 28 | 22 |
| | 26 | PA09_1 | PS17.2 | 12 | 200 | 95 | 70 | 28 | 22 |
| | 27 | PA09_2 | PS17.3 | 12 | 100 | 51 | 40 | 28 | 22 |

TABLE B.7: Interface shear data for air corroded surfaces - Chapter 6

| | No. | Surface | Exp. | $S_a$ | $N$ | $max$ | $cv$ | $max$ | $cv$ |
|---|---|---|---|---|---|---|---|---|---|
| | - | - | - | [µm] | [kN] | [kPa] | [kPa] | [degree] | [degree] |
| Air-corroded surfaces (surfaces 2) | 55 | PI01_0 | PS05.1 | 56 | 300 | 331 | 145 | 48 | 27 |
| | 56 | PI01_1 | PS05.2 | 56 | 200 | 222 | 104 | 48 | 27 |
| | 57 | PI01_2 | PS05.3 | 56 | 100 | 116 | 62 | 48 | 27 |
| | 58 | PI02_0 | PS06.1 | 49 | 300 | 307 | 158 | 45 | 27 |
| | 59 | PI02_1 | PS06.2 | 49 | 200 | 201 | 97 | 45 | 27 |
| | 60 | PI02_2 | PS06.3 | 49 | 100 | 99 | 54 | 45 | 27 |
| | 61 | PI03_0 | PS07.1 | 27 | 300 | 313 | 157 | 45 | 27 |
| | 62 | PI03_1 | PS07.2 | 27 | 200 | 182 | 95 | 45 | 27 |
| | 63 | PI03_2 | PS07.3 | 27 | 100 | 96 | 53 | 45 | 27 |
| | 64 | PI04_0 | PS15.1 | 108 | 300 | 294 | 178 | 45 | 30 |
| | 65 | PI04_1 | PS15.2 | 108 | 200 | 196 | 109 | 45 | 30 |
| | 66 | PI04_2 | PS15.3 | 108 | 100 | 107 | 61 | 45 | 30 |
| | 67 | PI05_0 | PS09.1 | 27 | 300 | 289 | 143 | 44 | 27 |
| | 68 | PI05_1 | PS09.2 | 27 | 200 | 189 | 115 | 44 | 27 |
| | 69 | PI05_2 | PS09.3 | 27 | 100 | 90 | 45 | 44 | 27 |
| | 70 | PI06_0 | PS11.1 | 30 | 300 | 279 | 180 | 42 | 30 |
| | 71 | PI06_1 | PS11.2 | 30 | 200 | 169 | 104 | 42 | 30 |
| | 72 | PI06_2 | PS11.3 | 30 | 100 | 83 | 57 | 42 | 30 |
| | 73 | PI07_0 | PS16.1 | 36 | 300 | 274 | 145 | 43 | 27 |
| | 74 | PI07_1 | PS16.2 | 36 | 200 | 186 | 107 | 43 | 27 |
| | 75 | PI07_2 | PS13.3 | 36 | 100 | 90 | 55 | 43 | 27 |
| | 76 | PI08_0 | PS18.1 | 30 | 300 | 272 | 170 | 43 | 29 |
| | 77 | PI08_1 | PS18.2 | 30 | 200 | 190 | 112 | 43 | 29 |
| | 78 | PI08_2 | PS18.3 | 30 | 100 | 97 | 56 | 43 | 29 |
| | 79 | PI09_0 | PS20.1 | 29 | 300 | 284 | 165 | 43 | 28 |
| | 80 | PI09_1 | PS20.2 | 29 | 200 | 189 | 103 | 43 | 28 |
| | 81 | PI09_2 | PS20.3 | 29 | 100 | 91 | 42 | 43 | 28 |

TABLE B.8: Interface shear data for artificial surfaces - Chapter 6

| | No. | Surface | Exp. | $Sa$ | $N$ | $max$ | $cv$ | $max$ | $cv$ |
|---|---|---|---|---|---|---|---|---|---|
| | - | - | - | [μm] | [kN] | [kPa] | [kPa] | [degree] | [degree] |
| Artificial surfaces (surfaces 3) | 28 | PA10_0 | PS19.1 | 38 | 100 | 109 | 67 | 44 | 30 |
| | 29 | PA10_1 | PS19.2 | 38 | 200 | 202 | 129 | 44 | 30 |
| | 30 | PA10_2 | PS19.3 | 38 | 300 | 278 | 159 | 44 | 30 |
| | 31 | PA11_0 | PS22.1 | 83 | 300 | 281 | 171 | 44 | 30 |
| | 32 | PA11_1 | PS22.2 | 83 | 200 | 203 | 120 | 44 | 30 |
| | 33 | PA11_2 | PS22.3 | 83 | 100 | 110 | 57 | 44 | 30 |
| | 34 | PA12_3 | PS24.4 | 38 | 300 | 309 | 150 | 44 | 26 |
| | 35 | PA12_0 | PS24.1 | 38 | 200 | 176 | 95 | 44 | 26 |
| | 36 | PA12_2 | PS24.3 | 38 | 100 | 86 | 42 | 44 | 26 |
| | 37 | PA13_0 | PS25.1 | 27 | 300 | 268 | 167 | 42 | 28 |
| | 38 | PA13_1 | PS25.2 | 27 | 200 | 173 | 95 | 42 | 28 |
| | 39 | PA13_2 | PS25.3 | 27 | 100 | 96 | 46 | 42 | 28 |
| | 40 | PA14_2 | PS28.3 | 25 | 100 | 98 | 61 | 44 | 30 |
| | 41 | PA14_0 | PS28.1 | 25 | 200 | 192 | 101 | 44 | 30 |
| | 42 | P14A_1 | PS28.2 | 25 | 300 | 284 | 178 | 44 | 30 |
| | 43 | PA15_1 | PS02.1 | 25 | 300 | 280 | 158 | 43 | 28 |
| | 44 | PA15_0 | PS02.2 | 25 | 200 | 197 | 117 | 43 | 28 |
| | 45 | PA15_2 | PS02.3 | 25 | 100 | 94 | 47 | 43 | 28 |
| | 46 | PA16_2 | PS29.3 | 67 | 300 | 286 | 175 | 43 | 29 |
| | 47 | PA16_3 | PS29.4 | 67 | 200 | 171 | 100 | 43 | 29 |
| | 48 | PA16_4 | PS29.5 | 67 | 100 | 95 | 53 | 43 | 29 |
| | 49 | PA17_0 | PS30.1 | 65 | 100 | 101 | 54 | 45 | 30 |
| | 50 | PA17_1 | PS30.2 | 65 | 200 | 198 | 99 | 45 | 30 |
| | 51 | PA17_2 | PS30.3 | 65 | 300 | 299 | 184 | 45 | 30 |
| | 52 | PA18_0 | PS31.1 | 73 | 300 | 280 | 174 | 44 | 29 |
| | 53 | PA18_1 | PS31.2 | 73 | 200 | 191 | 102 | 44 | 29 |
| | 54 | PA18_3 | PS31.4 | 73 | 100 | 113 | 50 | 44 | 29 |

TABLE B.9: Interface shear data for adhering crusts - Chapter 6

| | No. | Surface | Exp. | $S_a$ | $N$ | $max$ | $cv$ | $max$ | $cv$ |
|---|---|---|---|---|---|---|---|---|---|
| | - | - | - | [µm] | [kN] | [kPa] | [kPa] | [degree] | [degree] |
| Adhering sand crusts (surfaces 4) | 82 | PI10_3 | PS21.4 | 139 | 300 | 294 | 157 | 45 | 28 |
| | 83 | PI10_1 | PS21.2 | 139 | 200 | 211 | 109 | 45 | 28 |
| | 84 | PI10_2 | PS21.3 | 139 | 100 | 112 | 66 | 45 | 28 |
| | 85 | PI12_0 | PS27.1 | 154 | 300 | 312 | 163 | 45 | 27 |
| | 86 | PI12_1 | PS27.2 | 154 | 200 | 180 | 91 | 45 | 27 |
| | 87 | PI12_2 | PS27.3 | 154 | 100 | 112 | 52 | 45 | 27 |
| | 88 | PI13_0 | PS23.1 | 110 | 300 | 294 | 191 | 45 | 33 |
| | 89 | PI13_1 | PS23.2 | 110 | 200 | 209 | 136 | 45 | 33 |
| | 90 | PI13_2 | PS23.3 | 110 | 100 | 111 | 76 | 45 | 33 |
| | 91 | PI14_0 | PS26.1 | 152 | 300 | 294 | 179 | 45 | 31 |
| | 92 | PI14_1 | PS26.2 | 152 | 200 | 202 | 128 | 45 | 31 |
| | 93 | PI14_2 | PS26.3 | 152 | 100 | 100 | 63 | 45 | 31 |
| | 94 | P15I_3 | PS32.1 | 621 | 100 | 111 | 86 | 45 | 38 |
| | 95 | P15I_1 | PS32.2 | 621 | 200 | 195 | 150 | 45 | 38 |
| | 96 | P15I_2 | PS32.3 | 621 | 300 | 296 | 237 | 45 | 38 |
| | 97 | PI16_0 | PS34.1 | 631 | 100 | 97 | 48 | 41 | 24 |
| | 98 | PI16_1 | PS34.2 | 631 | 200 | 186 | 99 | 41 | 24 |
| | 99 | PI16_2 | PS34.3 | 631 | 300 | 256 | 129 | 41 | 24 |
| | 100 | PI17_0 | PS35.1 | 531 | 100 | 103 | 44 | 44 | 26 |
| | 101 | PI17_1 | PS35.2 | 531 | 200 | 205 | 99 | 44 | 26 |
| | 102 | PI17_2 | PS35.3 | 531 | 300 | 286 | 142 | 44 | 26 |
| | 103 | PI18_3 | PS33.1 | 605 | 100 | 107 | 63 | 46 | 32 |
| | 104 | PI18_1 | PS33.2 | 605 | 200 | 194 | 126 | 46 | 32 |
| | 105 | PI18_2 | PS33.3 | 605 | 300 | 311 | 188 | 46 | 32 |

TABLE B.10: Interface shear data for mounted crusts - Chapter 6

| | No. | Surface | Exp. | $Sa$ | $N$ | $max$ | $cv$ | $max$ | $cv$ |
|---|---|---|---|---|---|---|---|---|---|
| | - | - | - | [μm] | [kN] | [kPa] | [kPa] | [degree] | [degree] |
| | 106 | K01_0 | SK06.1 | 652 | 100 | 95 | 40 | 39 | 20 |
| | 107 | K01_1 | SK06.2 | 652 | 200 | 173 | 78 | 39 | 20 |
| | 108 | K01_2 | SK06.3 | 652 | 300 | 234 | 108 | 39 | 20 |
| | 109 | K02_0 | SK01.1 | 250 | 100 | 108 | 43 | 44 | 24 |
| | 110 | K02_1 | SK01.2 | 250 | 200 | 204 | 97 | 44 | 24 |
| | 111 | K02_2 | SK01.3 | 250 | 300 | 283 | 133 | 44 | 24 |
| | 112 | K03_0 | SK07.1 | 577 | 100 | 99 | 48 | 42 | 24 |
| | 113 | K03_1 | SK07.2 | 577 | 200 | 152 | 70 | 42 | 24 |
| | 114 | K03_2 | SK07.3 | 577 | 300 | 293 | 144 | 42 | 24 |
| | 115 | K04_3 | SK08.4 | 544 | 100 | 105 | 46 | 43 | 24 |
| | 116 | K04_1 | SK08.2 | 544 | 200 | 186 | 88 | 43 | 24 |
| | 117 | K04_2 | SK08.3 | 544 | 300 | 275 | 130 | 43 | 24 |
| | 118 | K05_0 | SK04.1 | 668 | 100 | 98 | 42 | 39 | 20 |
| | 119 | K05_1 | SK04.2 | 668 | 200 | 152 | 63 | 39 | 20 |
| | 120 | K05_2 | SK04.3 | 668 | 300 | 249 | 116 | 39 | 20 |
| | 121 | K06_0 | SK05.1 | 589 | 100 | 98 | 42 | 45 | 26 |
| | 122 | K06_1 | SK05.2 | 589 | 200 | 203 | 79 | 45 | 26 |
| | 123 | K06_2 | SK04.3 | 589 | 300 | 296 | 157 | 45 | 26 |
| | 124 | K07_1 | SK02.1 | 474 | 100 | 76 | 18 | 45 | 24 |
| | 125 | K07_2 | SK02.2 | 474 | 200 | 203 | 92 | 45 | 24 |
| | 126 | K07_3 | SK02.3 | 474 | 300 | 312 | 144 | 45 | 24 |
| | 127 | K08_0 | SK09.1 | 676 | 100 | 88 | 33 | 44 | 26 |
| | 128 | K08_1 | SK09.2 | 676 | 200 | 181 | 86 | 44 | 26 |
| | 129 | K08_2 | SK09.3 | 676 | 300 | 308 | 159 | 44 | 26 |
| | 130 | K09_0 | SK03.1 | 505 | 100 | 100 | 40 | 48 | 25 |
| | 131 | K09_1 | SK03.2 | 505 | 200 | 216 | 94 | 48 | 25 |
| | 131 | K09_2 | SK03.3 | 505 | 300 | 336 | 144 | 48 | 25 |

The left margin contains the rotated label: Mounted sand crusts (surfaces 5)

## B.2 Raw - supplemental data

The following raw data is stored on the permanent and scientific data-repository **Pangaea** for Earth & Environmental Science:

1. Cone penetration data used for soil classification and pile capacity prediction regarding Chapter 4

2. All load displacement curves of pile tension load tests regarding Chapter 4

3. All constant normal load direct shear data of sand-to-sand, and sand-to-interface shear tests regarding Chapter 6

# Bibliography

Abdel-Rahman, S.M. (2011). "Vibration Associated With Pile Driving and Its Effects on Nearby Historical Structures". In: *IMAC-XX: Conference & Exposition on Structural Dynamics*, pp. 1251–1258. ISSN: 0277786X.

Achmus, Martin, Kirill Alexander Schmoor, Volker Herwig, and Benjamin Matlock (2020). "Lateral bearing behaviour of vibro- and impact-driven large-diameter piles in dense sand". In: *geotechnik* 43.3, pp. 147–159. ISSN: 0172-6145. DOI: 10.1002/gete.202000006.

Airhart, Tom P, Teddy James Hirsch, and Harry M Coyle (1967). *Pile-soil system response in clay as a function of excess pore water pressure and other soil properties*. Texas Transportation Institute.

Al-Sammarraie, D, S Kreiter, F T Stähler, M Goodarzi, and T Mörz (2018). "New vibratory cone penetration device for in-situ measurement of cyclic softening". In: *Cone Penetration Testing 2018*. CRC Press, pp. 79–84.

Al-Sammarraie, Dina (2020). "Vibratory cone penetration test to investigate cyclic soil behavior in-situ". PhD. Thesis. University of Bremen.

Al-Sammarraie, Dina, Stefan Kreiter, Max O. Kluger, and Tobias Mörz (2020). "Reliability of CPT measurements in sand – influence of spacing". In: *Géotechnique*, pp. 1–38. ISSN: 0016-8505. DOI: 10.1680/jgeot.19.P.247.

Alvarez, Camilo, Brian Zuckerman, and John Lemke (2006). "Dynamic Pile Analysis Using CAPWAP and Multiple Sensors". In: *GeoCongress 2006*. Reston, VA: American Society of Civil Engineers, pp. 1–5. ISBN: 978-0-7844-0803-2. DOI: 10.1061/40803(187)173.

Anusic, Ivana, Barry M. Lehane, Gudmund R. Eiksund, and Morten A. Liingaard (2019a). "Evaluation of installation effects on set-up of field displacement piles in sand". In: *Canadian Geotechnical Journal* 56.4, pp. 461–472. ISSN: 0008-3674. DOI: 10.1139/cgj-2017-0730.

— (2019b). "Influence of installation method on static lateral response of displacement piles in sand". In: *Géotechnique Letters* 9.3, pp. 193–197. ISSN: 2045-2543. DOI: 10.1680/jgele.18.00191.

API (2006). *DRAFT recommended practice for planning, designing, and constructing fixed offshore platforms - Working stress design*. Tech. rep. Washington DC. DOI: 10.1088/1751-8113/44/8/085201. arXiv: 1011.1669.

Ashour, Mohamed, G Norris, and P Pilling (1998). "Lateral loading of a pile in layered soil using the strain wedge model". In: *Journal of geotechnical and geoenvironmental engineering* 124.4, pp. 303–315.

Axelsson, Gary (1998). "Long term set-up of driven piles in non-cohesive soils evaluated from dynamic tests on penetration rods". In: *Geotechnical Site Characterization*.

— (2000). "Long-Term Set-Up of driven Piles in Sand". Doctoral Thesis. Stockholm.

Baldi, G, R Bellotti, V. N. Ghionna, M. Jamiolkowski, and E Pasqualini (1986). "Interpretation of CPT's and CPTU's. 2nd Part: Drained Penetration". In: *Proceeding 4th International Geotechnical Seminar*. Singapore, pp. 143–15.

Billamboz, André (2014). "Regional patterns of settlement and woodland developments: Dendroarchaeology in the Neolithic pile-dwellings on Lake Constance (Germany)". In: *The Holocene* 24.10, pp. 1278–1287. ISSN: 0959-6836. DOI: 10.1177/0959683614540956.

Biryaltseva, T., Tobias Mörz, S. Brandt, S. Kreiter, U. Gerdes, and B. Ossig (2016). "Relative densities and void ratios derived from CPT data using in situ field calibration". In: *Proceedings of the 5th International Conference on Geotechnical and Geophysical Site Characterisation, ISC 2016* 1.1993, pp. 383–388.

Bittar, Eduardo, Barry Lehane, Phil Watson, and Andrew Deeks (2020). "Effect of cyclic history on the ageing of shaft friction of driven piles in sand". In: *Proceedings of the 4th International Symposium on Frontiers in Offshore Geotechnics*. 2006. United States: American Society of Civil Engineers, pp. 541–550.

Bowman, Elisabeth T. and Kenichi Soga (2005). "Mechanisms of setup of displacement piles in sand: laboratory creep tests". In: *Canadian Geotechnical Journal* 42.5, pp. 1391–1407. ISSN: 0008-3674. DOI: 10.1139/t05-063.

Bradshaw, Aaron S. and Christopher D. P. Baxter (2006). *Design and construction of driven pile foundations–lessons learned on the Central Artery/Tunnel project*. Tech. rep. University of Rhode Island.

Briaud, Jean-Louis and Larry M Tucker (1988). "Measured and predicted axial response of 98 piles". In: *Journal of Geotechnical Engineering* 114.9, pp. 984–1001.

Brinch Hansen, J (1963). "Discussion of Hyperbolic Stress-Strain Response: Cohesive Soil. by Robert L. Kondner". In: *J. Soil Mech., Found. Div., ASCE* 89.4, pp. 241–242.

Buitrago, Jaime and Patrick C Wong (2003). *Fatigue Design Of Driven Piles For Deepwater Applications*.

Bullock, Paul J., John H. Schmertmann, Michael C. McVay, and Frank C. Townsend (2005a). "Side Shear Setup. I: Test Piles Driven in Florida". In: *Journal of Geotechnical and Geoenvironmental Engineering* 131.3, pp. 292–300. ISSN: 1090-0241. DOI: 10.1061/(ASCE)1090-0241(2005)131:3(292).

— (2005b). "Side Shear Setup. II: Results From Florida Test Piles". In: *Journal of Geotechnical and Geoenvironmental Engineering* 131.3, pp. 301–310. ISSN: 1090-0241. DOI: 10.1061/(ASCE)1090-0241(2005)131:3(301).

Busch, Alexander V., Max O. Kluger, Daniel A. Hepp, Majid Goodarzi, Stefan Kreiter, and Tobias Mörz (2022). "Installation and aging effects on the capacity of small displacement piles". In: *Geomechanics for Energy and the Environment*, p. 100350. ISSN: 23523808. DOI: 10.1016/j.gete.2022.100350.

Carroll, R., P. Carotenuto, C. Dano, I. Salama, Matias Silva, Kenneth George Gavin, and Richard J. Jardine (2017). "Field Studies on the Axial Capacity of Small Diameter Piles and Ageing Effects in Sands". In: *Offshore Site Investigation Geotechnics 8th International Conference Proceedings*. Vol. 0. Society of Underwater Technology, pp. 1160–1169. DOI: 10.3723/OSIG17.1160.

Carroll, R., P. Carotenuto, C. Dano, I. Salama, M. Silva, S. Rimoy, Kenneth George Gavin, and Richard J. Jardine (2019). "Field experiments at three sites to investigate the effects of age on steel piles driven in sand". In: *Géotechnique* 2.6, pp. 1–21. ISSN: 0016-8505. DOI: 10.1680/jgeot.17.P.185.

Chen Yang, Nai-Chen (1956). "Redriving characteristics of piles". In: *Journal of the Soil Mechanics and Foundations Division* 82.3, pp. 1021–1026.

Chin, Fung Kee (1970). "Estimation of the ultimate load of piles from tests not carried to failure". In: *Proc. 2nd Southeast Asian Conference on Soil Engineering, Singapore, 1970*.

Chow, Fiona C. (1996). "Investigations into the behaviour of displacement piles for offshore foundations". PhD. Thesis. University of London. DOI: 10.1016/0148-9062(96)83559-5.

Chow, Fiona C., Richard J. Jardine, J. F. Nauroy, and F. Brucy (1997). "Time-related increases in the shaft capacities of driven piles in sand". In: *Géotechnique* 47.2, pp. 353–361. ISSN: 0016-8505. DOI: 10.1680/geot.1997.47.2.353.

Chow, Fiona C., Richard J. Jardine, F. Brucy, and J. F. Nauroy (1998). "Effects of Time on Capacity of Pipe Piles in Dense Marine Sand". In: *Journal of Geotechnical and Geoenvironmental Engineering* 125.11, pp. 1028–1028. ISSN: 1090-0241. DOI: 10.1061/(asce)1090-0241(1999)125:11(1028).

Chung, Jean, Régis Wallerand, and Morgane Hélias-Brault (2013). "Pile Fatigue Assessment During Driving". In: *Procedia Engineering* 66, pp. 451–463. ISSN: 18777058. DOI: 10.1016/j.proeng.2013.12.098.

Cleveland, William S (1979). "Robust locally weighted regression and smoothing scatterplots". In: *Journal of the American statistical association* 74.368, pp. 829–836.

Cudmani, R. (2001). "Statische, alternierende und dynamische Penetration in nicht-bindigen Böden". PhD thesis.

Dai, Bei Bing, Jun Yang, and Cui Ying Zhou (2016). "Observed effects of interparticle friction and particle size on shear behavior of granular materials". In: *International Journal of Geomechanics* 16.1, p. 4015011.

DFI (2014). *Comparison of impact versus vibratory driven piles: with a focus on soil - structure interaction*. REV2. Gavin & Doherty - Geo Solutions, p. 76.

Dietz, Matthew S. and Martin L. Lings (2006). "Postpeak Strength of Interfaces in a Stress-Dilatancy Framework". In: *Journal of Geotechnical and Geoenvironmental Engineering* 132.11, pp. 1474–1484. ISSN: 1090-0241. DOI: 10.1061/(ASCE)1090-0241(2006)132:11(1474).

DIN 18123 (2011). *Soil, investigation and testing - Determination of grain-size distribution*. Tech. rep. Deutsches Institut für Normen e. V.

DIN 18124 (2019). *Soil, investigation and testing - Determination of density of solid particles - Wide mouth pycnometer*. Tech. rep. Deutsches Institut für Normen e. V.

DIN 18126 (1996). *Soil, investigation and testing - Determination of density of non-cohesive soils for maximum and minimum compactness*. Tech. rep. Deutsches Institut für Normen e. V.

DIN EN 10027-2 (2015). *Designation systems for steels - Part 2: Numerical system; German version*. Tech. rep.

DIN EN ISO 14688-2 (2020). *Geotechnical investigation and testing — Identification and classification of soil — Part 2: Principles for a classification*. Tech. rep.

DIN EN ISO 17892-10 (2019). *Geotechnical investigation and testing - Laboratory testing of soil - Part 10: Direct shear tests*. Tech. rep.

DIN EN ISO 25178-3 (2012). *Geometrical product specifications (GPS) - Surface texture: Areal - Part 3: Specification operators*. Tech. rep.

DIN ISO 4324 (1983). *Surface active agents; powers and granules; measurement of the angle of response. Deutsches Institut für Normen e. V.* Tech. rep.

EA-Pfaehle (2012). *Empfehlungen des Arbeitskreises „Pfaehle": EA-Pfaehle*. Tech. rep. Weinheim, Germany. DOI: 10.1002/9783433601112.

Ehlers, Jürgen (1990). "Reconstructing the dynamics of the North-west European Pleistocene ice sheets". In: *Quaternary Science Reviews* 9.1, pp. 71–83. ISSN: 02773791. DOI: 10.1016/0277-3791(90)90005-U.

Ehlers, Jürgen, Alf Grube, Hans-Jürgen Stephan, and Stefan Wansa (2011). "Pleistocene glaciations of North Germany—new results". In: *Developments in quaternary sciences*. Vol. 15. Elsevier, pp. 149–162.

El Haffar, I., M. Blanc, and L. Thorel (2017). "Impact of pile installation method on the axial capacity in sand". In: *Géotechnique Letters* 7.3, pp. 260–265. ISSN: 2045-2543. DOI: 10.1680/jgele.17.00036.

Elmer, K, W Gerasch, T. Neumann, J. Gabriel, Klaus Betke, and M. Schulz-von Glahn (2007). "Measurement and Reduction of Offshore Wind Turbine Construction Noise". In: *DEWI Magazin* 30, pp. 33–38.

EN ISO 14688-1 (2018). *- Identification and classification of soil - Part 1: Identification and description (ISO 14688-1:2017); German version EN ISO 14688-1:2018. Deutsches Institut für Normen e. V.* Tech. rep.

Fellenius, Bengt H (1991). "Pile Foundations". In: *Foundation Engineering Handbook*. Boston, MA: Springer US, pp. 511–536. DOI: 10.1007/978-1-4757-5271-7_13.

Fellenius, Bengt H., Richard E Riker, Arthur J. O'Brien, and Gerald R Tracy (1989). "Dynamic and Static Testing in Soil Exhibiting Set-Up". In: *Journal of Geotechnical Engineering* 115.7, pp. 984–1001. ISSN: 0733-9410. DOI: 10.1061/(ASCE)0733-9410(1989)115:7(984).

Fischer, J, H Sychla, J Bakker, L de Neef, and J. Stahlmann (2013). "A comparison between impact driven and vibratory driven steel piles in the German North Sea". In: *Proceedings Conference on Maritime Energy (COME), Hamburg*, pp. 21–22.

Fleischer, Matthias, Stefan Kreiter, Tobias Mörz, and Marc Huhndorf (2016). "A small volume calibration chamber for cone penetration testing (CPT) on submarine soils". In: *Advances in Natural and Technological Hazards Research* 41, pp. 181–189. ISSN: 22136959. DOI: 10.1007/978-3-319-20979-1_18.

Fu, Wenxi, Xing Zheng, Xiaozhang Lei, and Jianhui Deng (2015). "Using a modified direct shear apparatus to explore gap and size effects on shear resistance of coarse-grained soil". In: *Particuology* 23, pp. 82–89. ISSN: 16742001. DOI: 10.1016/j.partic.2014.11.013.

Gadelmawla, E. S., M. M. Koura, T. M A Maksoud, I. M. Elewa, and H. H. Soliman (2002). "Roughness parameters". In: *Journal of Materials Processing Technology* 123.1, pp. 133–145. ISSN: 09240136. DOI: 10.1016/S0924-0136(02)00060-2.

Gattermann, Jörg, Volker Herwig, and Christian Moormann (2015). "VIBRO Project - Vergleich des lateralen Tragverhaltens von vibrierten und geschlagenen Stahlrohr - pfählen in sandigen Böden". In: *In Pfahl-Symposium 2015, Mitteilungen des Instituts für Grundbau und Bodenmechanik.*

Gavin, Kenneth George and David Igoe (2019). "A field investigation into the mechanisms of pile ageing in sand". In: *Géotechnique* 1997, pp. 1–12. ISSN: 0016-8505. DOI: 10.1680/jgeot.18.P.235.

Gavin, Kenneth George, David John Paul Igoe, and Lisa Kirwan (2013). "The effect of ageing on the axial capacity of piles in sand". In: *Proceedings of the Institution of Civil Engineers - Geotechnical Engineering* 166.2, pp. 122–130. DOI: 10.1680/geng.12.00064.

Gavin, Kenneth George and Brendan C. O'Kelly (2007). "Effect of Friction Fatigue on Pile Capacity in Dense Sand". In: *Journal of Geotechnical and Geoenvironmental Engineering* 133.1, pp. 63–71. ISSN: 1090-0241. DOI: 10.1061/(ASCE)1090-0241(2007)133:1(63).

Gavin, Kenneth George, Richard J. Jardine, Kjell Karlsrud, and Barry M. Lehane (2015). "The effects of pile ageing on the shaft capacity of offshore piles in sand". In: *Frontiers in Offshore Geotechnics III* 0.1, pp. 129–151. ISSN: 12086010. DOI: 10.1201/b18442-8.

Geo-Eng (2014). *Geotechnical site investigation report - VIBRO-project Altenwalde*. Tech. rep. Unpblished report - Geo-Engineering.org GmbH, pp. 1–154.

— (2015). *Baugrundbericht - Kalibration Nordsee - Altenwalde*. Tech. rep. Unpblished report - Geo-Engineering.org GmbH.

Goble, G G (1980). "Pile driving: a state-of-the art". In: *Seminar on the Application of Stress-Wave Theory on Pile*. Royal Institute of Technology.

González, Eva, Nico Deus, Jörg Elbracht, M Azizur Rahman, and Helga Wiederhold (2021). "Current and future state of groundwater salinization of the northern Elbe-Weser region". In: *Grundwasser* 26.4, pp. 343–356. ISSN: 1430-483X. DOI: 10.1007/s00767-021-00496-w.

Goodarzi, Majid, B. Ossig, L. S. Brandt, Alexander V. Busch, and P. Ghasemi (2019). "Axial capacity of impact-driven monopiles: the case study at Cuxhaven , Germany". In: Braunschweig: Pfahlsymposium.

GWEC (2014). "Global wind report". In: *Global Wind Energy Council*.

Han, Fei, Eshan Ganju, Rodrigo Salgado, and Monica Prezzi (2018). "Effects of Interface Roughness, Particle Geometry, and Gradation on the Sand–Steel Interface Friction Angle". In: *Journal of Geotechnical and Geoenvironmental Engineering* 144.12, p. 04018096. ISSN: 1090-0241. DOI: 10.1061/(ASCE)GT.1943-5606.0001990.

Heerema, Edward P. (1978). "Predicting Pile Driveability: Heather As An Illustration Of The "Friction Fatigue" Theory". In: *SPE European Petroleum Conference*. Society of Petroleum Engineers. DOI: 10.2118/8084-MS.

Holloway, D M and D L Beddard (1995). "Dynamic testing results, indicator pile test program–I-880, Oakland, California". In: *Proc. DFI 20th Ann. Memb. Conf*, pp. 105–126.

Holtz, Robert D, William D Kovacs, and Thomas C Sheahan (1981). *An introduction to geotechnical engineering*. Prentice-Hall Englewood Cliffs.

Hussein, Mohamad H., Michael R. Sharp, and William F. Knight (2012). "The Use of Superposition for Evaluating Pile Capacity". In: *Deep Foundations 2002*. Orlando, Florida, United States: American Society of Civil Engineers, pp. 6–21. ISBN: 9780784406014. DOI: 10.1061/40601(256)2.

Jardine, R J, N V Thomsen, M Mygind, M A Liingaard, and C L Thilsted (2015). "Axial capacity design practice for North European wind-turbine projects". In: *Proceedings of 3rd international symposium on frontiers in Offshore Geotechnics*, pp. 581–586.

Jardine, Richard J. and Fiona C. Chow (1996). *New design methods for offshore piles*. ISBN: 1870553314.

Jardine, Richard J., Barry M. Lehane, and S. J. Everton (1993). "Friction coefficients for piles in sands and silts". In: *Offshore Site Investigation* 28.1, pp. 661–677. DOI: 10.1007/978-94-017-2473-9_31.

Jardine, Richard J., J. R. Standing, and Fiona C. Chow (2006). "Some observations of the effects of time on the capacity of piles driven in sand". In: *Géotechnique* 56.4, pp. 227–244. ISSN: 0016-8505. DOI: 10.1680/geot.2006.56.4.227.

Jardine, Richard J., Fiona C. Chow, Overy R., and Standing J. (2005). *ICP Design Methods for Driven Piles in Sands and Clays*.

Jonker, G. (1987). "Vibratory Pile Driving Hammers for Pile Installations and Soil Improvement Projects". In: *Offshore Technology Conference*. Offshore Technology Conference. DOI: 10.4043/5422-MS.

Karlsrud, Kjell, Tor Georg Jensen, Ellen Katrine, Wensaas Lied, and Fritz Nowacki (2014). "Significant Ageing Effects for Axially Loaded Piles in Sand and Clay Verified by New Field Load Tests". In: February 2017. Houston: Offshore Technology Conference. DOI: 10.4043/25197-MS.

Kishida, H. and M. Uesugi (1987). "Tests of the interface between sand and steel in the simple shear apparatus". In: *Géotechnique* 37.1, pp. 45–52. ISSN: 0016-8505. DOI: 10.1680/geot.1987.37.1.45.

Kluger, Max O, Stefan Kreiter, Florian T Stähler, Majid Goodarzi, Tim Stanski, and Tobias Mörz (2021). "Cone penetration tests in dry and saturated Ticino sand". In: *Bulletin of Engineering Geology and the Environment* 80.5, pp. 4079–4088.

Kolk, H. J., A. E. Baaijens, and M. Senders (2005). "Design criteria for pipe piles in silica sands". In: *Frontiers in Offshore Geotechnics, ISFOG 2005 - Proceedings of the 1st International Symposium on Frontiers in Offshore Geotechnics*. ISBN: 0415390648. DOI: 10.1201/noe0415390637.ch80.

Komurka, Van E., Alan B. Wagner, and Tuncer B. Edil (2003). "A Review of Pile Set-Up". In: pp. 1–20.

Krige, Daniel G (1951). "A statistical approach to some basic mine valuation problems on the Witwatersrand". In: *Journal of the Southern African Institute of Mining and Metallurgy* 52.6, pp. 119–139.

Lagioia, Rocco, Alex Sanzeni, and Francesco Colleselli (2006). "Air, water and vacuum pluviation of sand specimens for the triaxial apparatus". In: *Soils and foundations* 46.1, pp. 61–67.

Lee, S. L., Y. K. Chow, G. P. Karunaratne, and K. Y. Wong (1988). "Rational Wave Equation Model for Pile-Driving Analysis". In: *Journal of Geotechnical Engineering* 114.3, pp. 306–325. ISSN: 0733-9410. DOI: 10.1061/(ASCE)0733-9410(1988)114:3(306).

Lehane, Barry M., James A. Schneider, and X. Xu (2005). "The UWA-05 method for prediction of axial capacity of driven piles in sand". In: *Frontiers in Offshore Geotechnics, ISFOG 2005 - Proceedings of the 1st International Symposium on Frontiers in Offshore Geotechnics*, pp. 683–689. DOI: 10.1201/noe0415390637.ch76.

— (2007). "Development of the UWA-05 Design Method for Open and Closed Ended Driven Piles in Siliceous Sand". In: *Contemporary Issues In Deep Foundations* 05.2006, pp. 1–10. ISSN: 08950563. DOI: 10.1061/40902(221)12.

Lehane, Barry M., Richard J. Jardine, A. J. Bond, and R. Frank (1993). "Mechanisms of Shaft Friction in Sand from Instrumented Pile Tests". In: *Journal of Geotechnical Engineering* 119.1, pp. 19–35. ISSN: 0733-9410. DOI: 10.1061/(ASCE)0733-9410(1993)119:1(19).

Lehane, Barry M., James A. Schneider, Jit Kheng Lim, and Giuseppe Mortara (2012). "Shaft Friction from Instrumented Displacement Piles in an Uncemented Calcareous Sand". In: *Journal of Geotechnical and Geoenvironmental Engineering* 138.11, pp. 1357–1368. ISSN: 1090-0241. DOI: 10.1061/(ASCE)GT.1943-5606.0000712.

Likins, Garland and Frank Rausche (2004). "Correlation of CAPWAP with static load tests". In: *Proceedings of the seventh international conference on the application of stresswave theory to piles*. Citeseer, pp. 153–165.

Lim, Jit Kheng (2013). "Time and scale effects on the shaft friction of displacement-piles in sand". PhD thesis. The University of Western Australia, Crawley, WA, Australia, p. 301.

Lim, Jit Kheng and Barry Lehane (2015). "Shearing resistance during pile installation in sand". In: *Proceedings of the Institution of Civil Engineers - Geotechnical Engineering* 168.3, pp. 227–235. ISSN: 1353-2618. DOI: 10.1680/geng.14.00066. arXiv: 0201333 [astro-ph].

Lim, Jit Kheng and Barry M. Lehane (2014). "Characterisation of the effects of time on the shaft friction of displacement piles in sand". In: *Géotechnique* 64.6, pp. 476–485. ISSN: 0016-8505. DOI: 10.1680/geot.13.P.220.

Lings, M. L. and M. S. Dietz (2005). "The peak strength of sand-steel interfaces and the role of dilation". In: *SOILS AND FOUNDATIONS* 45.6, pp. 1–14. ISSN: 1341-7452. DOI: 10.3208/sandf.45.1.

Liu, Tingfa, Haoruo Chen, Róisín M. Buckley, V. Santiago Quinteros, and Richard J. Jardine (2019). "Characterisation of sand-steel interface shearing behaviour for the interpretation of driven pile behaviour in sands". In: *E3S Web of Conferences* 92. Ed. by A. Tarantino and E. Ibraim, p. 13001. ISSN: 2267-1242. DOI: 10.1051/e3sconf/20199213001.

Martinez, A. and J. D. Frost (2017). *The influence of surface roughness form on the strength of sand–structure interfaces*. Vol. 7. 1. Schmidt, pp. 104–111. DOI: 10.1680/jgele.16.00169.

McVay, Michael C and Ching L Kuo (1999). *Estimate damping and quake by using traditional soil testing*. Tech. rep.

Miller, R M (1938). "Soil reactions in relation to foundations on piles". In: *Transactions of the American Society of Civil Engineers* 103.1, pp. 1193–1216.

Moayedi, H, M Mosallanezhad, and R Nazir (2017). "Evaluation of maintained load test (MLT) and pile driving analyzer (PDA) in measuring bearing capacity of driven reinforced concrete piles". In: *Soil Mechanics and Foundation Engineering* 54.3, pp. 150–154.

Monzón, Juan Carlos (2006). "Review of cpt based design methods for estimating axial capacity of driven piles in siliceous sand". In: *Department of Civil and Environmental Engineering*, p. 100.

Mosher, Reed L. (1990). "Axial Capacity of Vibratory-Driven Piles versus Impact-Driven Piles". In: *Modern geotechnical methods: instrumentation and vibratory hammers* 1, pp. 128–135. ISSN: 00167185.

Moshfeghi, Sara and Abolfazl Eslami (2018a). "Failure analysis of CPT-based direct methods for axial capacity of driven piles in sand". In: *Georisk: Assessment and Management of Risk for Engineered Systems and Geohazards* 13.1, pp. 1–19. ISSN: 1749-9518. DOI: 10.1080/17499518.2018.1478105.

— (2018b). "Study on pile ultimate capacity criteria and CPT-based direct methods". In: *International Journal of Geotechnical Engineering* 12.1, pp. 28–39. ISSN: 1938-6362. DOI: 10.1080/19386362.2016.1244150.

Musial, Walter and Bonnie Ram (2010). *Large-scale offshore wind power in the United States: Assessment of opportunities and barriers*. Tech. rep. National Renewable Energy Lab.(NREL), Golden, CO (United States).

Nehls, Georg, Armin Rose, Ansgar Diederichs, Michael Bellmann, and Hendrik Pehlke (2016). "Noise Mitigation During Pile Driving Efficiently Reduces Disturbance of Marine Mammals". In: pp. 755–762. DOI: 10.1007/978-1-4939-2981-8_92.

Ng, E, J Briaud, and L Tucker (1988). "Pile foundation. The behaviour of single pile in cohesionless soils". In: *Federal Highway Administration Report*.

Ng, Kam Weng and Sri Sritharan (2013). "Improving dynamic soil parameters and advancing the pile signal matching technique". In: *Computers and Geotechnics* 54, pp. 166–174. ISSN: 0266352X. DOI: 10.1016/j.compgeo.2013.07.007.

Oh, Ki-Yong, Woochul Nam, Moo Sung Ryu, Ji-Young Kim, and Bogdan I. Epureanu (2018). "A review of foundations of offshore wind energy convertors: Current status and future perspectives". In: *Renewable and Sustainable Energy Reviews* 88.June, pp. 16–36. ISSN: 13640321. DOI: 10.1016/j.rser.2018.02.005.

Olgun, Murat, Yavuz Yenginar, and Asihaer Hanati (2017). "Interpreting Load-Settlement Curves of Pile Foundations by Graphical Methods". In: *Eurasian Journal of Civil Engineering and Architecture* 1.1, pp. 1–10.

Osman, Mohamed A, Elfatih Mohamed Ali Ahmed, and Omar Babiker Elhaj Mohammed Ahmed (2013). "Comparison Between Dynamic and Static Pile Load Testing". In: *Electronic Journal of Geotechnical Engineering* 18, pp. 3615–3624.

Ozsu, Erdem, An-Ninh Ta, Bruno Stuyts, and Christophe Jaeck (2013). "Optimizing Pile Driving Fatigue for Offshore Foundations in Very Dense Sand: A Case Study". In: *Volume 6: Polar and Arctic Sciences and Technology; Offshore Geotechnics; Petroleum Technology Symposium*. American Society of Mechanical Engineers. ISBN: 978-0-7918-5540-9. DOI: 10.1115/OMAE2013-10664.

Paikowsky, SG, CM Player, and PJ Connors (1995). "A Dual Interface Apparatus for Testing Unrestricted Friction of Soil Along Solid Surfaces". In: *Geotechnical Testing Journal* 18.2, p. 168. ISSN: 01496115. DOI: 10.1520/GTJ10320J.

Pestana, Juan M, Christopher E Hunt, and Jonathan D Bray (2002). "Soil deformation and excess pore pressure field around a closed-ended pile". In: *Journal of geotechnical and geoenvironmental engineering* 128.1, pp. 1–12.

Pile Dynamics Inc. (2006). "CAPWAP Manual". In: *Cleveland Ohio, USA*.

Porcino, Daniela, Vincenzo Fioravante, Vito Nicola Ghionna, Sergio Pedroni, L David Suits, and TC Sheahan (2003). "Interface Behavior of Sands from Constant Normal Stiffness Direct Shear Tests". In: *Geotechnical Testing Journal* 26.3, p. 19513. ISSN: 01496115. DOI: 10.1520/GTJ11308J.

Preim, M J, R March, and M Hussein (1989). "Bearing capacity of piles in soils with time dependent characteristics". In: *Piling and Deep Foundations* 1, pp. 363–370.

Quinteros, V. Santiago, T. Lunne, L. Krogh, R. Bøgelund-Pedersen, and J. Brink Clausen (2018). "Shallow depth characterisation and stress history assessment of an overconsolidated sand in Cuxhaven, Germany". In: pp. 525–531.

Ramírez Lizet, Daniel Fraile, and Guy Brindley (2020). *Offshore wind in Europe - Key trends and statistics 2019*. Tech. rep.

Randolph, M. F. (2003). "Science and empiricism in pile foundation design". In: *Géotechnique* 53.10, pp. 847–875. ISSN: 0016-8505. DOI: 10.1680/geot.53.10.847.37518.

Randolph, M. F., R Dolwin, and R Beck (1994). "Design of driven piles in sand". In: *Géotechnique* 44.3, pp. 427–448. DOI: 10.1680/geot.1994.44.3.427.

Rausche, Frank, George G Goble, and Garland E Likins Jr (1985). "Dynamic determination of pile capacity". In: *Journal of Geotechnical Engineering* 111.3, pp. 367–383.

Rausche, Frank, Garland Likins, and Mohamad H. Hussein (2008). "Analysis of Post-Installation Dynamic Load Test Data for Capacity Evaluation of Deep Foundations". In: *From Research to Practice in Geotechnical Engineering*. Reston, VA: American Society of Civil Engineers, pp. 312–330. ISBN: 9780784409626. DOI: 10.1061/40962(325)8.

Rausche, Frank, Fred Moses, and George G Goble (1972). "Soil resistance predictions from pile dynamics". In: *Journal of the soil mechanics and foundations division* 98.9, pp. 917–937.

Rausche, Frank, M Nagy, and Garland Likins (2008). "Mastering the art of pile testing". In: *Proceedings of the Eighth International Conference on the Application of Stress Wave Theory to Piles*, pp. 19–32.

Remspecher, Fabian (2014). "Experimenteller Tragfähigkeitsnachweis von Pfahlgründungen für Offshore- Windenergieanlagen in Abhängigkeit vom Einbringverfahren". In: September. Berlin: 33 - Baugrundtagung - Spezialsitzung der jungen Geotechniker.

Rimoy, S., Matias Silva, Richard J. Jardine, Z. X. Yang, B. T. Zhu, and C. H.C. C. Tsuha (2015). "Field and model investigations into the influence of age on axial

capacity of displacement piles in silica sands". In: *Géotechnique* 65.7, pp. 576–589. ISSN: 17517656. DOI: 10.1680/geot.14.P.112.

Robertson, Peter Kay, Richard G Campanella, Donald Gillespie, and James Greig (1986). "Use of piezometer cone data". In: *Use of in situ tests in geotechnical engineering*. ASCE, pp. 1263–1280.

Rodger, A. A. and G. S. Little John (1980). "A Study of Vibratory Driving in Granular Soils". In: *Geotechnique* 30.3, pp. 269–293. ISSN: 17517656. DOI: 10.1680/geot.1980.30.3.269.

Rohrig, K, C Richts, S Bofinger, M Jansen, M Siefert, S Pfaffel, and M Durstewitz (2013). *Energiewirtschaftliche Bedeutung der Offshore-Windenergie*. Tech. rep. Fraunhofer-Institut für Energiewirtschaft und Energiesystemtechnik.

Salgado, Rodrigo (2008). *The engineering of foundations*. Vol. 888.

Schilder, Constanze, Harald Kohlhoff, Detlef Hofmann, Frank Basedau, Wolfgang R. Habel, Matthias Baeßler, Ernst Niederleithinger, Steven Georgi, and Markus Herten (2013). "Static and dynamic pile testing of reinforced concrete piles with structure integrated fibre optic strain sensors". In: ed. by Leszek R. Jaroszewicz, p. 879447. DOI: 10.1117/12.2026813.

Schneider, James A. (2007). "Analysis of piezocone data for displacement pile design". PhD thesis. The University of Western Australia School.

Schneider, James A., Xiangtao Xu, and Barry M. Lehane (2008). "Database Assessment of CPT-Based Design Methods for Axial Capacity of Driven Piles in Siliceous Sands". In: *Journal of Geotechnical and Geoenvironmental Engineering* 134.9, pp. 1227–1244. ISSN: 1090-0241. DOI: 10.1061/(asce)1090-0241(2008)134:9(1227).

Shek, L. M. P., L. M. Zhang, and H. W. Pang (2006). "Set-up effect in long piles in weathered soils". In: July, pp. 145–152.

Shioi, Y, O Yoshida, T Meta, and M Homma (1992). "Estimation of bearing capacity of steel pipe pile by static loading test and stress-wave theory (Trans-Tokyo Bay Highway)". In: *International conference on the application of stress-wave theory to piles*, pp. 325–330.

Sindowski, Karl-Heinz (1963). "Die drenthestadiale Altenwalder Stauchmoräne südlich Cuxhaven". In: *Zeitschrift der Deutschen Gesellschaft für Geowissenschaften*. Vol. 115. 1, pp. 158–162. DOI: 10.1127/zdgg/115/1965/158.

Skinner, A E (1969). "A note on the influence of interparticle friction on the shearing strength of a random assembly of spherical particles". In: *Geotechnique* 19.1, pp. 150–157.

Skov, Rikard and Hans Denver (1988). "Time-dependence of bearing capacity of piles". In: Ottawa: The 3rd International Conference on Apllication of Stress-wave Theory to Piles, pp. 25–27.

Smith, E A L (1960). "Pile-driving analysis by the wave equation". In: *Journal of the soil mechanics and foundations division* 86.4, pp. 35–61.

Soderberg, Lars O (1962). "Consolidation theory applied to foundation pile time effects". In: *Geotechnique* 12.3, pp. 217–225.

Subba Rao, K K S, M M Allam, and R G Robinson (1998). "INTERFACIAL FRICTION BETWEEN SANDS AND SOLID SURFACES." In: *Proceedings of the Institution of Civil Engineers - Geotechnical Engineering* 131.2, pp. 75–82. ISSN: 1353-2618. DOI: 10.1680/igeng.1998.30112.

Swart, R J, C Coppens, H Gordijn, M Piek, P Ruyssenaars, J J Schrander, P de Smet, M Hoogwijk, M Papalexandrou, E de Visser, and Others (2009). *Europe's onshore and offshore wind energy potential: An assessment of environmental and economic constraints*. Tech. rep. European Environment Agency. DOI: https://doi.org/10.2800/11373.

Tavenas, F. and R. Audy (1971). "Limitations of the Driving Formulas for Predicting the Bearing Capacities of Piles in Sand". In: *Canadian Geotechnical Journal*.

Terzaghi, Karl (1925). *Erdbaumechanik auf bodenphysikalischer Grundlage*. F. Deuticke.

Titi, Hani H. and G. Wije Wathugala (1999). "Numerical Procedure for Predicting Pile Capacity—Setup/Freeze". In: *Transportation Research Record: Journal of the Transportation Research Board* 1663.1, pp. 25–32. ISSN: 0361-1981. DOI: 10.3141/1663-04.

Tsuha, C.H.C., P.Y. Foray, Richard J. Jardine, Z. X. Yang, M Silva, and S. Rimoy (2012). "Behaviour of displacement piles in sand under cyclic axial loading". In: *Soils and Foundations* 52.3, pp. 393–410. ISSN: 00380806. DOI: 10.1016/j.sandf.2012.05.002.

Verfuss, Ursula K, Rachael R Sinclair, and Carol Sparling (2019). *A review of noise abatement systems for offshore wind farm construction noise, and the potential for their application in Scottish waters*. Scottish Natural Heritage.

Wackernagel, Hans (2003). *Multivariate geostatistics: an introduction with applications*. Springer Science & Business Media.

Wendel, E (1900). "On the test loading of piles and its application to foundation problems in Gothenburg". In: *Tekniska Samf Goteberg handl 7*, pp. 3–62.

White, D and Y. Zhao (2006). "A model-scale investigation into 'set-up' of displacement piles in sand". In: *Physical Modelling in Geotechnics*. 1998. Taylor & Francis. DOI: 10.1201/NOE0415415866.ch128.

White, D. J. and A. D. Deeks (2007). "Recent research into the behaviour of jacked foundation piles". In: *Advances in Deep Foundations*. Vol. 7096. January. Taylor & Francis, pp. 3–26. ISBN: 9780415436298. DOI: 10.1201/9780203938416.ch1.

White, D. J. and Barry M. Lehane (2004). "Friction fatigue on displacement piles in sand". In: *Geotechnique* 54.10, pp. 645–658. ISSN: 00168505. DOI: 10.1680/geot.2004.54.10.645.

Yang, Z. X., Richard J. Jardine, B. T. Zhu, and S. Rimoy (2014). "Stresses Developed around Displacement Piles Penetration in Sand". In: *Journal of Geotechnical and Geoenvironmental Engineering* 140.3, pp. 1–13. ISSN: 1090-0241. DOI: 10.1061/(ASCE)GT.1943-5606.0001022.

York, Donald L., Walter G Brusey, Frank M. Clémente, and Stephen K Law (1994). "Setup and Relaxation in Glacial Sand". In: *Journal of Geotechnical Engineering* 120.9, pp. 1498–1513. ISSN: 0733-9410. DOI: 10.1061/(ASCE)0733-9410(1994)120:9(1498).

Zhang, Z. and Y. H. Wang (2015). "Examining Setup Mechanisms of Driven Piles in Sand Using Laboratory Model Pile Tests". In: *Journal of Geotechnical and Geoenvironmental Engineering* 141.3, p. 04014114. ISSN: 1090-0241. DOI: 10.1061/(ASCE)GT.1943-5606.0001252.

Zhang, Zitao and Yu-Hsing Wang (2016). "DEM modeling of aging or creep in sand based on the effects of microfracturing of asperities and evolution of microstructural anisotropy during triaxial creep". In: *Acta Geotechnica* 11.6, pp. 1303–1320. ISSN: 1861-1125. DOI: 10.1007/s11440-016-0483-3.